Velocity-based Cardiac Segmentation and Motion-Tracking

A Thesis
Presented to
The Academic Faculty

By

Jinsoo Cho

In Partial Fulfillment
Of the Requirements for the Degree
Doctor of Philosophy in the
School of Electrical and Computer Engineering

Georgia Institute of Technology
October 2003

Velocity-based Cardiac Segmentation and Motion-Tracking

Approved by:

Dr. Paul J. Benkeser, Advisor

Dr. Marijn E. Brummer

Dr. May D. Wang

Date Approved 11/17/2003

Acknowledgement

I would greatly like to thank my advisor, Paul Benkeser, for his invaluable guidance and encouragement. Without his patient help, all these would impossible. I am especially grateful to Marijn Brummer for his numerous help and serving on my committee. I am also thankful to May Wang, Arthur Koblasz, and John Oshinski for serving on my committee.

I must thank David Fann for his kind help and friendship through the five years. I am also grateful to Joel Jackson, Mark Smith, and Nikil Jayant for their valuable comments. Thanks to Derek Fyfe for the echocardiography data set and to Veer Mahajan for the phase contrast MRI data set. Special thanks to Jae-Beom Lee for his moral support.

I would very like to thank my parents for their support, encouragement, and great love throughout my life. I'm also very thankful to my parents-in-law for their support. I'll always be indebted to my wife, June. I dedicate this thesis to June and my daughter, Annie.

Table of Contents

List of Tables

List of Figures

Abbreviations

BMD – Boundary Matching Descriptor

C – Curcumferential

CT – Computerized Tomography

ED – End Diastole

EDE – Elastic Deformation Estimation

EF – Ejection Fraction

EPI – Echo Planar Imaging

ES – End Systole

GVF – Gradient Vector Flow

L – Longitudinal

LLC – Linear Correlation Coefficient

LV – Left Ventricle

MRI – Magnetic Resonance Imaging

OGF – Orientation Gradient Force

R — Radial

RV — Right Ventricle

SCT — Seed Contour Tracking

SNR — Signal to Noise Ratio

SPAMM— Spatial Modulation of Magnetization

TE — Delay Time

TR — Repetition Time

Summary

Heart disease is one of the more life-threatening diseases. Its accurate diagnosis and appropriate treatment are central to the survival of patients. Because the accuracy of cardiac functional parameters that have been widely used in diagnosis of heart disease depends heavily on cardiac image segmentation and motion-tracking techniques, it is essential that those techniques be accurate and reliable.

A velocity-aided cardiac segmentation method based a modified active contour model, the orientation gradient force (OGF), and phase contrast magnetic resonance imaging (MRI) has been developed to improve the accuracy of segmentation of the myocardial boundaries, especially the endocardial boundary. Furthermore, the initial seed contour tracking (SCT) algorithm was also developed to improve the accuracy of automatic sequential frame segmentation. The performance of the proposed method was assessed by experimentations on a phase contrast MRI data set of a normal human volunteer. Experimental results of individual frame segmentation showed modest improvements in the accuracy and reproducibility of the endocardial boundary

segmentation. Experimental results of the sequential frame segmentation showed that the propagation of errors caused by improper positioning of initial seed contours was significantly reduced by the use of the SCT.

A cardiac motion tracking method based on elastic deformation estimation (EDE) of a deformable model and phase contrast MRI has been also developed to track the three-dimensional motion of the myocardium addressing the problem of relatively low out-of-plane resolution of MRI. The advantage of this method is that it can provide a physically plausible yet computationally efficient and shape-independent framework for cardiac motion tracking. To assess the proposed method, the motion of a normal human left ventricle (LV) was tracked throughout the entire cardiac cycle. Then, the tracking results were compared with a color-coded tissue Doppler echocardiography data set. A strain analysis was also carried out. The results showed that the out-of-plane velocity measurements from the LV model were correlated with those of the echocardiography data set at the selected regions in the septum and the strain measurements were generally found to be consistent with previously published values.

CHAPTER 1

Introduction

1.1 Motivation

Heart disease is one of the more life-threatening diseases. Its accurate diagnosis and appropriate treatment are central to the survival of patients. Numerous diagnostic methods that can assess abnormalities of the heart have been developed. Among these methods, cardiac functional analysis has been widely used to derive global and regional parameters that describe the functionality of the heart. Because the accuracy of these parameters depends heavily on cardiac segmentation and motion-tracking techniques, it is essential that those techniques be accurate and reliable. However, since a heart has such a complex shape and motion pattern, the development of an accurate cardiac segmentation and motion-tracking technique still remains a challenging problem.

Accurate segmentation of the myocardial boundaries is essential for deriving cardiac global functional parameters such as ventricular volume/mass, ejection fraction, and cardiac output. It is also an important step for accurate motion and deformation analysis of the myocardium and has been done by automatic or semiautomatic techniques. However, current segmentation techniques have difficulty both extracting accurate myocardial boundaries and performing a fully automatic process because of low image quality, a complex shape and motion pattern of the heart, and lack of clear delineation between the myocardium and adjacent anatomic structures [1].

Many studies have also been carried out to correlate the dynamic characteristics of the heart with a priori knowledge of various cardiac pathologies using various kinds of imaging modalities. However, difficulty assessing motion of the myocardium still comes not only from the difficulty in correlating the positions of points within the myocardium between images taken at subsequent time frames but also from relatively low out-of-plane resolution of imaging modalities such as magnetic resonance imaging (MRI). Although N.B. Ingels *et al.* [2] and GD. Meier *et al.* [3] used implanted markers to obtain correlation of the position, these techniques are unacceptable in clinical situations because of their invasiveness. Recently, a number of MR imaging modalities that use

presaturated tagging patterns [4, 5, 6, 7] and velocity-encoded phase images [8] have been developed to obtain correlation of the position noninvasively. Although these methods make it possible to quantify the severity and extent of regional myocardial motion abnormalities noninvasively, an appropriate heart model is still needed to track the positions of tissue points in the myocardium and interpolate sparse displacements due to relatively low out-of-plane imaging resolution and sparse markers, respectively.

The first goal of this thesis is to develop an accurate and reliable semiautomatic cardiac segmentation method that can be used not only to obtain more accurate global functional parameters but also to construct an accurate shape description of the heart. The second goal is to develop a cardiac motion-tracking method for extraction of motion and deformation parameters that can give accurate descriptions of regional functions of the heart.

1.2 Problem Statement

Although current cardiac segmentation and motion-tracking techniques are quite successful, they still have the following major problems and limitations:

1. Segmentation of the endocardial boundary suffers from problems such as flow-related signal loss, the presence of papillary muscles, and poor visualization of the endocardium.
2. Large changes in positions and shapes of the myocardial boundaries through subsequent frames make it difficult to follow the boundaries and cause the propagation of errors in sequential frame segmentation.
3. Given that the MR imaging plane is spatially fixed and has relatively low out-of-plane resolution, motion-tracking of the myocardium in three-dimensional space introduces errors not only in the out-of-plane direction but also in the in-plane directions.
4. Most of model-based motion-tracking techniques are confined to a specific ventricle of the heart to reconstruct the three-dimensional motion of the myocardium.

A commonly used cardiac segmentation technique in routine clinical practice is semiautomatic segmentation, which requires a human operator's intervention. For semiautomatic segmentation, the active contour model, which was first proposed by Kass *et al.* [9], has been a popular choice as an underlying automation technique. However,

semiautomatic segmentation based on the active contour models still have difficulty extracting accurate myocardial boundaries, especially the endocardial boundary. This thesis describes the development of a cardiac segmentation method that is based on the generalized active contour model, the tensor-based orientation gradient force, the initial seed contour tracking algorithm, and phase contrast MRI to improve the accuracy of the endocardial boundary segmentation and sequential frame segmentation.

One of the primary approaches to estimate the motion and deformation of the myocardium using various MR imaging modalities is to use a three-dimensional model of the heart. In such model-based approaches, geometric models or finite element models have been used to reconstruct the three-dimensional displacement fields of the myocardium. However, geometric model-based approaches require separate models for each ventricle of the heart, and finite element model-based approaches that can reflect the physical properties of the myocardium are computationally expensive. In this thesis, a cardiac motion-tracking method based on an elastically deformable model and phase contrast MRI has also been developed to reflect the elastic property of the myocardium with reduced computational expenses and to make a cardiac motion-tracking method less dependent on the shape of a specific ventricle.

1.3 Contributions of this Work

The major contributions of this work are summarized as follows:

- The development of an active contour model with a new image force derived from the velocity images of phase contrast MRI to improve the accuracy of segmentation of the myocardial, especially endocardial, boundaries.
- The development of a sequential frame segmentation algorithm for the velocity-aided active contour model to reduce the propagation of errors in the automatic sequential frame segmentation.
- The development of a three-dimensional cardiac motion tracking method based on an elastically deformable model and phase contrast MRI. It uses a physical property of the myocardium to reconstruct the three-dimensional displacement fields of the myocardium.

Unlike other MRI cardiac segmentation methods based on active contour models, the velocity images from phase contrast MRI, together with the magnitude images, are used to derive a new external force from the orientation gradient. Although the one-dimensional velocity images have been used in vessel segmentation [24], it is the first attempt to use the three-dimensional velocity images in cardiac segmentation. With the

additional information from the velocity images, a new seed contour tracking (SCT) algorithm for a modified active contour model provides a prediction scheme of positions of initial seed contours through a sequence of cardiac MR images. It contributes to reduce the propagation of errors in the automatic sequential frame segmentation. Finally, a new cardiac motion-tracking method based on an elastically deformable model provides a tool for compensating the relatively low out-of-plane resolution of phase contrast MRI to track the three-dimensional motion of the myocardium.

1.4 Structure of the Thesis

This thesis consists of two main parts. The first part presents a cardiac segmentation method in two chapters: chapter 2 describes the research background of cardiac segmentation, and chapter 3 develops a velocity-aided cardiac segmentation method and presents experimental results. The second part is similarly organized: chapter 4 describes the research background of cardiac motion-tracking, and chapter 5 develops an elastically deformable model-based cardiac motion-tracking method and presents experimental results.

Part I

Cardiac Segmentation

CHAPTER 2

Background

In this chapter, cardiac functional parameters and segmentation methods that have been used previously to identify the myocardial boundaries are described. Cardiac segmentation methods using deformable model-based approaches are of primary interest.

2.1 Cardiac Functional Parameters

Cardiac functional parameters describe the functionality of the heart and are frequently used in diagnosis of various heart diseases. These parameters can be divided into two main areas, global parameters and regional parameters. Global parameters include general volumetric measures such as ventricular volume, ventricular mass, ejection fraction, stroke volume, and cardiac output. Regional parameters include motion

and deformation parameters that are related to the motion of the heart during the cardiac cycle, such as wall thickening, strain, and strain rate.

Ventricular volume is typically measured from images obtained from either angiocardiography, echocardiography, or MRI. Volume measurement techniques are typically based on a geometric model, such as Simpson's rule. Simpson's Rule is a fundamental mathematical principle. It is based on the idea that the volume of an object can be determined by cutting the object into thin slices measuring the volume of each slice and summing the volumes of all slices. With a boundary segmentation method, Simpson's Rule is applied to the left ventricle (LV) by slicing the LV into disks along the long axis, as shown in Figure 1. The area of each disk is calculated and multiplied by the disk's thickness to determine its volume. As described, techniques for volume measurement first estimate the myocardial boundaries to approximate the ventricular shape and then calculate the volume of those shapes. Echocardiography may easily underestimate the ventricular volume, and angiocardiography may overestimate the ventricular volume when the volume of the papillary muscles or trabeculations is not taken into account. Some studies [10, 11] have shown that MRI provides better estimation of the ventricular volume than other imaging modalities.

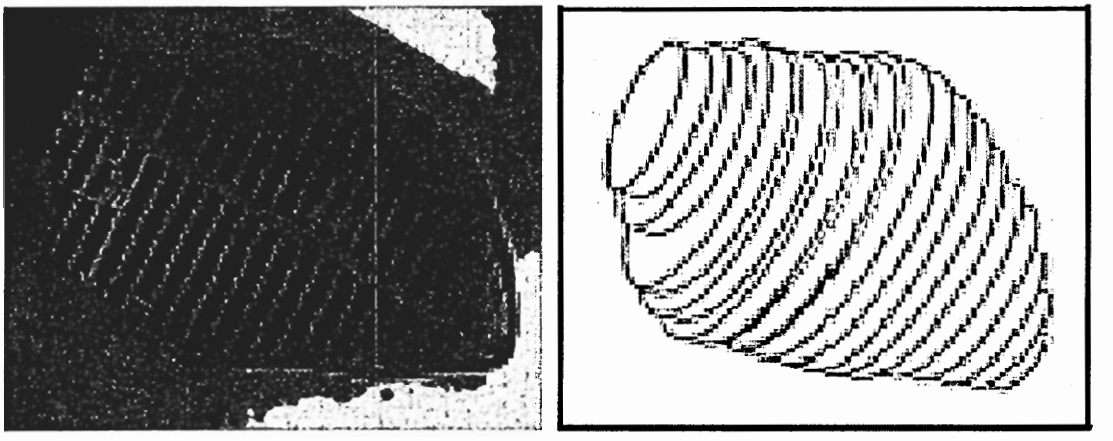

Figure 1. Simpson's rule for LV volume measurement. Ventricular volume $V = \frac{\pi}{4}\sum_{i=1}^{n} D_i^2 \Delta L$

Ventricular mass is another useful measure of the global functionality of the heart because ventricular hypertrophy is characterized by an increase in muscle mass. This parameter is determined by calculating the total ventricular volume within the epicardial borders, subtracting the ventricular volume, and multiplying the result by the density of the muscle tissue. Ejection fraction (EF) is a frequently used global parameter that measures the pumping function of the ventricle. It is derived from the end-systolic and end-diastolic ventricular volumes. Stroke volume is calculated as the difference between the end-diastolic and end-systolic volume, and cardiac output is derived from the product

of the stroke volume and the heart rate.

Wall thickening is an indicator of dysfunctional contraction and closely associated with myocardial viability. Three-dimensional myocardial wall motion and thickening were used as methods for distinguishing ischemic from non-ischemic myocardium [12]. Strain is the change in length of the myocardium relative to its original length and has been used to describe myocardial deformation. There have been numerous efforts to estimate strain values of the myocardium. One of the more widely used approaches is the model-driven approach [13]. In this approach, a shape model of the heart is used to calculate and visualize the three-dimensional regional strain data throughout the cardiac cycle. Derived strain data are then used to find the abnormalities of the motion of the myocardium and to describe the contractility of the myocardium. Strain calculations have been mostly conducted for the analysis of LV deformation [14, 15] because of its relative geometric simplicity. Strain rate is the temporal derivative of strain and is also an indicator of deformation of the myocardium, as shown in Figure 2. It is a load-independent index that is, unlike strain, only slightly affected by rigid-motion, such as translation and rotation. Studies [16, 17, 18] have suggested that regional myocardial strain rate estimation can be performed in a clinical setting and may prove to

be a robust and sensitive tool to define alterations in either contractile function or passive elastic deformation within a myocardial segment. The strain-stress relationship has also been used to describe regional deformation characteristics [19].

As described previously, estimation of the myocardial boundaries is an essential step for deriving various cardiac functional parameters, and the accuracy of these parameters depends on the correctness of the estimated boundaries. Therefore, it is essential that cardiac segmentation be accurate and reliable. Numerous cardiac segmentation methods have been developed and used to estimate the myocardial boundaries more accurately and efficiently. These methods can be divided into three broad classes, such as manual segmentation, semiautomatic segmentation, and automatic segmentation, according to the level of human operator's intervention. Because manual and semiautomatic cardiac segmentation methods are widely used in routine clinical practice, these are described in the next two sections.

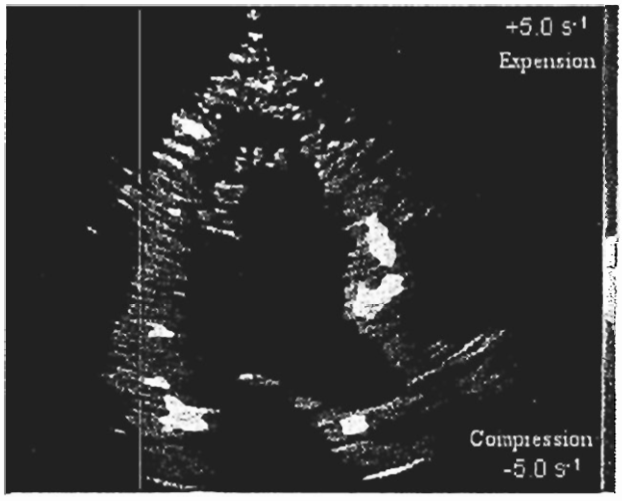

Figure 2. An example of strain rate image of LV from color-coded tissue Doppler echocardiography.

2.2 Manual Segmentation

Manual segmentation is performed by human operators with a computer, an input device (usually a mouse), and a display device to trace the endocardial and epicardial boundaries in cardiac images. Because human operators can use their a priori knowledge of the anatomical structure of the heart, the results of manual segmentation are usually more reliable than those of automatic and semiautomatic segmentation. Therefore, it is often considered the "*gold standard*" and is widely used in routine clinical practice. However, manual segmentation is time consuming and subject to operator-dependent variability.

2.3 Semiautomatic Segmentation

A full automation of cardiac segmentation is a quite difficult task because of the complex shape of the heart and noisy imaging modalities. Instead, semiautomatic segmentation approaches that include expert interactive guidance are preferably used in routine clinical practice. The active contour model based on a deformable contour model is one of these semiautomatic segmentation approaches. It overcomes many of the limitations of traditional image processing techniques, such as region growing, edge detection, and mathematical morphology operations. This connected and continuous geometric model uses a priori knowledge of object shape to constrain the segmentation problem, and its inherent continuity and smoothness can compensate for noise, gaps, and other irregularities in object boundaries, such as the myocardial boundaries. These properties can make it possible to link sparse or noisy image features into a coherent and consistent model of the myocardial boundaries. In this semiautomatic segmentation approach, the operator usually initiates the segmentation process either by specifying an initial region of interest or by drawing an initial shape of the object to be segmented. Then, the operator visually checks the accuracy of the points that have been automatically generated. The points that have been improperly positioned after automatic segmentation

can be modified manually through an interactive correction routine. The original active contour model and its several variations are briefly described in this section.

As described previously, the active contour models are deformable contour models that are often used to approximate the locations and shapes of object boundaries in images based on the assumption that boundaries are piecewise continuous or smooth. These models are also known as "snakes" and are examples of more general techniques of matching a deformable model to an image by energy minimization. Unlike the other segmentation methods, these models are active: a contour model minimizes its energy functional and exhibits dynamic behavior. Snakes usually do not try to find the entire salient contours in images, but they find a desired contour using an initial seed contour. The original snake [9] is a controlled continuity spline under the influence of image forces and external constraint forces. Its mathematical formulation draws from the theory of optimal approximation involving functionals. Geometrically, a snake is a parametric contour in the image plane $(x, y) \in \Re^2$. Representing the position of a snake parametrically by $\mathbf{v}(p) = (x(p), y(p))$, the energy of a snake is defined as:

$$E_{snake} = \int_0^1 \{ E_{int}(\mathbf{v}(p)) + E_{img}(\mathbf{v}(p)) + E_{ext}(\mathbf{v}(p)) \} dp \qquad (1)$$

where E_{int} represents the internal energy of the spline, E_{img} represents the image force, and

E_{ext} represents the external constraint force. The functional represents the energy of the contour, and the final shape of the contour corresponds to the minimum of this energy. The internal spline energy is defined as:

$$E_{int}(\mathbf{v}(p)) = \sigma(p)\left|\frac{\partial \mathbf{v}(p)}{\partial p}\right|^2 + \varsigma(p)\left|\frac{\partial^2 \mathbf{v}(p)}{\partial p^2}\right|^2 \quad (2)$$

The internal energy consists of a first-order elasticity term and a second-order rigidity term. $\sigma(p)$ controls the tension (stretching) of the contour and $\varsigma(p)$ controls the flexibility (bending) of the contour. The image force consists of three different energy components that attract a snake to lines, edges, and terminations. Edge force, one of image force components, is defined as:

$$E_{img,edge} = -\left|Grad(x,y)\right|^2 \quad (3)$$

where $Grad(x,y)$ represents the image gradients. A snake is attracted to contours with large image gradients. The external constraint force (E_{ext}) is defined as the spring force to provide the interactivity in energy minimization process. By the calculus of variations, $\mathbf{v}(p)$ that minimizes the energy E_{snake} must satisfy the Euler-Lagrange equation. This vector-valued partial differential equation is discretized by finite differences, and the solution $\mathbf{v}(p)$ is calculated by an implicit Euler time-integration method. Although this

original active contour model has a shrinkage problem around strong edge points, it provides a simple framework to combine high-level global constraints with low-level local constraints so that it can effectively segment the object of interest. Cohen [20] modified the image force of the original active contour model by normalizing it to obtain more stable results and also added an inflation force in the direction of the outward normal of the contour to eliminate the shrinkage problem around strong edge points. His model is effective for segmentation of the myocardial boundaries in noisy images such as ultrasound and MR images of the heart because it avoids the contour's being trapped by spurious isolated edge points and makes the result more insensitive to the initial contours. Later, he extended his model into three-dimensions [21].

Most cardiac segmentation methods based on the active contour models rely on using only the image gray scale or gradient information to identify the myocardial boundaries. However, using the image gray scale or gradient information alone may not be sufficient to identify the accurate myocardial boundaries due to low signal-to-noise ratio (SNR) of images or complex shape characteristics of the boundaries. To address these problems, different kinds of image forces have been proposed for the external energy of the active contour model. Xu *et al.* [22] used the curvature information to

derive an external image force. They also proposed gradient vector flow (GVF) computed as a diffusion of the gradient vectors of a gray-level edge map [23]. These image forces reduced the problems associated with poor convergence to concave boundaries, such as the endocardial boundary with papillary muscles. Recently, Kozerke *et al.* [24] proposed an automatic vessel segmentation algorithm that used the active contour model with the velocity-based external force. In their approach, the velocity images from phase contrast MRI in addition to the magnitude (intensity) image are used to address the degradation problem of magnitude image around the vessel wall boundary that is similar to those associated with defining the myocardium boundaries. The original controlled continuity spline by Kass *et al.* [9] is used for the internal energy, and the conventional image force from the edge map of magnitude image is used for the external energy. However, in the case of severe signal distortions near the vessel wall boundaries resulting from disturbed flow conditions and partial volume effects, velocity images from phase contrast MRI are used to derive new image force to replace the image force based on the edge map. By simulation, they showed that the boundary representations from velocity images were often better than those from magnitude images. The sequential frame segmentation in their active contour model also benefits from this image force because the initial seed

contour for the current frame is the contour from the previously segmented frame. Although the application of this technique was the vessel segmentation, the result suggested the possibility of using velocity profiles as a new image force in segmentation of the myocardial boundaries.

The active contour models have been very effective for segmenting and tracking of moving objects in image sequences, such as cardiac image sequences. Several variations of the original active contour model have been also proposed to improve sequential segmentation of the myocardial boundaries throughout the cardiac cycle. Leymarie *et al.* [25] used the previously segmented contour as an initial seed contour for the current frame to track the contour through a sequence of images. Inspired by this idea, Gupta *et al.* [26] used the active contour model in four-dimensional cardiac analysis study. In their approach, the contour is automatically propagated throughout the entire slices and time frames using the previously segmented contour as an initial seed contour as in Leymarie's approach. However, two different energy minimization techniques are used for the automatic propagation of the contour, because contour deviation between two consecutive slices is usually greater than that between two consecutive time frames. The steepest descent method that attempts only local optimization of the contour energy is

used for temporal propagation of the contour. Dynamic programming, with larger search region and thus less susceptible to local minima, is used for spatial propagation of the contour. The inflation and deflation forces are also used to effectively follow the contracting boundaries of the myocardium. Chalana *et al.* [27] proposed a multiple active contour model to reduce the propagation of errors in sequential frame segmentation of the myocardial boundaries on echocardiographic sequences. They added the temporal smoothness and the monotonic motion constraints into the internal and the external energy formulation, respectively. Li *et al.* [28] also proposed a similar approach to take into account a temporal smoothness of the contour. In the presence of large changes in positions and shapes of the myocardial boundaries through the subsequent frames, simply using the previously segmented contour as an initial seed contour may cause severe propagation of errors in sequential segmentation of the myocardial boundaries. Therefore, boundary position prediction methods in addition to the active contour models have been proposed to cope with these errors. Akgul *et al.* [29, 30, 31] proposed a post-processing technique to improve sequential frame segmentation of the tongue surface in ultrasound image sequences. They tracked the previously segmented contour using the optical flow technique to obtain a closer initial seed contour to the desired boundary. As a result, it

reduced the propagation of errors in sequential frame segmentation. Peterfreund [32] also applied the optical flow technique in his velocity-controlled active contour model to estimate a better seed contour. Although the applications of Akgul's and Peterfreund's approaches were not cardiac segmentation, they suggested that using motion information of the myocardium would improve the accuracy of sequential frame segmentation of the myocardial boundaries.

CHAPTER 3

Velocity-aided Cardiac Segmentation

3.1 Introduction

As described previously, manual segmentation of the myocardial boundaries is considered the "*gold standard*." However, it is time consuming and subject to operator-dependent variability. Therefore, semiautomatic segmentation methods such as the active contour models are preferred in routine clinical practice. Although active contour models have been quite successful in segmentation of the myocardium boundaries, most of them still suffer from problems such as flow-related signal loss, the presence of papillary muscles, heterogeneity of the myocardium signal, poor visualization of the endocardium on the most apical slices, and lack of clear delineation between the myocardium and adjacent anatomic structures. In addition, large changes in positions and shapes of the myocardial boundaries through the subsequent time frames may cause the propagation of

errors in sequential frame segmentation, even if the segmentation algorithm within an individual frame is highly reliable. In this chapter, a new cardiac segmentation method that is based on phase contrast MRI, the generalized active contour model, the tensor-based orientation gradient force, and the sequential frame segmentation algorithm is proposed to cope with some of these problems.

3.2 Phase Contrast MRI

3.2.1 Terminology

Cine MRI with short repetition time (TR) is useful for imaging dynamic processes. This imaging technique uses a gating strategy that acquires data at a constant rate and retrospectively sorts and interpolates the data into the desired number of frames per cycle [33]. Phase contrast MRI refers to a family of MR imaging methods that exploit the fact that spins that move through magnetic field gradients obtain a different phase than static spins, enabling the production of images with controlled sensitivity to flow. The combination of these two tools produces a technique that can depict motion and flow throughout the cardiac cycle. This is called *cine-phase contrast MRI* or simply *phase*

contrast MRI.

Phase contrast MRI has been used for several quantitative motion applications, including measurement of flow of blood, cerebrospinal fluid, motion of the brain, skeletal muscle, and angiography. It is also well suited for measurement of cardiac tissue velocities because of their speed, flexible velocity sensitivity, and inherent quantitative foundation. In this thesis, phase contrast MRI is used for segmentation of the myocardial boundaries, because it is capable of measuring velocities of both the myocardium and blood.

3.2.2 Physical Principle

Each raw data set of MRI produces images that portray the transverse magnetization in each voxel. This transverse magnetization is a vector quantity having both magnitude and phase. Typically, in MRI only the magnitude of the magnetization contributes to the image intensity. However, the phase can contain useful information about motion: i.e., spins that move through magnetic field gradients obtain a different phase than static spins, enabling the production of images with controlled sensitivity to motion.

Motion in the presence of a magnetic field gradient produces a change in phase proportional to velocity v [8]:

$$\phi = v\,(\kappa M_1) \tag{4}$$

$$M_1 = \int_0^{TE} W(t)t \cdot dt \tag{5}$$

where, ϕ is phase, κ is the gyromagnetic ratio, and M_1 is the first moment of the gradient waveform $W(t)$ evaluated at echo delay time (TE). In a manner completely analogous to spatial phase encoding for image generation, the read-out gradient waveform encodes motion in the direction of this gradient into the phase of the signal, and demonstrates the effect of flow and myocardial motion in spin-echo data.

If two complete data sets are acquired with gradient waveforms that have a different first moment in one direction, the difference in phase in each pixel (by simple subtraction between two phase images) will be

$$\Delta\phi = v\,(\kappa \Delta M_1)\,. \tag{6}$$

Static structures will exhibit no phase change. By acquiring two measurements with different gradient first moments (by altering the gradient waveform shape), the method can be sensitive to phase shift due to motion yet be insensitive to other phase effects (e.g., the field gradient inhomogeneity). A critical parameter of phase contrast images is the

strength of the flow (motion) encoding controlled by ΔM_1 (strong encoding means strong gradient waveform). An intuitive alternative is the encoding velocity, v_{enc}, that produces a phase shift ($\Delta\phi$) of π radians or 180°:

$$v_{enc} = \pi \; / \; (\kappa \, \Delta M_1) \tag{7}$$

This parameter is useful because it also represents the largest speed that can be measured unambiguously. Because the velocity over v_{enc} means the phase shift over 180°, this causes the phase wrap-around problem (velocity aliasing). Therefore, v_{enc} has to be larger than the maximum velocity that can be measured in the moving structure. The v_{enc} value is controlled by adjusting the strength of the flow encoding ΔM_1. The measured phase shift is converted to velocity by:

$$v = \left(\frac{v_{enc}}{\pi} \right) \cdot \Delta\phi \tag{8}$$

With the above phase encoding methods and parameters, three directional-dependent velocity images can be produced, one for each Cartesian direction (x, y, z), as shown in Figure 3. One magnitude image can be also obtained by conventional frequency and phase encoding along with the velocity images. Therefore, four acquisitions are required to produce a set of three-dimensional velocity images.

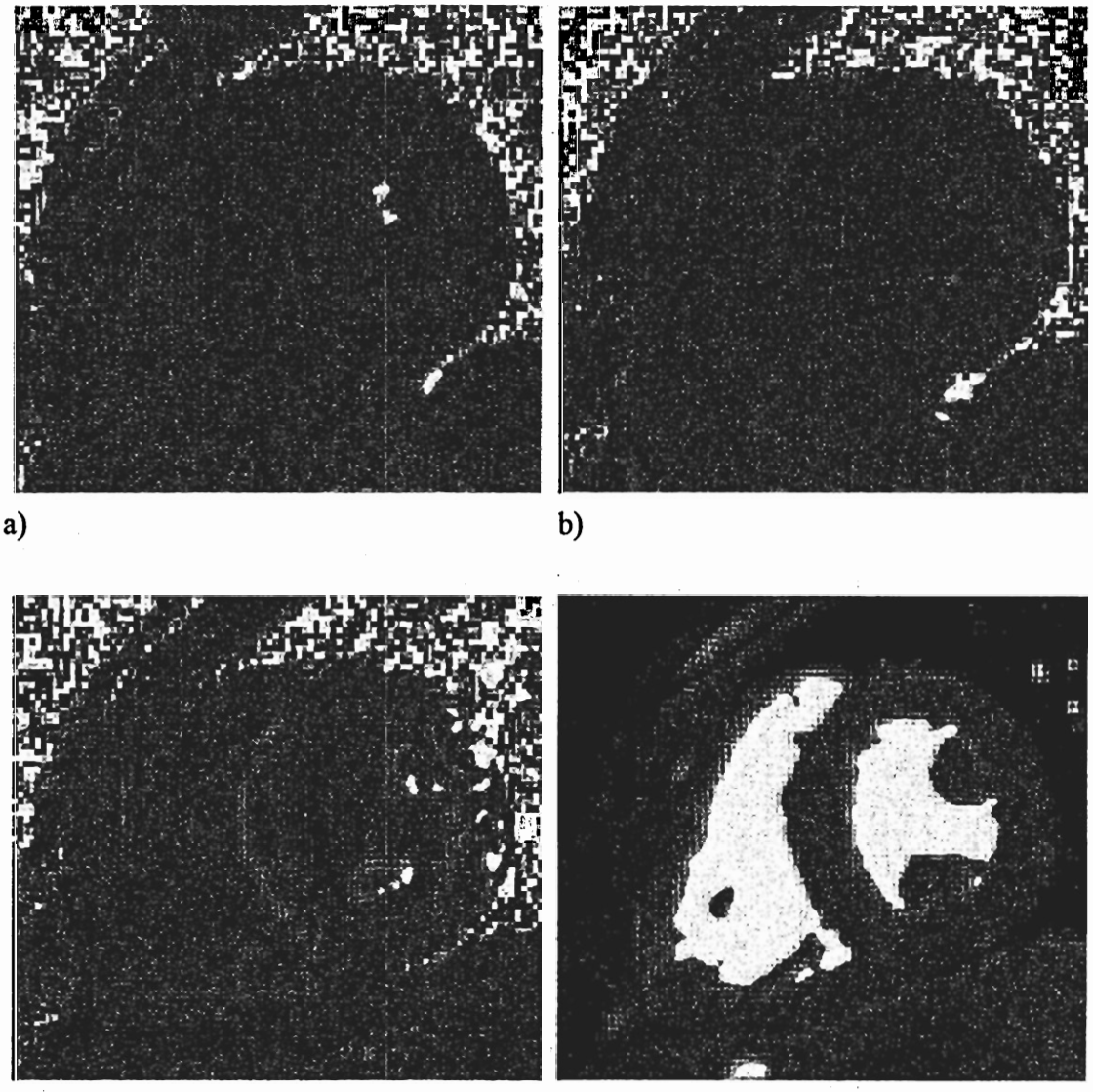

Figure 3. Typical velocity images around end systole. a) horizontal directional (v_x) velocity image b) vertical directional (v_y) velocity image c) out-of-plane directional (v_z) velocity image, and d) magnitude image.

3.3 Generalized Active Contour Model

The generalized active contour model [34], which is a variation of the original active contour model, turns a boundary extraction problem into an energy minimization problem and is designed to eliminate the shrinkage problem around strong edge points. It is also invariant to scale change and rotation. In this thesis, this model will be used and modified to incorporate a new external force that is based on the orientation gradient of velocity vector fields.

The generalized active contour model balances two different potential energies, which are internal deformation potential energy (E_{int}) and external potential energy (E_{ext}). E_{int} imposes continuity and smoothness constraints, and E_{ext} attracts the snake to salient image features. By combining these two energy terms, the total potential energy for the boundary extraction problem is defined as:

$$E_{total} = \int_0^1 E_{int}(\mathbf{v}(p)) + E_{ext}(\mathbf{v}(p))dp \tag{9}$$

where $\mathbf{v}(p) = (x(p), y(p))$ is a parametric representation of the position of a contour, x and y are the coordinate functions in the image plane $(x, y) \in \Re^2$, and $p \in [0, 1]$ is the parametric domain. This potential energy represents the energy of a contour, and the final shape of the contour corresponds to the minimum of this energy. In practice, this

continuous form of the energy formulation can be replaced by the discrete form of the energy formulation. If the ordered set of points are defined as $V = [\mathbf{v}_1, \mathbf{v}_2, \ldots, \mathbf{v}_n]$, where $\mathbf{v}_i = (x_i, y_i)$ for $i = 1, 2, \ldots, n$, then, the solution set of points with the minimum energy of E_{total} can be expressed by:

$$V^* = \arg\min\left\{\sum_{i=1}^{n} \eta_i E_{int}(\mathbf{v}_i) + (1-\eta_i) E_{ext}(\mathbf{v}_i)\right\} \tag{10}$$

where $\eta_i \in [0, 1]$ is the regularization parameter at each contour point. Large η_i's generate strong model-driven solutions reflected largely by continuity and smoothness constraints of the contour, and small η_i's generate strong image feature-driven solutions. The local mini-max criterion is used to automatically select the regularization parameters that produce the optimal tradeoff at every contour location in a local sense. The energy formulation for the local optimum is

$$E(V, \Gamma) = \sum_{i=1}^{n} \left[\eta_i E_{int}(\mathbf{v}_i) + (1-\eta_i) E_{ext}(\mathbf{v}_i)\right] \tag{11}$$

where $\Gamma = \{\eta_1, \eta_2, \ldots, \eta_n\}$ are the unknown local regularization parameters. Seeking a local mini-max solution set V^* that minimizes the maximum of $E(V, \Gamma)$ over every η_i yields the local mini-max criterion:

$$E(V^*, \Gamma^*) = \min_{V} \sum_{i=1}^{n} \max(E_{int}(\mathbf{v}_i), E_{ext}(\mathbf{v}_i)) \tag{12}$$

where V^* and Γ^* are the solutions. This criterion completely bypasses the explicit selection of the parameters Γ^* and can be incorporated into the discrete energy minimization process.

In the original active contour model [9], the internal energy E_{int} was defined as the first and second derivatives of the contour, controlling the tension and rigidity respectively. On the discrete grid, the original formulation of E_{int}, Equation (2), can be approximated by the finite difference method:

$$E_{int}(\mathbf{v}_i) = \|\mathbf{v}_i - \mathbf{v}_{i-1}\|^2 + \|\mathbf{v}_{i-1} - 2\mathbf{v}_i + \mathbf{v}_{i+1}\|^2 \tag{13}$$

This approximation has several problems in practical situations. E_{int} vanishes when $\mathbf{v}_i = \mathbf{v}$ for all i causing the contour to shrink around strong edge points. E_{int} is also not invariant to scale change and rotation causing error in constraining smoothness on the contour. In order to impose smoothness constraint without the shrinkage problem, E_{int} is defined to force the contour to take the form of a line for an opened contour or a circle for a closed contour:

$$E_{int}(\mathbf{v}_i) = \frac{1}{l(V)}\|\mathbf{v}_i - \upsilon(\mathbf{v}_{i-1} + \mathbf{v}_{i+1})\|^2 \tag{14}$$

where $\upsilon = 0.5$ or $\upsilon = 0.5\cos^{-1}(2\pi/n)$ for opened and closed contours respectively. In order to make E_{int} invariant to scale change and rotation, the normalizing function $l(V)$ is

defined as the average distance between each of two neighboring points:

$$l(V) = \frac{1}{n}\sum_{i=1}^{n}\left\|\mathbf{v}_i - \mathbf{v}_{i-1}\right\|^2 \tag{15}$$

The external energy E_{ext} is generalized to include intensity gradient direction if necessary. Define image b as the function b: $I \rightarrow \Lambda$. Depending on the data type of either $\Lambda = D$ (intensity image or edge magnitude) or $\Lambda = D^2$ (2×1 intensity gradient vector), the external energy is formulated as follows:

$$E_{ext}(\mathbf{v}_i) = 1 - \mathbf{h}_i^T b(\mathbf{v}_i) \tag{16}$$

where $\mathbf{h}_i$ is the unit normal vector at $\mathbf{v}_i$, $\|\mathbf{h}_i\| = 1$. For $\Lambda = D^2$, $\mathbf{h}_i$ is normal to the tangent vector $\mathbf{t}_i$ of the contour:

$$\mathbf{t}_i = \frac{\mathbf{v}_i - \mathbf{v}_{i-1}}{\left\|\mathbf{v}_i - \mathbf{v}_{i-1}\right\|} + \frac{\mathbf{v}_{i+1} - \mathbf{v}_i}{\left\|\mathbf{v}_{i+1} - \mathbf{v}_i\right\|} \tag{17}$$

E_{ext} continuously weighs the gradient magnitude against any orientation in consistency. An edge point whose orientation disagrees with that of neighboring points may yield large external energy and is consequently considered the noise.

3.4 Tensor-based Orientation Gradient Force

Cardiac segmentation based on active contour models and MRI has used only MR magnitude (intensity) images to derive image forces. However, it is still a difficult task to find accurate myocardial boundaries, especially the endocardial boundary, because of problems such as flow-related signal loss, the presence of papillary muscles, and poor visualization of the endocardium in MR magnitude images as described previously. Kozerke *et al.* [24] addressed similar degradation problems in the segmentation of vessel boundaries. In their work, they derived an image force based on the gradient of one-dimensional (unidirectional) velocity as an alternative to the gradient of image intensity and showed the potential for using the velocity images from phase contrast. Similar to the case of vessel boundaries, the direction of the three-dimensional myocardial motion around the endocardial boundary can be significantly different from that of blood flow, especially around systolic phases, as shown in Figure 4. This fact can be used to derive a new image force to improve the accuracy of segmentation of the endocardial boundary. In this section, the tensor-based orientation gradient force is developed using the concept of the orientation tensor estimation and the velocity images from phase contrast MRI. It is incorporated into the generalized active contour model as an additional external force.

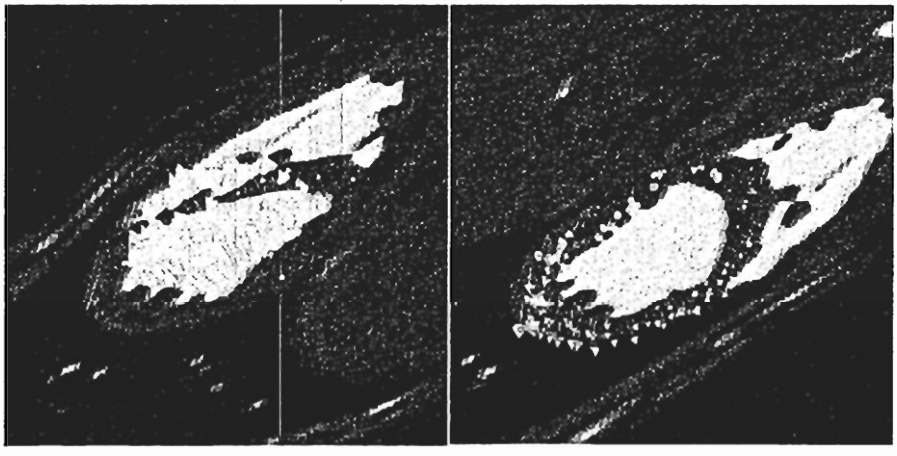

a) b)

Figure 4. Difference in the direction of the myocardial motion and blood flow. Three-dimensional velocity vectors are overlaid on both top and bottom sides of the same magnitude image slice at end systole. Vectors out of the image slice show a) superior directional blood flow and b) inferior directional myocardial motion.

3.4.1 Orientation Tensor

To quantitatively measure and differentiate the direction of the three-dimensional myocardial motion and blood flow, an appropriate measure is first needed. The orientation of three-component velocity vector fields is used for this purpose. Unlike two-dimensional vector whose orientation can be represented by a scalar value, such as the angle, the orientation of three-dimensional vector can not be directly represented by a scalar value. Furthermore, the concepts of deriving edges in two-dimensional scalar images, such as gray-scale images, do not extended directly to a higher order vector field

because the gradient of a vector field is not a scalar or a new vector, but a second order tensor. Hence, the concept of the orientation tensor [35] is used to represent the orientation of three-dimensional velocity vector fields from the three-directional velocity images.

The orientation is a local property of a signal and defined as a local gradient direction. It can be well defined in a simple neighborhood, where signals can locally vary in only one direction. For example, a neighborhood that contains a single edge or line has a well defined orientation, whereas neighborhoods that are low-contrast, contain substantial amounts of noise, or have several edges or lines do not have a well-defined orientation. A simple neighborhood can be formally expressed as:

$$s(\zeta) = g(\zeta \cdot \mathbf{x}') \tag{18}$$

where s and g are non-constant functions, ζ is the spatial coordinate vector, and $\mathbf{x}'$ is a normalized directional vector that is oriented along the axis of maximal signal variation. According to this definition, s is constant along any vector that is perpendicular to $\mathbf{x}'$. For this type of neighborhood, the local orientation can be entirely defined by $\mathbf{x}'$.

The entity, denoted as $\mathbf{T}$ here, representing the local orientation of a simple neighborhood should meet the following three basic requirements:

1) Invariance

2) Equivariance

3) Uniqueness

The invariance requirement means that $\mathbf{T}$ must be invariant to g in a strong sense. A more practical and weaker requirement is that the normalized entity $\mathbf{T}' = \mathbf{T}/\|\mathbf{T}\|$ must be invariant to g. The equivariance requirement means that if the orientation of the local neighborhood changes by a small amount, it should always result in a small change in $\mathbf{T}$. A more formal description of this requirement is that there must be a continuous mapping from $\mathbf{x}'$ to $\mathbf{T}$ and if making a small change in $\mathbf{x}'$, resulting in a small change also in $\mathbf{T}$, the norm of $\mathbf{T}$ should be invariant to $\mathbf{x}'$. The uniqueness requirement means that there is a unique representation $\mathbf{T}$ to each orientation. The entity for the local orientation of the neighborhood that meets these three requirements is a tensor of order two:

$$\mathbf{T} \equiv A\mathbf{x}'\mathbf{x}'^{T} \tag{19}$$

where A is an arbitrary positive number that doesn't depend on $\mathbf{x}'$ and $\mathbf{x}'^{T}$ is a transpose of $\mathbf{x}'$. $\mathbf{x}'$ is actually an eigenvector of $\mathbf{T}$, and A is the only non-zero eigenvalue of $\mathbf{T}$, so $\mathbf{T}$ is a tensor of rank one. It doesn't change when $\mathbf{x}'$ changes its sign. Thus, it is a one-to-one mapping and unique. It also satisfies the invariance requirement,

because $\mathbf{T}$ is invariant to g. To show that it satisfies the equivariance requirement, rotate $\mathbf{x}'$ by adding a small perpendicular vector $\varepsilon\mathbf{r}'$ to $\mathbf{x}'$ and calculate the difference in the norm of $\mathbf{T}$. Defining $d\mathbf{T}/d\varepsilon$ and carrying out the limit calculation yield:

$$\frac{d\mathbf{T}}{d\varepsilon} = \lim_{\varepsilon \to 0} \frac{\mathbf{T}(\mathbf{x}' + \varepsilon\mathbf{r}') - \mathbf{T}(\mathbf{x}')}{\varepsilon}$$
$$= A(\mathbf{x}'\mathbf{r}'^{T} + \mathbf{r}'\mathbf{x}'^{T}) \tag{20}$$

Then, the norm of $d\mathbf{T}/d\varepsilon$ is

$$\left\| \frac{d\mathbf{T}}{d\varepsilon} \right\| = \sqrt{2}A \tag{21}$$

This shows that a small change in $\mathbf{x}'$ results in a small change in $\mathbf{T}$, and the norm of the differential is independent of both $\mathbf{x}'$ and $\mathbf{r}'$. Thus, it satisfies the equivariance requirement.

3.4.2 Orientation Estimation

The local orientation of three-dimensional velocity vector fields can now be represented by the orientation tensor described in the previous section. The orientation tensor is constructed by combining the output magnitudes from quadrature filters [36]. Each quadrature filter is spherically separable and real in the Fourier domain and given by:

$$F_k(\mathbf{u}) = R(\rho) D_k(\mathbf{u}') \tag{22}$$

where $\mathbf{u}$ is the frequency, $\rho = \|\mathbf{u}\|$, and $\mathbf{u}' = \mathbf{u}/\rho$. The radial function R is a band-pass function given by:

$$R(\rho) = \mathrm{e}^{-\frac{4}{B^2 \ln 2} \ln^2(\rho/\rho_i)} \tag{23}$$

where B is the relative bandwidth and ρ_i is the center frequency. The directional function D_k is given by:

$$D_k(\mathbf{u}') = \begin{cases} (\mathbf{u}' \cdot \mathbf{n}_k')^2, & \mathbf{u}' \cdot \mathbf{n}_k' > 0 \\ 0, & \text{otherwise} \end{cases} \tag{24}$$

where $\mathbf{n}_k'$ is the kth filter directing vector. Thus $D(\mathbf{u}')$ varies as $\cos^2(\theta)$, where θ is the difference in angle between u and the filter direction $\mathbf{n}_k'$. Then, the orientation tensor for three-component velocity vector fields is constructed by:

$$\mathbf{T} = \sum_{k=1}^{4} \left(\sum_{l=1}^{3} q_{kl}^2 \right)^{\frac{1}{2}} \left(\mathbf{N}_k' - \frac{1}{4} \mathbf{I} \right) \tag{25}$$

where q_{kl} is the output magnitude of kth quadrature filter obtained by filtering the lth velocity image out of three(x, y, and z)-directional velocity images, $\mathbf{N}_k'$ is the outer product of the kth filter directing vector $\mathbf{n}_k'$ and $\mathbf{n}_k'^T$, and $\mathbf{I}$ is an identity tensor. The detailed derivation of the above equation can be found in [35].

3.4.3 External Force Construction

The estimated orientation tensor **T** represents the local variation in the velocity vector fields, and its norm corresponds to the local energy of the variation. Thus, the edges of the three-component velocity vector fields from the three-directional velocity images are obtained from this tensor and used to derive a new image force, called tensor-based orientation gradient force (OGF). The OGF is defined as:

$$E_{orientation}(\mathbf{v}_i) = (1 - \mathbf{h}_i^T o(\mathbf{v}_i)) \tag{26}$$

where $o(\mathbf{v}_i)$ is an orientation feature function that produces the orientation gradient vectors from the norm of the orientation tensor, $\mathbf{h}_i$ is the unit normal vector at $\mathbf{v}_i$, and $\|\mathbf{h}_i\| = 1$.

The estimation of the local orientation tensor assumes that a neighborhood be simple as described in section 3.4.1. However, it is apparent that not all neighborhoods are simple in real data, such as the velocity vector fields. Consequently, the estimated orientation tensor is not a rank one tensor. The tensor **T** describes the directions of both the maximum change and minimum change, and the corresponding eigenvalues describe the rate of change in each direction. Therefore, some method of interpreting the estimated orientation tensor is needed to reliably incorporate the OGF into the generalized active

contour model. Rank one approximation of $\mathbf{T}$ and a resulting certainty measure are used for this purpose.

Because the estimated orientation tensor, not necessarily a rank one, is always symmetric, it can be decomposed into

$$\mathbf{T} = \sum_{k=1}^{2} \lambda_k \mathbf{e}_k' \mathbf{e}_k'^T \tag{27}$$

where $\mathbf{e}_k'$ is an eigenvector of $\mathbf{T}$ and λ_k is the corresponding eigenvalue. For a non-simple neighborhood, the orientation tensor $\mathbf{T}$ doesn't have only one nonzero eigenvalue and can even have a negative eigenvalue. The convention of setting any negative eigenvalue of $\mathbf{T}$ to zero is used here for interpretation purposes. Let $\mathbf{T}_s$ be a rank one tensor, then it can be expressed as:

$$\mathbf{T}_s = \lambda_s \mathbf{e}_s' \mathbf{e}_s'^T \tag{28}$$

If $\mathbf{T}_s$ minimizes

$$\varepsilon = \|\mathbf{T}\text{-}\mathbf{T}_s\|^2 = \left\|\mathbf{T} - \lambda_s \mathbf{e}_s' \mathbf{e}_s'^T\right\|^2 \tag{29}$$

then, $\mathbf{T}_s$ is refer to a rank one approximation of $\mathbf{T}$. It can be shown that any rank one approximation $\mathbf{T}_s$ of $\mathbf{T}$ is such that λ is the largest eigenvalue of $\mathbf{T}$ with $\mathbf{e}'$ as the corresponding eigenvector, i.e., $\lambda_s = \lambda_1$ and $\mathbf{e}_s' = \mathbf{e}_1'$ when $\lambda_1 \geq \lambda_2$. With the rank one approximation $\mathbf{T}_s$, the approximation error ε becomes

$$\varepsilon = \left\| \sum_{k=1}^{2} \lambda_k \mathbf{e}_k' \mathbf{e}_k'^T - \lambda_1 \mathbf{e}_1' \mathbf{e}_1'^T \right\|^2 = \lambda_2^2 \tag{30}$$

From this error estimation, a useful measure that indicates the certainty of a rank one approximation of **T** can be defined as:

$$\chi = \frac{\lambda_1 - \lambda_2}{\lambda_1}, \quad \begin{cases} 0 \le \chi_i \le 1 \\ \lambda_1 \ge \lambda_2 \end{cases} \tag{31}$$

$\chi \approx 1$ indicates that **T** is approximately a rank one tensor, corresponding to a simple neighborhood. In other words, χ represents the certainty of the local orientation in the velocity vector fields (i.e., how much reliable the measured local orientation variation is). Therefore, this certainty measure can be used as a weighting factor to combine the OGF with the conventional intensity gradient force.

A new external force for the generalized active contour model is now constructed by combining the OGF with the intensity gradient force described in section 3.3 using the certainty measure χ:

$$E_{new\_ext}(v_i) = (1 - \chi_i) E_{ext}(v_i) + \chi_i E_{orientation}(v_i) \tag{32}$$

This force can effectively incorporate the velocity-based external force into the generalized active contour model. In practice, χ is normalized because the estimated values of its components are usually high ($\chi \approx 0.8$) and have a small dynamic range.

3.5 Energy Minimization

The discrete dynamic programming approach [37] is used to find the solution set of points with the minimum energy of E_{total}. Instead of using an exhaustive search, the minimization process is decomposed into n independent stages, where each stage uses only 3 neighboring points. Because the energy decreases monotonically in this process, the solution is guaranteed to converge in a finite number of iterations. Denote the ordered set of contour points $P = [\mathbf{v}_1, \mathbf{v}_2, \ldots, \mathbf{v}_n]$. Then, the solution set P_j^* at iteration j is

$$P_j^* = \arg\min_P \sum_{i=1}^{n} E_i(\mathbf{v}_{i-1}, \mathbf{v}_i, \mathbf{v}_{i+1}) \tag{33}$$

where E_i is a state variable defined by:

$$E_i(\mathbf{v}_{i-1}, \mathbf{v}_i, \mathbf{v}_{i+1}) = \mu_i E_{int}(\mathbf{v}_i) + (1-\mu_i) E_{new\_ext}(\mathbf{v}_i) \tag{34}$$

The minimization process starts with m_1:

$$m_1(\mathbf{v}_2, \mathbf{v}_3) = \min_{\mathbf{v}_1} \{E_1(\mathbf{v}_3, \mathbf{v}_1, \mathbf{v}_2) + E_2(\mathbf{v}_1, \mathbf{v}_2, \mathbf{v}_3)\} \tag{35}$$

For the next stage, s_1 and E_3 are used to obtain

$$\begin{aligned} m_2(\mathbf{v}_3, \mathbf{v}_4) &= \min_{\mathbf{v}_2} \{m_1(\mathbf{v}_2, \mathbf{v}_3) + E_3(\mathbf{v}_2, \mathbf{v}_3, \mathbf{v}_4)\} \\ &= \min_{\mathbf{v}_2, \mathbf{v}_1} \sum_{i=1}^{3} E_i(\mathbf{v}_{i-1}, \mathbf{v}_i, \mathbf{v}_{i+1}) \end{aligned} \tag{36}$$

Continuing with the similar fashion, the general recurrence relation m_i for $i = 3$ through $i = n - 3$ is obtained:

$$m_i(\mathbf{v}_{i+1}, \mathbf{v}_{i+2}) = \min_{\mathbf{v}_i}\{m_{i-1}(\mathbf{v}_i, \mathbf{v}_{i+1}) + E_{i+1}(\mathbf{v}_i, \mathbf{v}_{i+1}, \mathbf{v}_{i+2})\} \tag{37}$$

Then, the process is completed in stage n-2 as follows:

$$m_{i-2}(\mathbf{v}_{n-1}, \mathbf{v}_n) = \min_{\mathbf{v}_{n-2}}\{m_{i-3}(\mathbf{v}_{n-2}, \mathbf{v}_{n-1}) + E_{n-1}(\mathbf{v}_{n-2}, \mathbf{v}_{n-1}, \mathbf{v}_n) + E_n(\mathbf{v}_{n-1}, \mathbf{v}_n, \mathbf{v}_{n-2})\} \tag{38}$$

$$\min_{\mathbf{v}_{n-1}, \mathbf{v}_n} m_{n-2}(\mathbf{v}_{n-1}, \mathbf{v}_n) = \min_P \sum_{i=1}^{n} E_i(\mathbf{v}_{i-1}, \mathbf{v}_i, \mathbf{v}_{i+1}) \tag{39}$$

Finally, backward substitution produces a solution set P_j^* from $i = n - 1$ and $i = n$ to $i =$ 1:

$$\begin{aligned} \{\mathbf{v}_{n-1}^*, \mathbf{v}_n^*\} &= \arg \min_{\mathbf{v}_{n-1}, \mathbf{v}_n} m_{n-2}(\mathbf{v}_{n-1}, \mathbf{v}_n) \\ \mathbf{v}_i^* &= \arg \min_{\mathbf{v}_i} m_{i-1}(\mathbf{v}_i, \mathbf{v}_{i+1}^*) \end{aligned} \tag{40}$$

To obtain a final solution set V^*, the above minimization process is iterated until the energy of the contour cannot be further reduced:

$$V^* = P_j^*, \qquad \text{if } P_j^* = P_{j-1}^*, \text{ where } j = 1, 2, \ldots \tag{41}$$

3.6 Sequential Frame Segmentation

As described previously, manual segmentation of the myocardial boundaries is reliable, but too time consuming in practice. Semiautomatic segmentation, such as active contour models that generally use an automatic process in sequential frame segmentation, also requires considerable human intervention to correct the segmentation errors and their

propagation during the entire segmentation process. Because most active contour models use a segmented boundary as an initial seed contour for the subsequent frame, the propagation of errors in automatic sequential frame segmentation of the myocardial boundaries can be significant where there are considerable changes in position and shape of the boundaries. Hence, a method, which minimizes the propagation of errors in automatic sequential frame segmentation of the myocardial boundaries with a minimum human intervention, is desirable. Tracking the motion of a segmented contour using the velocity information from phase contrast MRI is the proposed solution for minimizing the propagation of errors, because an initial seed contour placed closer to the desired boundary generally reduces the segmentation errors from the effect of a false local minimum in an active contour model. In this section, the SCT algorithm for the segmentation method developed in previous sections is developed with the goal of reducing the propagation of errors in automatic sequential frame segmentation of the myocardial boundaries, especially the endocardial boundary.

Before applying the SCT algorithm, the locations of pixels on a segmented endocardial boundary should be carefully examined in a pixel-by-pixel basis because they may be either in the region of the myocardium or blood pool due to segmentation

errors. Poor tracking of the boundary pixels in the region of blood pool will result in the tracked initial seed contour containing significant errors because the velocity values in blood pool near the endocardial boundary can be significantly different from those in nearby myocardium as previously described. Hence, an appropriate selection and displacement of a segmented boundary pixel is first needed to ensure that all the boundary pixels to be tracked are located in the region of the myocardium. Define the average orientation tensor energy in the neighborhood around a segmented endocardial boundary pixel:

$$E_{\mathbf{T}} = \frac{1}{n}\sum_{i=1}^{n}\|\mathbf{T}_i\| \tag{42}$$

where $\|\mathbf{T}_i\|$ is the norm of the neighboring pixel's orientation tensor around the segmented boundary pixel. Then, this average orientation tensor energy is compared with the energies calculated at pixels located in the normal-outer direction to the segmented boundary, and the pixel with the lowest energy is selected as a new location of the boundary pixel. Practically, the neighborhood is chosen to be a 3×3 window centered at the segmented boundary pixel of interest, and a search region is limited to 3 pixels in the normal-outer direction of the segmented endocardial boundary for the LV. Because the average orientation tensor energy measured at the endocardial boundary usually has a

higher value than the region of the myocardium, displacing the segmented boundary pixel to the location with a lower energy will more likely place the boundary pixel in the region of the myocardium (away from the region of the blood pool). Then, tracking the segmented boundary pixel located in the region of the blood pool can be mostly avoided so that a false prediction of the position of an initial seed contour can be minimized.

Now, the initial seed contour tracking for the subsequent frame is performed by integrating velocity components on the segmented and displaced endocardial boundary pixels as a function of time [8]:

$$f(t) = \int v[f(\tau)]d\tau \tag{43}$$

where $f(t)$ represents one of the three Cartesian coordinates of the boundary trajectory and v is one of the velocity components. In practice, this integral is replaced by a summation over the velocity:

$$f_{k+1} = f_k + v(f_k, t_k)\Delta t \tag{44}$$

where f_{k+1} is the position of a tracked initial seed contour at time t_{k+1}, k is the current frame number, $v(f_k, t_k)$ denotes the velocity at the position of a segmented contour at time t_k, and Δt is the temporal resolution of a phase contrast MR data set. The out-of-plane (z) component of the tracked contour position is projected onto the imaging plane. Because

the positions of pixels on the previously segmented boundary contour are tracked using available velocity information, the resulting initial seed contour for the subsequent frame using this method can be closer to the desired boundary when there are considerable changes in positions and shapes of the endocardial boundaries between the two subsequent frames. Then, the effect of a false local minimum (or segmentation errors) in automatic sequential boundary segmentation can be reduced. The SCT algorithm is repeated sequentially between two subsequent frames until all the cardiac frames are processed. An overview of the entire segmentation process is given in Figure 5.

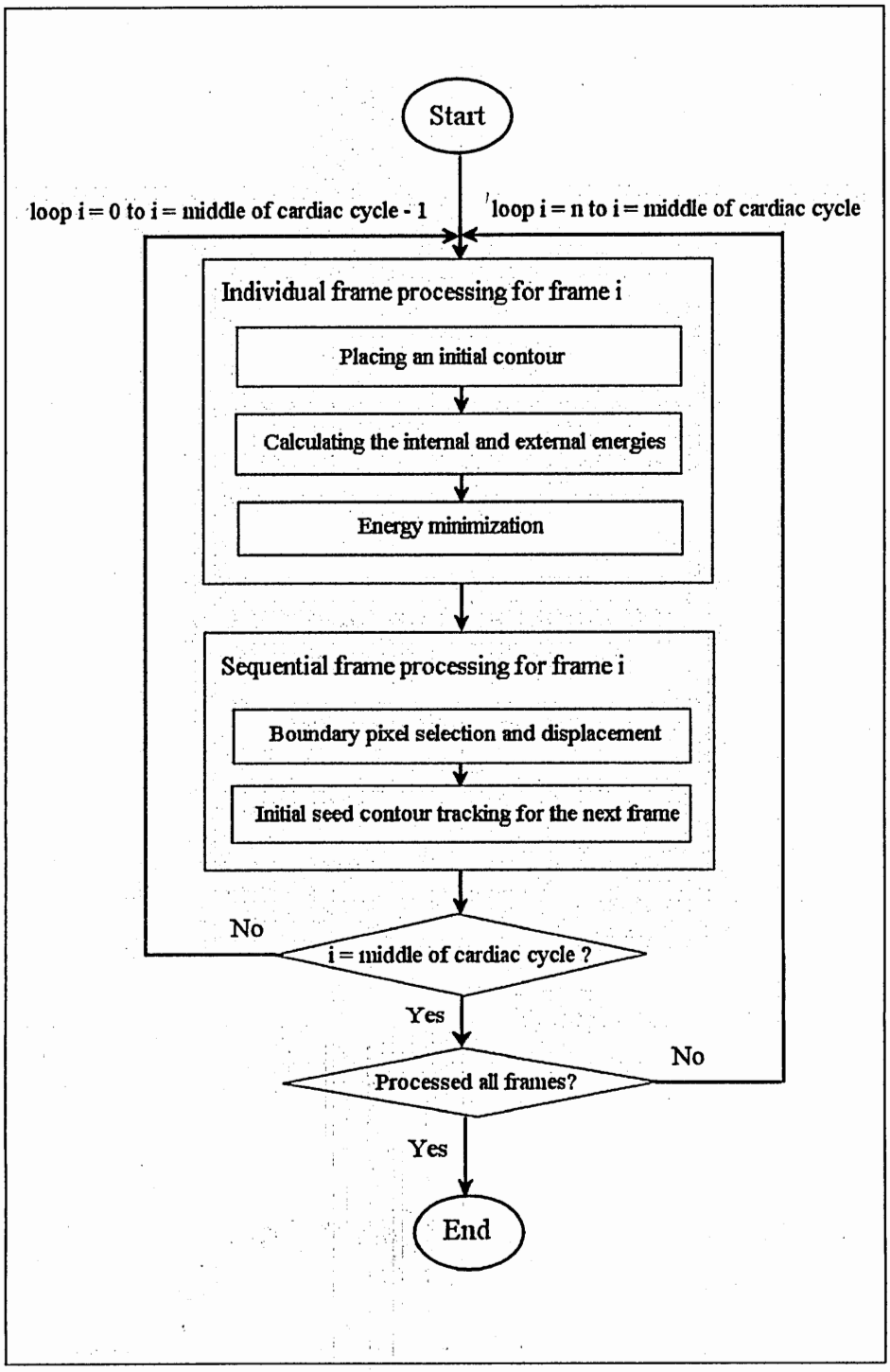

Figure 5. Overview of segmentation process for the entire cardiac cycle. The total number of cardiac frames is denoted by n.

3.7 Experimental Results

In this section, the performance of the proposed cardiac segmentation method is quantitatively assessed. Individual frame segmentation and sequential frame segmentation of the human LV and RV are separately examined, and results are compared with those obtained by manual segmentation.

3.7.1 Data Acquisition

A phase contrast MRI data set of a normal human volunteer was acquired by Philips Gyroscan Intera 1.5T MRI scanner at the Frederik Philips Magnetic Resonance Research Center in the Department of Radiology at Emory University. A single human subject (male, 22 year-old) was scanned once. Scan parameters of the breath-held segmented echo-planar imaging (EPI) scans were as follows: 20 cardiac frames, 8 short axis slices (each slice sequence was acquired per breathhold), 41-msec temporal resolution, 256× 256 in-plane resolution, 350-mm field of view, 10-mm slice thickness, 1-mm slice distance, and 50-cm/sec velocity encoding in three orthogonal directions. Stacks of slices and a set of phase contrast MR images at end diastole are shown in Figure 6.

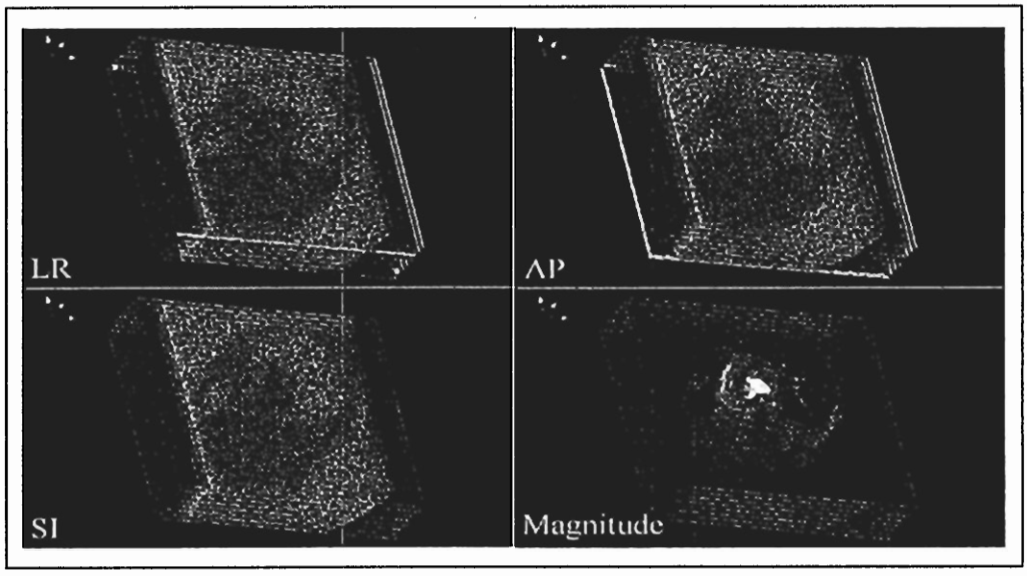

a)

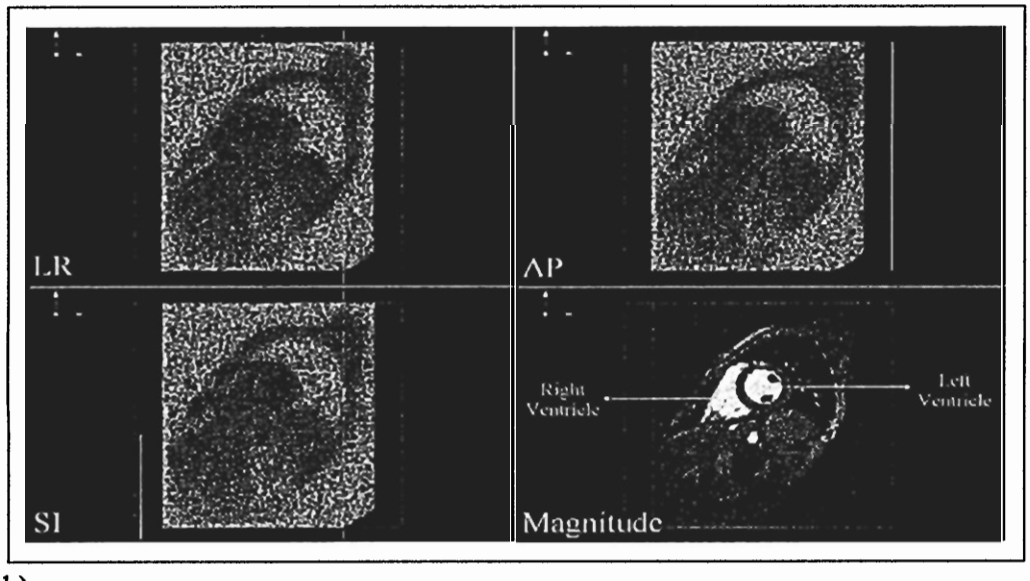

b)

Figure 6. A phase contrast MRI data set of a normal human volunteer. a) Stacks of 8 slices at end diastole are visualized, and b) mid-ventricle slices at end diastole. LR, AP, and SI indicate the velocity encoding directions in left-right, anterior-posterior, and superior-inferior, respectively. Magnitude indicates the magnitude image.

3.7.2 Quantitative Measures for Performance Assessment

Although the visual inspection of segmented boundaries is the simplest way for assessing the accuracy of segmentation, it is qualitative and subjective. Thus, a quantitative measure is needed to objectively assess the accuracy of segmentation. The boundary matching descriptors (BMD) [39, 40] and the linear correlation coefficients (LLC) [41] are used to quantitatively assess the performance of the proposed segmentation methods in this thesis.

The BMD is a measure of shape-similarity between the myocardial boundaries. Define the gradient *Grad*[*i*] at each manually segmented reference boundary point *i*:

$$Grad[i] = \frac{1}{d}\sum_{j=1}^{d}\left|I[i,j] - I[i,-j]\right|, \quad 0 \le i \le n \tag{45}$$

where *I*[*i*, -*d*:*d*] is the intensity level at each point along the line normal to the boundary, *d* is a distance interval from point *i*, and *n* is the total number of sampled boundary points. Let CD[*i*] be a confidence distance along the normal line defined at point *i*. Then, the confidence distance, which is inversely proportional to the gradient, is defined as:

$$\mathrm{CD}[i] = \frac{d}{Grad'[i]} \tag{46}$$

where $Grad'[i]$ is the gradient, which is linearly scaled such that

$$1 \le Grad'[i] \le d \tag{47}$$

Given a value of the distance d, CD[i] is calculated and lies between a value of one pixel and d pixels. Practically, the value of d is chosen as 3 for the LV and 2 for the RV depending on the myocardial thicknesses. If CD[i] is small (i.e., the gradient is large), the border can be easily identified. Similarly, if CD[i] is large, the border is ambiguous. Then, the BMD is defined as the ratio of the total number of points in a comparing boundary within the confidence distance of a reference boundary (the number of matches) to the number of points outside of the confidence distance (the number of mismatches). Instead of directly using the BMD, a modified definition of the BMD is used for normalization purposes:

$$\text{BMD}(\%) = \frac{\text{Number of boundary points within the confidence distance}}{\text{Total number of boundary points}} \times 100 \qquad (48)$$

The LLC is a measure of how likely it is that a manually segmented reference boundary and a segmented boundary by the proposed methods are correlated. The LLC is defined by:

$$\text{LLC} = \left| \frac{\sum_{i=1}^{n} (R_i - < R >)(C_i - < C >)}{\sqrt{\sum_{i=1}^{n} (R_i - < R >)^2 \sum_{i=1}^{n} (C_i - < C >)^2}} \right| \qquad (49)$$

where n is the total number of sampled boundary points, R_i is a signature value (radius measured with the center of mass) of the manually segmented reference boundary, $<R>$ is

a mean signature value, C_i is a signature value of the segmented boundary by the proposed methods, and <C> is a mean signature value. If the two boundaries are exactly correlated with each other in a linear sense, then LLC should be one. Similarly, if there's no correlation between the two boundaries, then LLC should be zero.

3.7.3 Individual Frame Segmentation

Experiments of individual frame segmentation were performed on the entire cardiac cycle (20 frames) and three different longitudinal levels (apex, mid-ventricle, and base) of both the LV and RV as follows:

1) Each frame was segmented ten times using both the segmentation methods with and without the OGF.
2) In each segmentation, an initial seed contour was placed manually around the desired endocardial boundary by the same observer.
3) The BMD and LCC values of the segmented boundaries were calculated relative to the manually segmented reference boundaries and averaged over ten different trials.

4) The BMD and LCC values from the segmentation methods with and without the OGF were compared.

At the apical level of the LV, mean BMDs and LCCs from both the segmentation methods with and without the OGF decreased toward the end systole (frame 8) because the boundaries around the end systole were concave and easily corrupted by nearby points with high external forces. However, because the three-dimensional motion differences between the myocardium and blood flow increased around end systole, the improvements in mean BMDs and LCCs by the OGF also increased around the end systole. The intra-observer variability of segmentation caused by manually placed initial seed contours, which were slightly different with each segmentation, decreased by the use of the OGF especially around end systole. Around end diastole, mean BMDs and LCCs from both methods were similar. These results are shown in Figure 7, and quantitative comparisons of BMDs and LCCs at selected frames are shown in Table 1. Because the calculation of LCC assumes a circular shape of the boundary, only BMDs were measured for the boundaries of the RV. At the apical level of the RV, lower mean BMDs were obtained around early systole because of the ambiguous boundary delineation due to the presence of papillary muscles. The use of the OGF reduced the effect of papillary

muscles and resulted in higher mean BMDs. However, improvements in the intra-observer variability were negligible throughout the entire cardiac cycle. Figure 8 shows the results of segmentation of the RV, and Table 2 shows comparisons of BMDs.

Similar to the apical level, mean BMDs and LCCs at the mid-LV decreased toward end systole, and the improvements in mean BMDs and LCCs by the OGF increased around end systole, as shown in Figure 9. Note that BMDs and LCCs at frame 12 and 14 show the effect of flow-related signal loss. This effect was reduced by the use of the OGF. The intra-observer variability in BMDs also decreased around the end systole, as shown in Table 3. At the mid-RV, similar results were obtained, but the magnitude of BMDs and improvements were generally less than those at the mid-LV, as shown in Figure 10. Comparisons of mean BMDs are shown in Table 4.

At the basal level, the overall performance improvement by the use of the OGF was less than at other ventricle levels. This might be because of the velocity wrap-around problem of phase contrast MRI (around frame 10) and blood turbulence around the valves. The velocity wrap-around problem produces high external forces that attract the boundary to the false minima, and non-consistent blood flow produces ambiguous orientation edges that lower the effect of the orientation gradient force. The intra-observer

variability was also affected by these problems. Figure 11, Figure 12, Table 5, and Table 6 show the results of individual frame segmentation at the basal level.

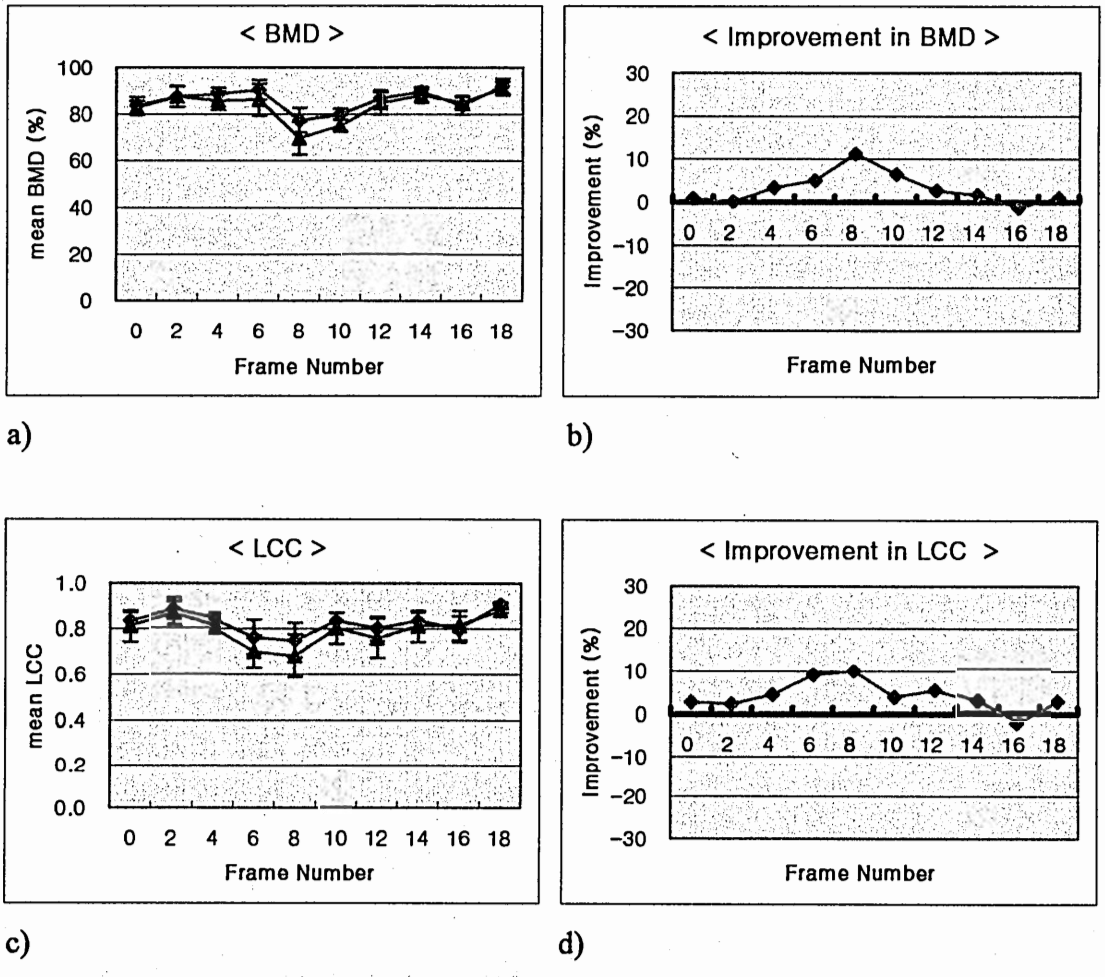

Figure 7. Performance graphs of individual frame segmentation at the apical level of the LV. Mean boundary matching descriptor (BMD) values and mean linear correlation coefficient (LCC) values of ten selected frames are given in a) and c) respectively. Improvements in mean BMDs and mean LCCs are given in b) and d) respectively. Blue in a) and c) indicates the results with the OGF, and magenta in a) and c) indicates the results without the OGF. Error bars in a) and c) represent the standard deviations.

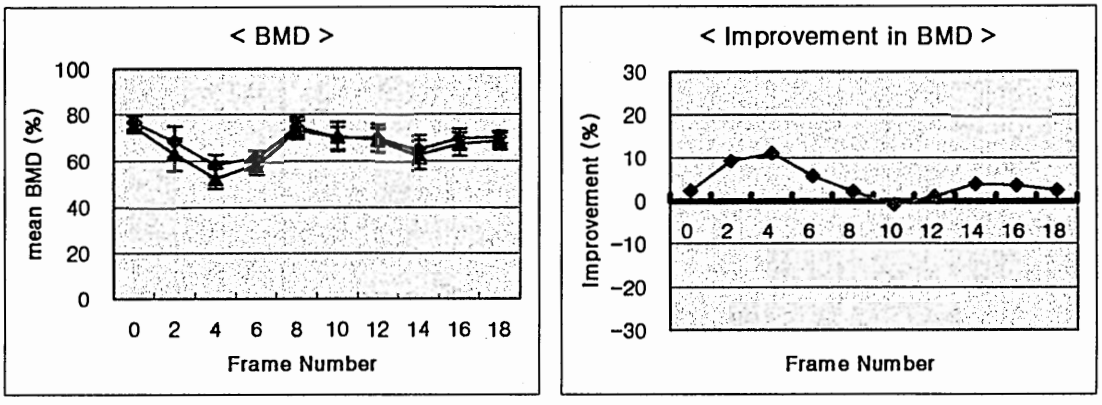

a) b)

Figure 8. Performance graphs of individual frame segmentation at the apical level of the RV. Mean boundary matching descriptor (BMD) values of ten selected frames are given in a). Improvements in mean BMDs are given in b). Blue in a) indicates the results with the OGF, and magenta in a) indicates the results without the OGF. Error bars in a) represent the standard deviations.

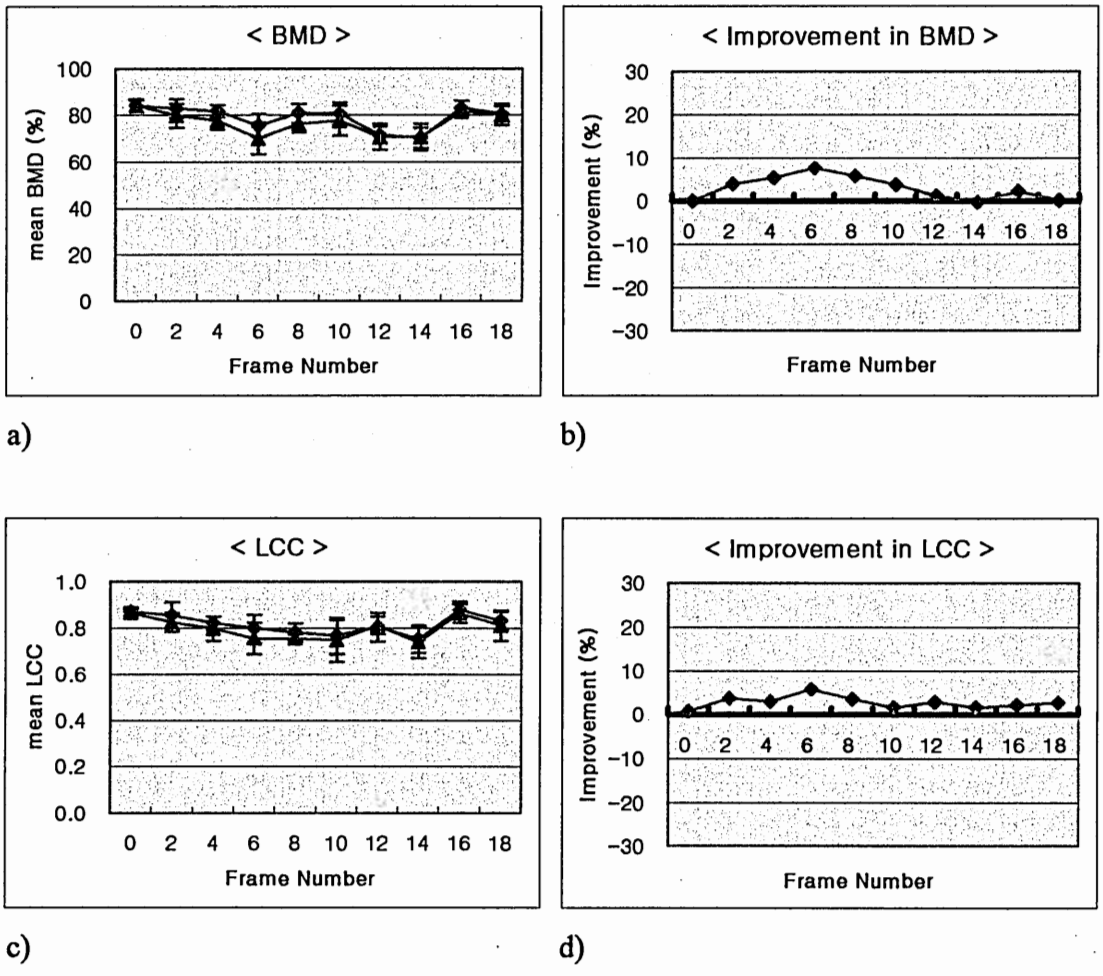

Figure 9. Performance graphs of individual frame segmentation at the mid-ventricular level of the LV. Mean boundary matching descriptor (BMD) values and mean linear correlation coefficient (LCC) values of ten selected frames are given in a) and c) respectively. Improvements in mean BMDs and mean LCCs are given in b) and d) respectively. Blue in a) and c) indicates the results with the OGF, and magenta in a) and c) indicates the results without the OGF. Error bars in a) and c) represent the standard deviations.

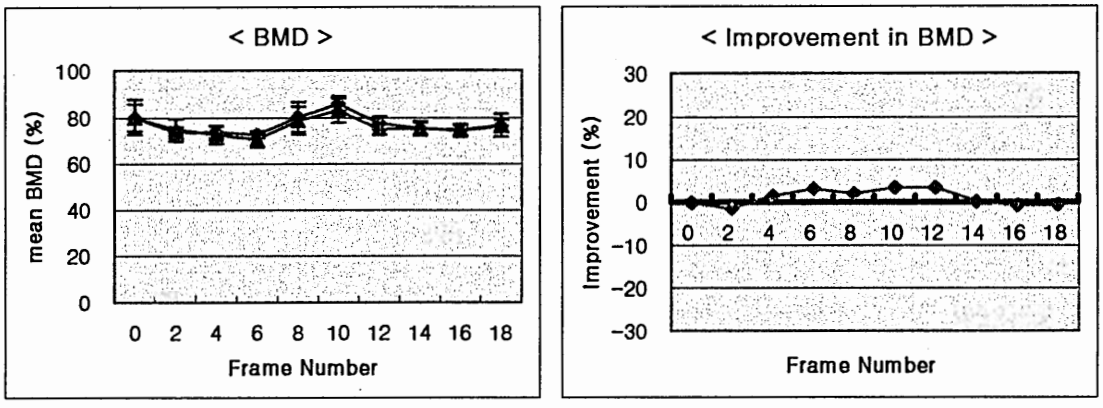

a) b)

Figure 10. Performance graphs of individual frame segmentation at the mid-ventricular level of the RV. Mean boundary matching descriptor (BMD) values of ten selected frames are given in a). Improvements in mean BMDs are given in b). Blue in a) indicates the results with the OGF, and magenta in a) indicates the results without the OGF. Error bars in a) represent the standard deviations.

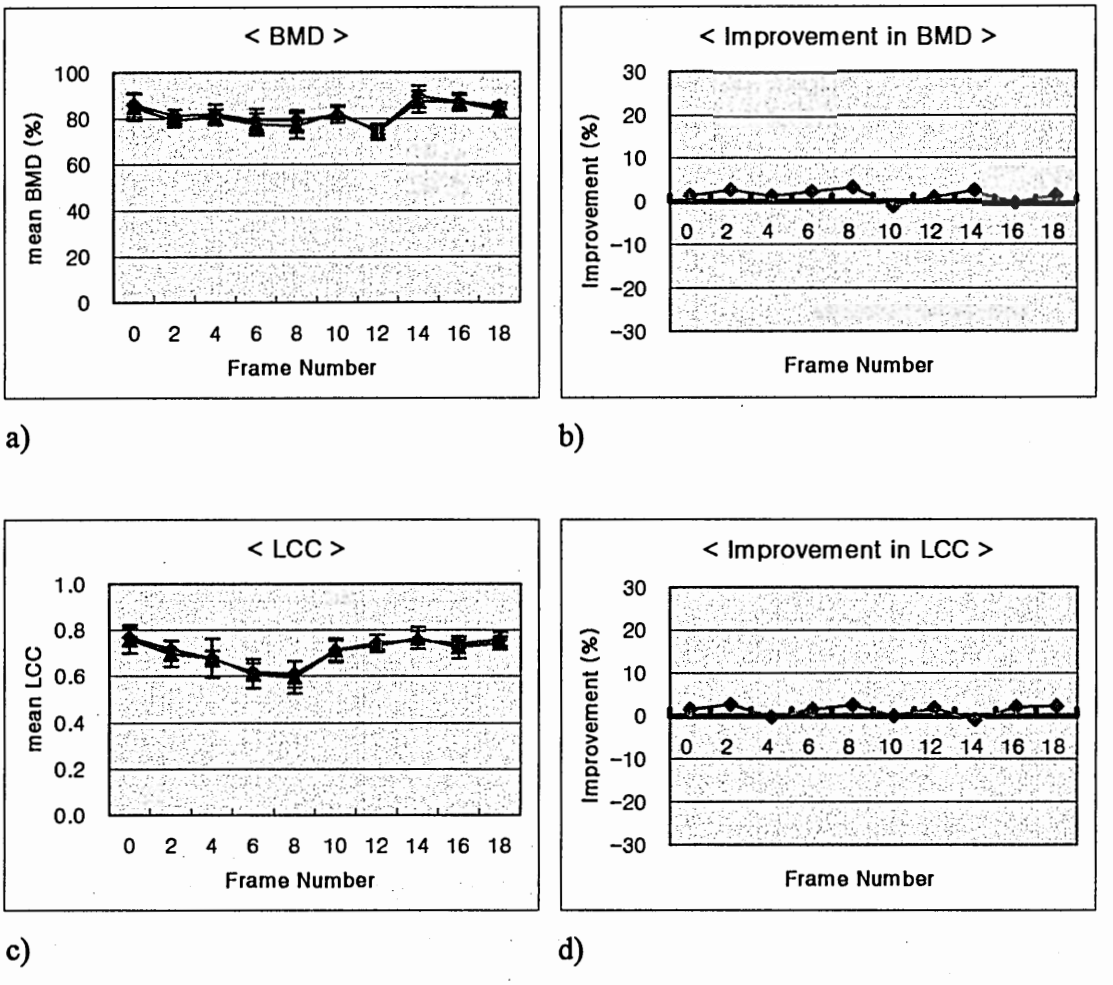

Figure 11. Performance graphs of individual frame segmentation at the basal level of the LV. Mean boundary matching descriptor (BMD) values and mean linear correlation coefficient (LCC) values of ten selected frames are given in a) and c) respectively. Improvements in mean BMDs and mean LCCs are given in b) and d) respectively. Blue in a) and c) indicates the results with the OGF, and magenta in a) and c) indicates the results without the OGF. Error bars in a) and c) represent the standard deviations.

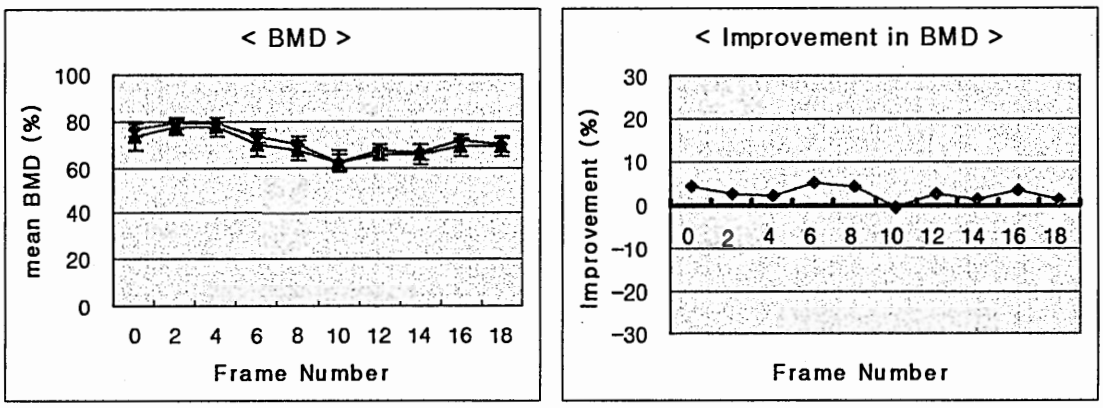

a) b)

Figure 12. Performance graphs of individual frame segmentation at the basal level of the RV. Mean boundary matching descriptor (BMD) values of ten selected frames are given in a). Improvements in mean BMDs are given in b). Blue in a) indicates the results with the OGF, and magenta in a) indicates the results without the OGF. Error bars in a) represent the standard deviations.

Table 1. Results of individual frame segmentation at the apical level of the LV. Endocardial boundary in a frame was segmented ten times by the same observer. In each segmentation, an initial seed contour was placed manually. The boundary matching descriptor (BMD) and the linear correlation coefficient (LCC) are mean ± standard deviation.

	With OGF		Without OGF	
Frame Number	BMD (%)	LCC	BMD (%)	LCC
0	83.40±3.76	0.832±0.038	82.72±2.90	0.810±0.067
2	87.44±4.27	0.882±0.047	87.40±4.50	0.862±0.052
4	88.48±2.85	0.840±0.025	85.56±4.04	0.804±0.029
6	90.44±4.14	0.762±0.075	86.20±6.85	0.698±0.072
8	77.48±5.29	0.748±0.072	69.70±7.18	0.680±0.094
10	79.86±1.70	0.832±0.038	75.06±2.69	0.801±0.067
12	86.80±3.34	0.800±0.052	84.50±4.74	0.758±0.086
14	89.58±1.30	0.832±0.038	88.16±3.28	0.810±0.067
16	83.58±3.67	0.798±0.055	84.80±3.02	0.814±0.064
18	91.94±3.17	0.904±0.011	91.08±2.92	0.878±0.008

Table 2. Results of individual frame segmentation at the apical level of the RV. Endocardial boundary in a frame was segmented ten times by the same observer. In each segmentation, an initial seed contour was placed manually. The boundary matching descriptor (BMD) is mean ± standard deviation.

	With OGF	Without OGF
Frame Number	BMD (%)	BMD (%)
0	76.78±2.48	75.10±1.39
2	68.54±4.70	62.80±5.18
4	58.02±4.89	52.24±4.49
6	61.50±3.56	58.20±4.18
8	75.08±3.58	73.50±3.82
10	70.08±5.03	70.68±6.26
12	70.10±5.87	69.42±5.14
14	65.00±6.34	62.64±6.41
16	69.76±4.43	67.34±5.11
18	70.44±2.70	68.78±3.61

Table 3. Results of individual frame segmentation at the mid-ventricle level of the LV. Endocardial boundary in a frame was segmented ten times by the same observer. In each segmentation, an initial seed contour was placed manually. The boundary matching descriptor (BMD) and the linear correlation coefficient (LCC) are mean ± standard deviation.

	With OGF		Without OGF	
Frame Number	BMD (%)	LCC	BMD (%)	LCC
0	83.94±2.93	0.872±0.019	83.92±2.56	0.866±0.015
2	82.76±4.07	0.854±0.057	79.68±5.04	0.824±0.042
4	81.64±3.67	0.820±0.031	77.54±3.73	0.796±0.053
6	75.44±4.76	0.798±0.061	70.12±6.68	0.754±0.067
8	80.70±4.01	0.781±0.038	76.36±4.88	0.754±0.017
10	79.50±4.86	0.756±0.079	77.62±5.43	0.744±0.089
12	75.60±3.59	0.804±0.043	71.76±5.51	0.782±0.059
14	75.42±4.32	0.750±0.059	72.66±5.55	0.738±0.067
16	82.96±3.10	0.880±0.034	81.22±1.35	0.862±0.041
18	80.36±3.33	0.832±0.038	80.30±4.55	0.810±0.067

Table 4. Results of individual frame segmentation at the mid-ventricle level of the RV. Endocardial boundary in a frame was segmented ten times by the same observer. In each segmentation, an initial seed contour was placed manually. The boundary matching descriptor (BMD) is mean ± standard deviation.

	With OGF	Without OGF
Frame Number	BMD (%)	BMD (%)
0	79.86±5.89	79.94±7.68
2	73.36±2.64	74.42±4.87
4	73.48±2.62	72.40±3.95
6	72.40±1.65	70.18±3.06
8	80.14±6.47	78.58±6.27
10	85.90±3.16	83.04±5.26
12	77.42±2.98	74.78±2.50
14	75.16±2.49	75.08±3.27
16	73.92±2.52	74.50±2.44
18	76.04±2.90	76.44±5.10

Table 5. Results of individual frame segmentation at the basal level of the LV. Endocardial boundary in a frame was segmented ten times by the same observer. In each segmentation, an initial seed contour was placed manually. The boundary matching descriptor (BMD) and the linear correlation coefficient (LCC) are mean ± standard deviation.

	With OGF		Without OGF	
Frame Number	BMD (%)	LCC	BMD (%)	LCC
0	86.02±5.15	0.768±0.041	84.90±5.68	0.758±0.061
2	81.32±2.35	0.714±0.042	79.22±1.30	0.696±0.055
4	81.78±4.44	0.676±0.033	80.78±3.25	0.678±0.085
6	79.16±5.27	0.618±0.039	77.48±4.66	0.610±0.063
8	79.26±4.37	0.608±0.058	76.82±5.60	0.594±0.072
10	81.58±3.59	0.712±0.043	82.54±3.20	0.712±0.052
12	74.92±1.96	0.742±0.036	74.20±3.34	0.730±0.016
14	89.48±4.86	0.756±0.038	87.24±4.76	0.763±0.047
16	86.96±3.75	0.738±0.019	86.92±3.08	0.724±0.048
18	85.08±1.29	0.758±0.031	83.60±3.29	0.742±0.028

Table 6. Results of individual frame segmentation at the basal level of the RV. Endocardial boundary in a frame was segmented ten times by the same observer. In each segmentation, an initial seed contour was placed manually. The boundary matching descriptor (BMD) is mean ± standard deviation.

	With OGF	Without OGF
Frame Number	BMD (%)	BMD (%)
0	76.38±3.68	73.26±4.78
2	78.82±2.63	76.96±3.31
4	78.70±2.59	77.00±4.31
6	73.24±2.90	69.58±5.10
8	69.94±3.27	67.04±4.43
10	62.18±3.47	62.52±3.54
12	67.24±2.55	65.64±3.20
14	66.44±3.71	65.80±4.35
16	71.32±2.55	68.84±3.84
18	69.60±3.57	68.84±3.84

3.7.4 Sequential Frame Segmentation

The testing for sequential frame segmentation was performed on the same data set used for individual frame segmentation (20 frames at three different longitudinal levels in both the LV and RV as follows:

1) A sequence at each longitudinal level of each ventricle was segmented five times using both the segmentation methods with and without the SCT.
2) In each segmentation, an initial seed contour for the first frame of the sequence was placed manually around the desired endocardial boundary by the same observer.
3) Sequential frame segmentation was performed automatically in both forward and backward time direction up to the middle of cardiac cycle (i.e., frame 0 to 9 and frame 19 to 10, respectively).
4) The BMD and LCC values of the segmented boundaries were calculated relative to the manually segmented reference boundaries and averaged over five different trials.
5) The BMD and LCC values from the segmentation methods with and without the SCT were compared.

At the apical level of the LV, mean BMDs and LCCs from the method with the SCT were more consistent than those from the method without the SCT, and improvements in BMDs and LCCs by the use of the SCT and the bi-directional sequential segmentation increased dramatically as the frame number approached the middle of cardiac cycle (frame 10), as shown in Figure 13. These results were obtained because the initial seed contours for each frame, which were tracked and placed closer to the desired boundary by the SCT, significantly reduced the segmentation errors in each frame and prevented their propagation. The intra-observer variability by slightly different initial seed contours for the first frame of a sequence was also lower in most cardiac frames, as shown in Table 7. Similar to the experiments of individual frame segmentation, only BMDs were measured for the RV. At the apical level of the RV, the overall magnitudes of BMDs and improvements in BMDs were lower than those for the LV, because of the presence of the papillary muscles and the thinner myocardial wall. The thinner myocardial wall produces more errors in boundary pixel selection and displacement before the actual SCT, and tracking the boundary pixels outside the myocardial wall can place an initial seed contour for the subsequent frame at a location far away from the desired boundary. These facts resulted in lower improvements in BMDs and virtually no

improvement in the intra-observer variability of segmentation. Figure 14 and Table 8 show the results of sequential frame segmentation of the endocardial boundaries at the apical level of the RV.

At the mid-LV, changes in positions and shapes of the endocardial boundaries between the subsequent frames were less than at the apical level. Thus, the overall performance improvement by the use of the SCT was lower than those at the apical level, as shown in Figure 15. However, improvements, which increased toward the middle of the cardiac cycle, were still obtained in both BMDs and LCCs, except for the frame 12, where the flow-related signal loss was large. The performance degradation by the signal loss in the magnitude image can be compensated by the combined use of the OGF and the SCT as described in section 3.7.3. The intra-observer variability of segmentation was also lowered by the use of the SCT, as shown in Table 9. Experimental results for the mid-RV were the similar to those obtained for the apical level of the RV, as shown in Figure 16 and Table 10. However, the magnitudes of BMDs and improvements in BMDs were generally higher than those at the apical level because of the reduced effects of the papillary muscles.

The velocity wrap-around problem also affected the performance of sequential frame segmentation at the basal level of the LV as it did in the individual frame segmentation. Improvements in BMDs and LCC at frame 2 and 4 were relatively low, and improvement in BMD at frame 10 was even negative, as shown in Figure 17 b) and d). This is because small errors in the position of the segmented boundary and the boundary pixel selection process produce large positional errors in the initial seed contour for the subsequent frame after applying the SCT. The intra-observer variability was also affected by this problem, as shown in Table 11. For the RV, the combined effects of velocity wrap-around and the thinner myocardial wall resulted in more modest improvements in BMDs and virtually no improvement in the intra-observer variability, as shown in Figure 18 and Table 12.

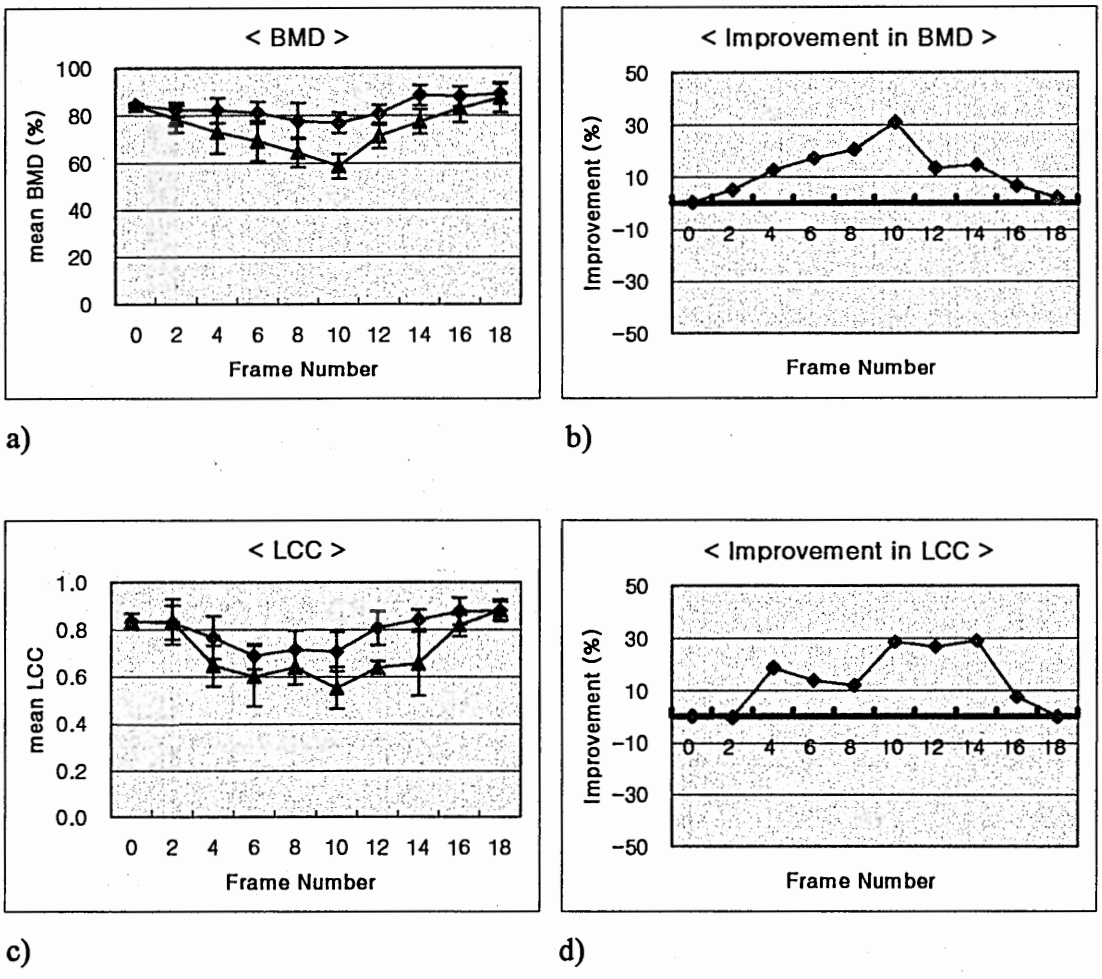

Figure 13. Performance graphs of sequential frame segmentation at the apical level of the LV. Mean boundary matching descriptor (BMD) values and mean linear correlation coefficient (LCC) values of ten selected frames are given in a) and c) respectively. Improvements in mean BMDs and mean LCCs are given in b) and d) respectively. Blue in a) and c) indicates the results with the OGF, and magenta in a) and c) indicates the results without the OGF. Error bars in a) and c) represent the standard deviations.

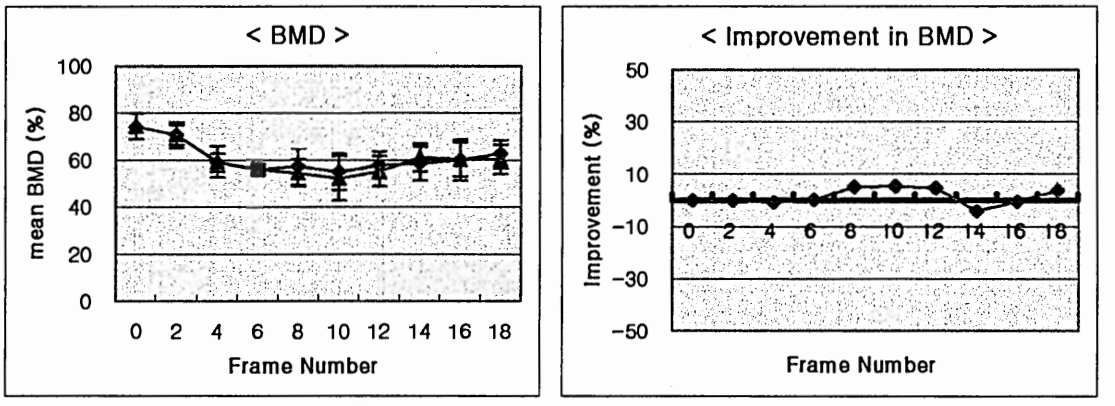

a) b)

Figure 14. Performance graphs of individual frame segmentation at the apical level of the RV. Mean boundary matching descriptor (BMD) values of ten selected frames are given in a). Improvements in mean BMDs are given in b). Blue in a) indicates the results with the OGF, and magenta in a) indicates the results without the OGF. Error bars in a) represent the standard deviations.

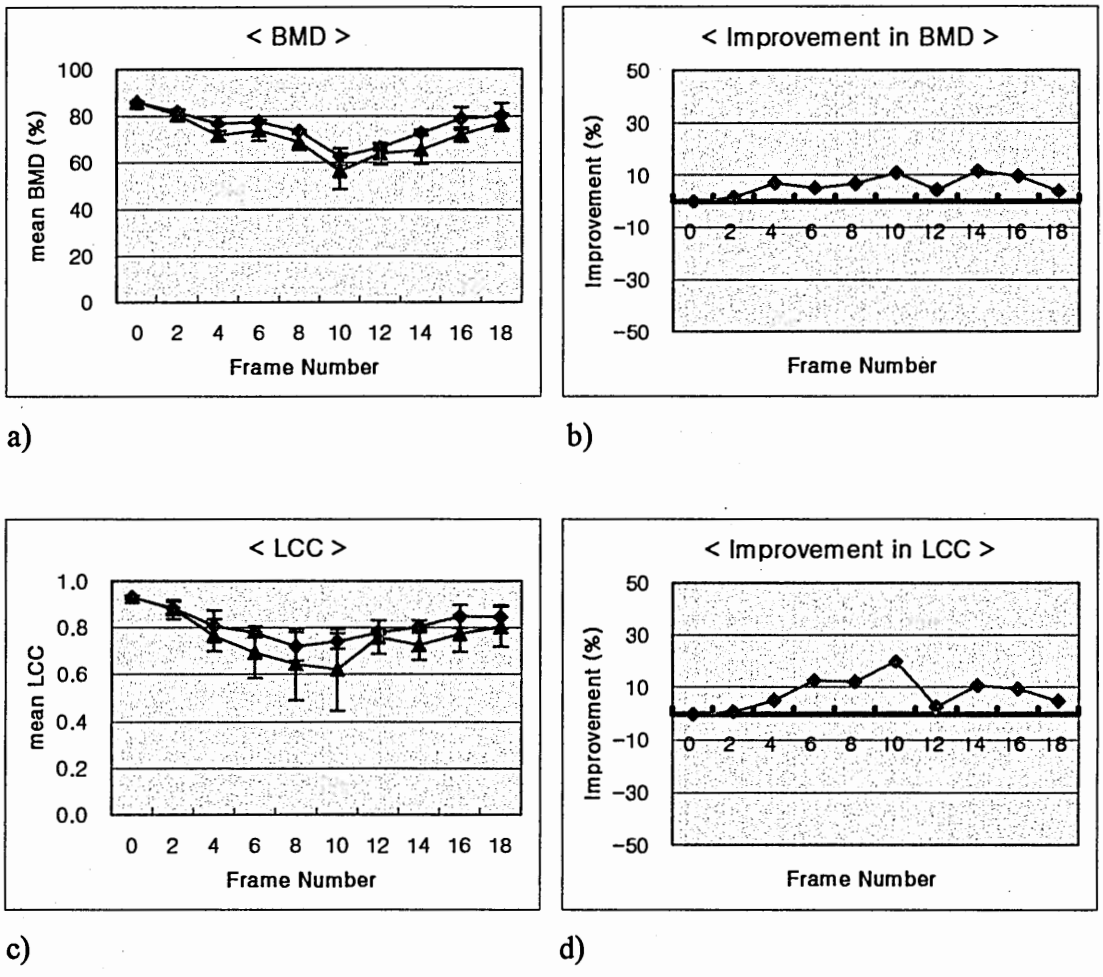

Figure 15. Performance graphs of sequential frame segmentation at the mid-ventricular level of the LV. Mean boundary matching descriptor (BMD) values and mean linear correlation coefficient (LCC) values of ten selected frames are given in a) and c) respectively. Improvements in mean BMDs and mean LCCs are given in b) and d) respectively. Blue in a) and c) indicates the results with the OGF, and magenta in a) and c) indicates the results without the OGF. Error bars in a) and c) represent the standard deviations.

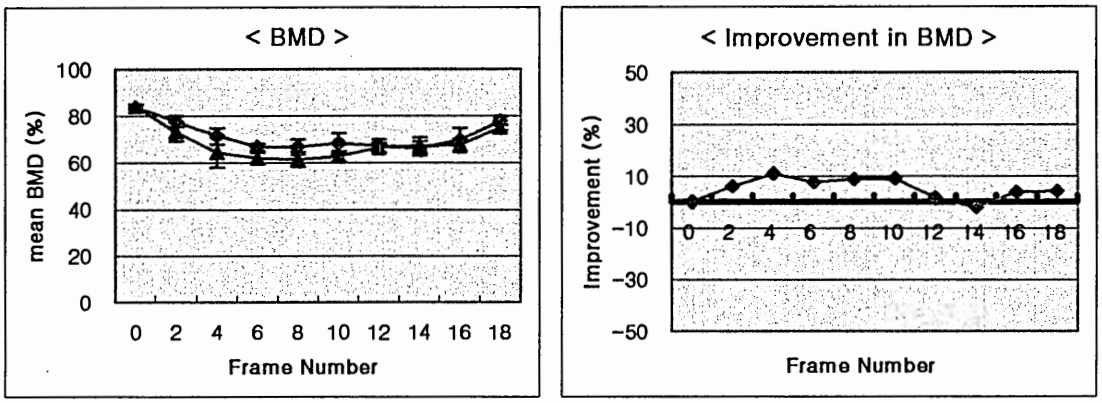

a) b)

Figure 16. Performance graphs of individual frame segmentation at the mid-ventricular level of the RV. Mean boundary matching descriptor (BMD) values of ten selected frames are given in a). Improvements in mean BMDs are given in b). Blue in a) indicates the results with the OGF, and magenta in a) indicates the results without the OGF. Error bars in a) represent the standard deviations.

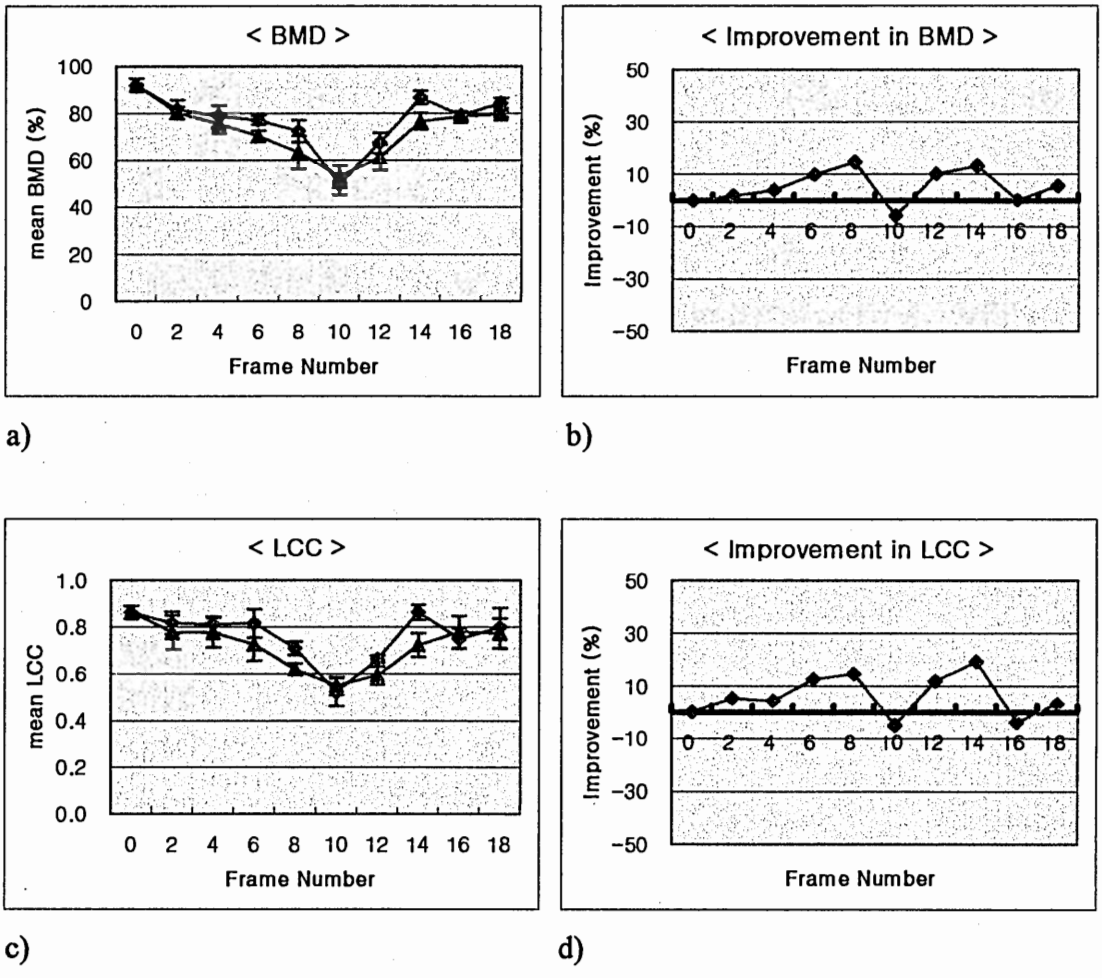

Figure 17. Performance graphs of sequential frame segmentation at the basal level of the LV. Mean boundary matching descriptor (BMD) values and mean linear correlation coefficient (LCC) values of ten selected frames are given in a) and c) respectively. Improvements in mean BMDs and mean LCCs are given in b) and d) respectively. Blue in a) and c) indicates the results with the OGF, and magenta in a) and c) indicates the results without the OGF. Error bars in a) and c) represent the standard deviations.

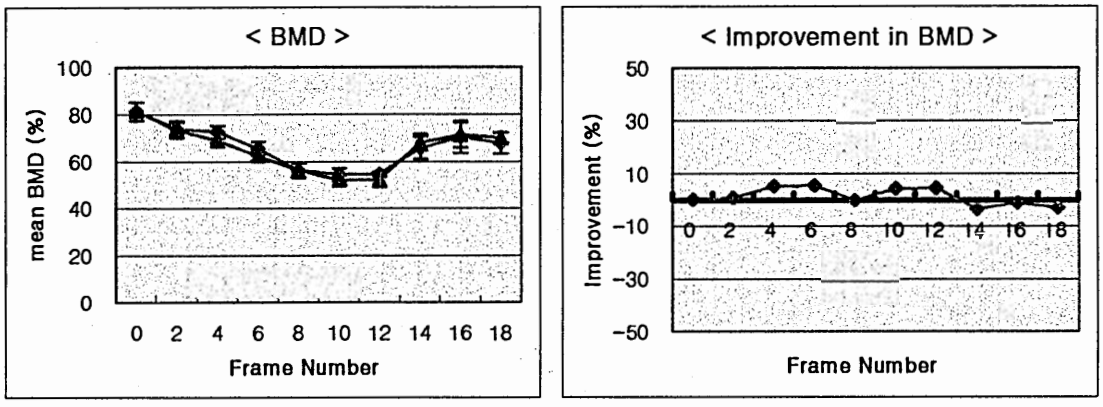

a) b)

Figure 18. Performance graphs of individual frame segmentation at the basal level of the RV. Mean boundary matching descriptor (BMD) values of ten selected frames are given in a). Improvements in mean BMDs are given in b). Blue in a) indicates the results with the OGF, and magenta in a) indicates the results without the OGF. Error bars in a) represent the standard deviations.

Table 7. Results of sequential frame segmentation at the apical level of the LV. Endocardial boundaries in twenty cardiac frames were sequentially segmented five times by the same observer. The boundary matching descriptors (BMD) and linear correlation coefficients (LCC) of ten selected frames presented here are mean ± standard deviation.

	With SCT		Without SCT	
Frame Number	BMD (%)	LCC	BMD (%)	LCC
0	84.38±0.72	0.834±0.034	84.20±0.74	0.834±0.034
2	82.30±3.19	0.830±0.071	78.44±5.63	0.834±0.097
4	82.06±5.28	0.766±0.093	72.84±8.67	0.646±0.086
6	81.10±4.71	0.686±0.055	69.16±8.49	0.602±0.130
8	77.52±7.63	0.714±0.080	64.26±6.15	0.638±0.071
10	76.66±4.22	0.706±0.084	58.62±5.35	0.550±0.090
12	80.68±3.81	0.808±0.075	71.16±4.80	0.638±0.026
14	88.62±4.37	0.844±0.042	77.34±5.27	0.654±0.135
16	88.00±4.30	0.878±0.058	82.72±5.67	0.818±0.048
18	89.12±4.23	0.880±0.037	87.40±6.47	0.882±0.045

Table 8. Results of sequential frame segmentation at the apical level of the RV. Endocardial boundaries in twenty cardiac frames were sequentially segmented five times by the same observer. The boundary matching descriptors (BMD) of ten selected frames presented here are mean ± standard deviation.

	With SCT	Without SCT
Frame Number	BMD (%)	BMD (%)
0	74.26±5.33	74.26±5.33
2	70.62±5.40	70.74±4.24
4	58.78±3.67	59.22±6.84
6	55.94±1.31	55.92±2.34
8	57.14±7.77	54.40±5.71
10	54.92±7.70	52.10±9.36
12	57.78±5.93	55.16±6.37
14	58.48±7.27	61.08±5.89
16	59.86±8.74	60.22±7.26
18	62.48±5.97	60.22±6.18

Table 9. Results of sequential frame segmentation at the mid-ventricle level of the LV. Endocardial boundaries in twenty cardiac frames were sequentially segmented five times by the same observer. The boundary matching descriptors (BMD) and linear correlation coefficients (LCC) of ten selected frames presented here are mean± standard deviation.

	With SCT		Without SCT	
Frame Number	BMD (%)	LCC	BMD (%)	LCC
0	85.80±0.44	0.930±0.010	85.80±0.44	0.930±0.010
2	81.77±1.33	0.883±0.025	80.60±2.17	0.877±0.040
4	76.73±3.15	0.807±0.065	71.73±2.27	0.767±0.068
6	77.63±0.29	0.780±0.020	73.90±4.44	0.693±0.110
8	73.57±0.65	0.720±0.061	68.93±3.54	0.643±0.153
10	62.47±3.70	0.743±0.032	56.40±7.69	0.620±0.173
12	66.50±1.47	0.780±0.010	63.70±4.57	0.760±0.070
14	73.00±1.31	0.803±0.025	65.43±6.07	0.727±0.064
16	79.00±4.70	0.847±0.049	72.03±3.21	0.773±0.076
18	80.10±5.37	0.843±0.049	77.17±3.61	0.803±0.086

Table 10. Results of sequential frame segmentation at the mid-ventricle level of the RV. Endocardial boundaries in twenty cardiac frames were sequentially segmented five times by the same observer. The boundary matching descriptors (BMD) of ten selected frames presented here are mean ± standard deviation.

	With SCT	Without SCT
Frame Number	BMD (%)	BMD (%)
0	84.17±1.29	84.17±1.29
2	77.70±2.29	73.27±4.10
4	71.50±3.60	64.40±6.37
6	66.67±1.55	61.87±2.55
8	66.77±3.16	61.40±3.22
10	68.27±4.24	62.63±2.24
12	67.37±2.65	66.47±2.00
14	66.10±3.06	67.37±3.37
16	69.80±5.20	67.43±2.59
18	78.03±1.85	75.07±1.15

Table 11. Results of sequential frame segmentation at the basal level of the LV. Endocardial boundaries in twenty cardiac frames were sequentially segmented five times by the same observer. The boundary matching descriptors (BMD) and linear correlation coefficients (LCC) of ten selected frames presented here are mean± standard deviation.

	With SCT		Without SCT	
Frame Number	BMD (%)	LCC	BMD (%)	LCC
0	91.83±2.91	0.863±0.029	91.83±2.91	0.863±0.029
2	81.60±4.01	0.817±0.049	80.17±2.32	0.777±0.075
4	78.57±4.51	0.810±0.036	75.53±4.17	0.777±0.065
6	77.07±1.78	0.817±0.060	70.13±2.45	0.727±0.070
8	72.27±4.68	0.710±0.030	63.00±7.19	0.620±0.026
10	49.63±4.28	0.520±0.060	52.83±4.54	0.547±0.038
12	67.27±4.35	0.663±0.015	61.03±5.58	0.593±0.040
14	86.67±2.75	0.863±0.032	76.63±3.44	0.723±0.051
16	78.77±1.51	0.750±0.044	78.73±1.69	0.780±0.069
18	84.07±2.14	0.797±0.087	79.60±1.21	0.773±0.065

Table 12. Results of sequential frame segmentation at the basal level of the RV. Endocardial boundaries in twenty cardiac frames were sequentially segmented five times by the same observer. The boundary matching descriptors (BMD) of ten selected frames presented here are mean ± standard deviation.

	With SCT	Without SCT
Frame Number	BMD (%)	BMD (%)
0	81.37±3.95	81.37±3.95
2	73.93±2.51	73.43±3.56
4	72.47±2.68	68.87±0.91
6	65.57±2.74	62.17±2.01
8	56.13±2.98	56.20±3.05
10	54.27±2.71	52.10±2.10
12	54.53±0.86	52.23±3.10
14	65.70±4.68	68.17±3.41
16	70.37±6.76	71.23±5.34
18	67.77±4.50	69.90±2.07

3.8 Discussions and Conclusions

The active contour models have been quite successful in segmentation of the myocardium boundaries. However, most of them still suffer from problems such as flow-related signal loss, the presence of papillary muscles, and poor visualization of the endocardium. In addition, large changes in positions and shapes of the myocardial boundaries between the subsequent time frames may cause the propagation of errors in sequential frame segmentation.

A new velocity-aided cardiac segmentation method, which is based on a modified active contour model and phase contrast MRI, has been developed to improve the accuracy of MRI-based cardiac segmentation. Unlike other segmentation methods based on active contour models, the velocity images from phase contrast MRI, together with the magnitude images, were used for segmentation of the myocardial boundaries. Using this additional information, the tensor-based orientation gradient force was derived and incorporated into the generalized active contour model to improve the accuracy of segmentation of the myocardial boundaries, especially the endocardial boundary. Furthermore, the initial seed contour tracking algorithm was developed to improve the accuracy of automatic sequential frame segmentation throughout the entire cardiac cycle.

The performance of the proposed velocity-aided cardiac segmentation method has been assessed by experimentations on a phase contrast MRI data set of a normal human volunteer. Experimental results of the individual frame segmentation showed that improvements in the accuracy and reproducibility of segmentation of the endocardial boundary by the use of the OGF were obtained mostly around the lower level of the ventricles and end systole. However, improvements were generally negligible around the upper level of the ventricles and end diastole, and the velocity wrap-around problem and blood turbulence around the basal level of the ventricles even degraded the performance of boundary segmentation. Experimental results of the sequential frame segmentation showed that the propagation of errors caused by improper positioning of initial seed contours was significantly reduced by the use of the SCT. Improvements in the accuracy and reproducibility of segmentation of the endocardial boundary were higher in the LV than the RV and increased as the frame number approached the middle of cardiac cycle by the use of the SCT and the bi-directional sequential segmentation. The velocity wrap-around problem at the basal level of both ventricles and the thinner myocardial wall of the RV degraded the performance of the SCT and sequential frame segmentation. In general, improvements in the sequential frame segmentation were higher than those in the

individual frame segmentation. Visual comparisons of the segmented endocardial boundaries of selected frames in the LV are presented in Appendix A.

Because problems of registration and flow-artifact of phase contrast MRI data set can degrade the performance of the proposed segmentation method, appropriate pre-processing steps are needed to reduce potential sources of segmentation errors from these problems. Although a simple registration method based on a block matching approach was applied for the acquired data set in this thesis, a better method for registration and a method for reducing flow-artifact are highly desirable. Therefore, future work should include the development of these methods. Because of the experimentations with the limited data set of a normal human subject, the results might be easily biased by a certain experimental setting. Future work should also include experimentations with more data sets of various human subjects.

Part II

Cardiac Motion-Tracking

CHAPTER 4

Background

In this chapter, MRI-based cardiac motion-tracking methods that have been used previously to derive the dynamic characteristics of the myocardium are described. They can be classified into three main categories, tagged MRI-based methods, phase contrast MRI-based methods, and computer vision-based methods, depending on the techniques used to obtain correlation of the positions of myocardial tissue points between images taken at subsequent time frames.

4.1 Tagged MRI-based Cardiac Motion-Tracking

MR tagging is a technique that can be used to label and track specific regions of the myocardium during contraction. MR tagging technique produces dark lines or stripes in the myocardium as multiple and noninvasive markers. Thus, the motion of the

myocardium within a certain relaxation time can be tracked without using invasive markers, such as implanted sutures, because lines or stripes move with myocardial tissue. It originated from "time-of-flight method" that measured blood flow by locally saturated magnetization of blood and detected the passage of this tagged blood stream [42]. Zerhouni *et al.* [4] proposed the first MR tagging technique for the analysis of the myocardial motion within the plane of the image by using selective excitation to produce a pattern of lines (star-bursts) of altered magnetization. Axel *et al.* [5, 6] and Bolster *et al.* [7] further improved the tagging technique to have grid-like shape so that many markers could be tracked.

Among these techniques, Axel's technique based on the spatial modulation of magnetization (SPAMM) has been extensively used for the analysis of the myocardial motion and is briefly described here. SPAMM produces a dark tagging grid by spatially modulating the degree of magnetization prior to imaging. It uses a sequence of two RF pulses separated by a magnetic-field-gradient pulse. Starting from a condition of uniform longitudinal magnetization, a RF pulse (a 90° flip angle) turns this magnetization into transverse magnetization with the same initial phase. Then, a magnetic-field gradient is applied across the sample, causing the transverse magnetization to dephase linearly

across the sample in the direction of the gradient. This corresponds to a sinusoidal modulation of the x and y components of the transverse magnetization along the direction of the applied gradient. Then, applying the second RF pulse with the same flip angle as the first produces a sinusoidal modulation of the longitudinal magnetization. The resulting image shows periodic stripes due to this modulation. Applying another sequence of two RF pulses with the field gradient orthogonal to the first field gradient produces a tagging grid, as shown in Figure 19.

As described, SPAMM provides somewhat sparse but sufficient number of noninvasive markers within the imaging plane to track the motion of the myocardium. It yields the two (x and y) components of the motion parallel to the image plane, so the two-dimensional (in-plane) motion of the myocardium can be directly visualized and tracked [43, 44, 45, 46, 47, 48, 49]. However, because the motion and deformation of the myocardium are typically described by the strain that is a function of the derivatives of the displacement field, the interpolation process is needed to obtain a dense displacement field. In addition, because the current MR imaging techniques can provide only the image slices instead of true volumetric data, the three-dimensional motion of the myocardium can not be directly visualized and tracked as the two-dimensional case. For example,

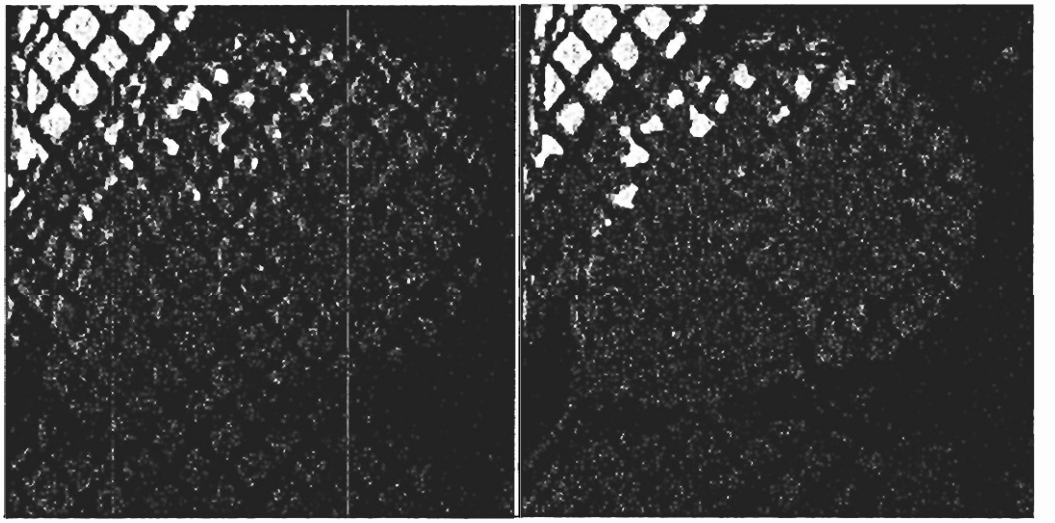

Figure 19. An example of SPAMM images. Image on the left is at end-diastole, and image on the right is at end-systole.

given that every imaging plane is spatially fixed, the out-of-plane (through-plane) motion of the myocardium cannot be captured by tagged data points on the image plane: i.e., the subsequent motion of tissue points imaged at frame 0 are not generally known. However, tagged data points imaged at subsequent frames ($t \geq 1$) provide one-dimensional displacement information because their projections at frame 0 onto the imaging planes are known. Figure 20 shows the relationship between imaged and actual tissue displacement. Point P on the tagging plane is initially imaged as P' and finally as P''. P and P'' are the same tissue point, a component of whose motion is estimated by the tagging

approach to have the displacement of P' to P''. As stated previously, the motion of the tissue point initially at P' is generally not imaged at subsequent frames due to the out-of-plane motion. Therefore, a method for combining a series of sparse one-dimensional displacement information into a dense three-dimensional displacement field is needed to fully characterize the three-dimensional motion of the myocardium.

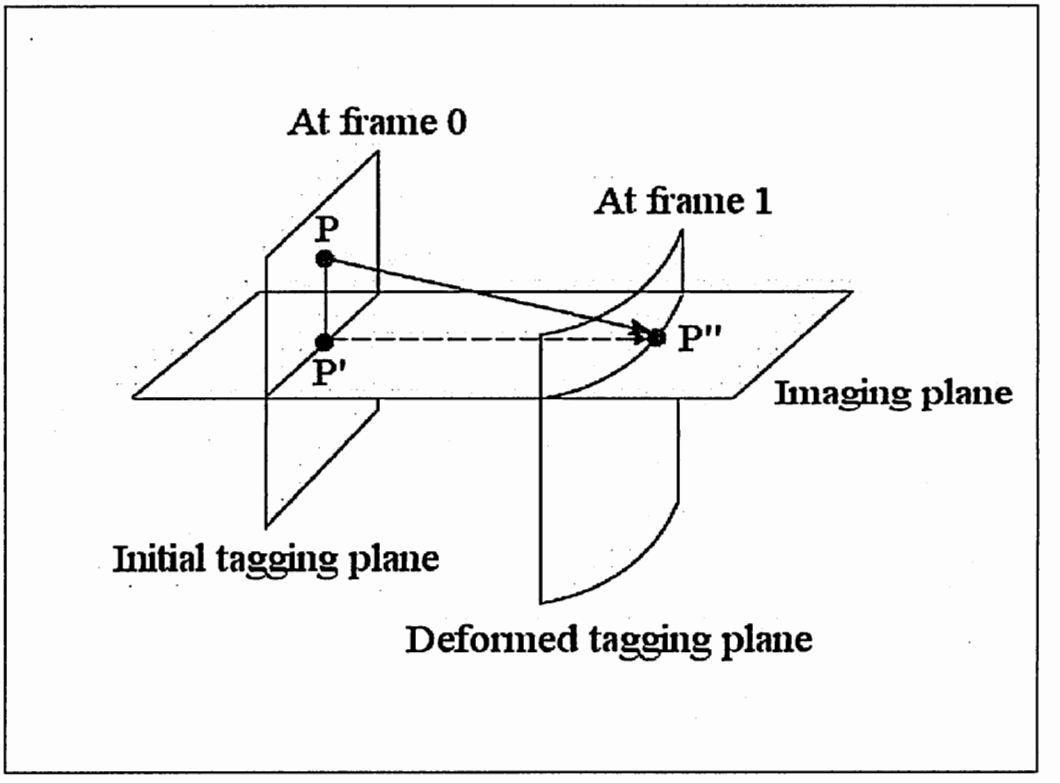

Figure 20. Relationship between imaged and actual tissue displacement.

Model-based cardiac motion-tracking methods have been widely used to reconstruct the three-dimensional displacement field from the two-dimensional image sequences from tagged MRI. Young *et al.* [13, 14, 50, 51, 52, 53] proposed a finite-element model-based approach to reconstruct the three-dimensional motion of the myocardium. In their method, a finite-element model is first constructed based on techniques described by Nielsen *et al.* [54]. This model is then used to reconstruct the three-dimensional displacement field from the one-dimensional displacement information obtained from short- and long-axis tagged MRI slices. The actual reconstruction technique is based on model-fitting procedures, which are called "reconstruction fit" and "deformation fit." Young *et al.* [55, 56] recently developed a similar method for tracking the three-dimensional motion of the myocardium based on a "model tag" and applied this method to the analysis of the motion of the RV. This method does not require "reconstruction fit," and thus can be analyzed faster. Park *et al.* [15, 57, 58, 59, 60] used a volumetric physics-based deformable model and Lagrangian dynamics in the analysis of the three-dimensional motion of the myocardium. They fitted a deformable model to tagged MRI data set of the LV to reconstruct the three-dimensional displacement field and extract the motion parameters. Their deformable model is based on the parameter

functions that can capture regional shape variations of the LV, such as bending, twisting, and contraction. O'Dell *et al.* [61, 62] proposed a three-dimensional motion reconstruction method from planar tagged MR images, where three orthogonal sets of one-dimensional displacement fields from a stack of two-dimensional short- and long-axis slices of the LV were used to fit an analytical series expression in a polar spheroidal coordinate system. Kerwin *at al.* [63] and Ozturk *at al.* [64] proposed spline-based methods for reconstructing the three-dimensional motion of the myocardium from tagged MR images. Denny *at al.* [65] also proposed a method for estimating a dense displacement field from sparse displacement field based on a stochastic model. In general, these model-based cardiac motion-tracking methods extract a series of one-dimensional displacement information from orthogonal tagging planes and then fit a model to the displacements of tagging stripe intersection points (or tagging stripes) to reconstruct the three-dimensional displacement field.

Tagged MRI-based cardiac motion-tracking methods have been quite successful because of the low sensitivity to artifacts, relatively high temporal resolution, and direct visualization of myocardial motion, but currently have the several limitations. First, tracking the entire cardiac cycle often suffers from the inherent tag fading from T_1

recovery: i.e., the motion of the myocardium only during the contraction phases can be tracked without the tag fading problem. Secondly, multiple data acquisitions, such as acquisitions in both short and long axis, are required to obtain three-dimensional motion information of the myocardium. Thirdly, detection of tagging stripes or tagging stripe intersection points is required in the preprocessing stage. The tag detection step is generally done by semiautomatic segmentation methods [66, 67, 68], but it may cause errors in the motion-tracking stage. Lastly, because of the limited spatial resolution of tagging grids, an appropriate interpolation method based on a specific model-geometry is generally required to obtain a dense displacement field. Thus, the motion-tracking method is often limited to a specific ventricle.

4.2 Phase Contrast MRI-based Cardiac Motion-Tracking

Although phase contrast MRI has been extensively used for measurement of blood flow as described in section 3.2, several researchers have also applied this imaging technique to measurement of the motion of the myocardium. Dijk [69] first suggested the use of MR phase to obtain the myocardial velocity using a spin echo gated MR imaging sequence, and Nayler *et al.* [70] then demonstrated that velocity information could be

encoded into the phase of the MR signal by using rapid gradient echo sequences. More recently, N.J. Pelc *et al.* [8, 71, 72] extended these concepts by incorporating the velocity phase encoding into a conventional Cine-MR sequence and enabled the tracking of the motion of the myocardium throughout the entire cardiac cycle.

The data provided by phase contrast MRI are velocities at a set of fixed points in space, i.e., instantaneous Eulerian velocities. Because velocity measurements at a given image location at different times generally correspond to different myocardial tissue points, deriving the motion and deformation characteristics of the myocardium necessarily involves tracking the motion of myocardial tissue points. Thus, velocity-based trajectory computation is needed to obtain the tissue velocities and their trajectories. Several tracking methods have been proposed to calculate the trajectories of tissue points by integrating the velocities over time. Constable *et al.* [73] and N.J. Pelc *et al.* [74] proposed tracking methods for the two-dimensional motion of the myocardium using similar velocity integration methods. L.R. Pelc *et al.* [75] compared their methods with directly visualized motion by implanted markers. Lingamneni *et al.* [76] improved N.J. Pelc's method by using motion terms higher than the velocity. These are based on "forward-backward velocity integration."

Forward-backward velocity integration performs two different velocity integrations as follows. Velocity integration in the forward direction is first performed by a recursive summation over the velocity as described in section 3.6:

$$f_{k+1} = f_k + v(f_k, t_k)\Delta t \tag{50}$$

where f_{k+1} is the position of a tracked tissue point at time t_{k+1}, k is the current frame number, $v(f_k, t_k)$ denotes the velocity at the position of tissue point at time t_k, and Δt is the temporal resolution (phase delay) of a phase contrast MR data set. This simple integration method assumes that the velocity is $v(f_k, t_k)$ for the entire interval t_k to t_{k+1}, and then suddenly becomes $v(f_{k+1}, t_{k+1})$. Therefore, if it is assumed that the velocity varies linearly during the time interval (from t_k to t_{k+1}), then a refined trajectory of tissue motion can be obtained by:

$$f_{k+1} = f_k + \frac{1}{2}[v(f_k, t_k) + v(f_{k+1}, t_{k+1})]\Delta t \tag{51}$$

These forward directional velocity integration methods estimate the tissue location in the next time frame from the location in the current time frame. However, because periodic motion of the myocardium and retrospective gating ensure that a point identified in the first frame returns to its starting position in the end of each cardiac cycle, velocity integration in backward direction can also be performed to obtain a trajectory of tissue

motion. Let b_k be the trajectory resulting from backward directional velocity integration. Then, the equations of the backward directional velocity integration are

$$b_{k-1} = b_k - v(b_k, t_k)\Delta t \tag{52}$$

$$b_{k-1} = b_k - \frac{1}{2}[v(b_k, t_k) + v(b_{k-1}, t_{k-1})]\Delta t \tag{53}$$

Then, more reliable trajectory of tissue motion can be obtained by combining the trajectories from forward and backward integrations. Let this combined trajectory r_k be a linear combination of the forward and backward trajectories, with the relative weighting on the forward trajectory, w_k, being dependent on the time frame:

$$r_k = w_f f_k + w_b b_k \tag{54}$$

where the weighting coefficient w can be selected on the basis of various constraints. Examples of the appropriate weighting coefficients are $w_f = 1 - t/T$ and $w_b = t/T$ that minimize the velocity offset caused by eddy current-induced fields, where T is the cardiac cycle. Because forward/backward trajectory error increases with increasing/decreasing frame numbers, these intuitive weighting coefficients effectively minimize the errors of the combined trajectory.

Data degradation in the acquisition process resulting from sources such as eddy currents and the interpolation procedure used in cine data reconstruction sometime

presents challenges to phase contrast MRI-based cardiac motion analysis. To reduce this degradation and improve the tracking accuracy of the motion trajectory, Zhu *et al.* [77] proposed a tracking method based on the frequency domain integration technique. Rather than using polynomial models and the time domain velocity integration, this method uses a Fourier model that takes advantage of the periodicity of the measured data and any depicted motion. Because the motion depicted by the cine data is periodic, the algorithm models a trajectory composed of Fourier harmonics and integrates the velocity data in the frequency domain. Later, Drangova *et al.* [78] compared Zhu's method with the forward-backward integration method, and a better in-plane tracking accuracy was obtained in the frequency domain integration technique. However, a problem of the trajectory underestimation occurred when there was the out-of-plane motion of the myocardium.

Although the velocity integration methods described so far produce reliable in-plane motion trajectories of the myocardium, these methods clearly can introduce errors not only in the out-of-plane direction, but also in the in-plane directions. This is because these methods use only a single slice from the phase contrast MRI and assume that there is no motion in the out-of-plane direction. To cope with this problem, Zhu *et al.* [79] used multiple two-dimensional slices from phase contrast MRI to track the three-dimensional

motion of the myocardium. In their method, a linear spatial modeling technique is used because phase contrast MRI has relatively low out-of-plane resolution compared with the in-plane resolution. Zhu *et al.* [80] also proposed a spatial and temporal modeling method using a finite element-based deformable model and Fourier tracking.

Phase contrast MRI-based cardiac motion-tracking methods have several advantages over tagged MRI-based methods. First, because of higher spatial resolution of trackable markers, pointwise motion-tracking of the myocardium can be achieved. Secondly, segmentation of markers, such as tag intersection points, is not needed. However, phase contrast MRI-based methods are sensitive to velocity artifacts and do not have the capability of direct visualization of the motion of the myocardium. They also suffer from the relatively low out-of-plane resolution of velocity images. Furthermore, because velocity estimation near the myocardial boundaries is often noisy, the tracking accuracy near the myocardial boundaries can be degraded.

4.3 Computer Vision-based Cardiac Motion-Tracking

Several computer vision-based methods, which try to obtain correlation of positions of myocardial tissue points between subsequent time frames without the use of either tagged MRI or phase contrast MRI, have been proposed to track the motion of the myocardium. Song *at al.* [81] used three-dimensional cine-CT images and the optical flow algorithm, which is based on the assumption that a pixel in an image is consistent in its intensity level from one frame to the next. Amini *et al.* [82] used a shape feature-based method to obtain displacement estimates. Shi *at al.* [83, 84] proposed a pointwise tracking method based on the surface curvature of the epicardium and also combined a curvature-based displacement estimation method with phase contrast MRI [85]. Papademetris *at al.* [86] also proposed a shape feature-based method using a physical model and ultrasound images.

In general, computer vision-based cardiac motion-tracking methods are mostly independent of imaging modality types: i.e., MRI, CT, or ultrasound can be used. However, most of them are very dependent on accurate ventricular boundary (or surface) segmentation that are still neither easy to achieve or fully automated. Furthermore, their trackable region tends to be limited to a certain region of the ventricle.

CHAPTER 5

Elastically Deformable Model-based Cardiac Motion-Tracking

5.1 Introduction

As described in section 4.2, phase contrast MRI has been used for cardiac motion-tracking with the several advantages over tagged MRI. However, because the data acquisition time of phase contrast MRI usually prohibits the use of true volumetric data in routine clinical practice, phase contrast MRI generally produces only multiple two-dimensional image slices with relatively low out-of-plane resolution. A linear or higher order spatial modeling technique can be used to estimate the velocity values within (or between) the imaged slices to compensate for the effects of this relatively low out-of-plane resolution. However, because of the complex shape and motion of the myocardium, simple polynomial model-based techniques may produce errors in the estimated velocity

values, and consequently they may degrade the accuracy of tracking not only the out-of-plane motion but also the in-plane motion of the myocardium. Therefore, in order to track the three-dimensional motion of the myocardium more accurately, the effects of the relatively low out-of-plane resolution of phase contrast MRI should be effectively compensated for or minimized.

In this chapter, a new elastically deformable model-based cardiac motion-tracking method is introduced to estimate the three-dimensional motion and deformation of the myocardium. The method is designed mainly to address the problem of the relatively low out-of-plane resolution of phase contrast MRI and transforms the cardiac motion-tracking problem into an energy minimization. In section 5.2, the basic concept of elastic deformation and the elastically deformable model, which will be used to recover the three-dimensional motion and deformation of the myocardium, is reviewed. In section 5.3, a cardiac motion-tracking method using elastic deformation estimation (EDE) is introduced. In section 5.4, techniques for constructing a geometrical representation of the LV from phase contrast MRI data set is presented. In section 5.5, the overall procedure of the motion-tracking is described. Experimental results are presented in section 5.6, followed by the discussions and conclusions in section 5.7.

5.2 Elastically Deformable Model

The complete modeling of the physical properties and mechanical behavior of the myocardium is extremely difficult and has been an ambitious goal because the myocardium is non-linear, anisotropic, and an active material. Rather, simplified modeling techniques, which retain some of the important properties of the myocardium, have been developed to seek a trade off between precise modeling and computational efficiency. In this section, an elastically deformable model, which is used to recover the three-dimensional motion and deformation of the myocardium, is described. This model is often considered the approximate continuum model because it adheres less strictly to the laws of physics than the sophisticated continuum mechanics-based models. However, it is still physically plausible and computationally efficient.

Deformation is called elastic when an object recovers its undeformed reference configuration (shape) as soon as all externally applied forces are removed. The elastic force is the force that recovers the deformed object to its reference configuration and can be characterized by the deformation potential that associates an energy with the deformation of an object. The deformation potential energy should have the following properties: the energy is zero in the reference configuration of an object, the energy

increases as the deformation of an object from its reference configuration increases, and the energy is invariant to rigid motion of an object. The differential geometric-based shape description can be used to define the deformation potential energy of a three-dimensional object that has the above properties.

Two objects (solids) in three-dimensional space have the same instantaneous shape if their metric tensors are identical at a particular time [87, 88]. Let the metric tensor be G, and defined by a 3 by 3 matrix with entries:

$$G_{ij}(\mathbf{p}(\mathrm{u},t)) = \frac{\partial \mathbf{p}}{\partial u_i}\frac{\partial \mathbf{p}}{\partial u_j} \tag{55}$$

where u_i is the ith element of three Cartesian coordinates, and $\mathbf{p}$ is a parametric representation of the position of a constituent point of an object defined by $\mathbf{p}(\mathrm{u}, t) = [p_1(\mathrm{u}, t), p_2(\mathrm{u}, t), p_3(\mathrm{u}, t)]^{\mathrm{T}}$, where $\mathrm{u} = (u_1, u_2, u_3)$ at time t in a domain $\Omega = 0 \le u_1, u_2, u_3 \le 1$. This metric tensor describes the shape of an object defined by Euclidean distances and angles between nearby points in three-dimensional space. The off-diagonal elements quantify angle deviations and the diagonal elements quantify distance deviations. These distances and angles change as an object deforms, and the metric tensor is invariant to rigid motions such as rotation and translation [89]. Therefore, the metric tensor uniquely describes the instantaneous shape of an object by the stretching and shearing tensor

components between nearby data points in three-dimensional space. Using this shape measure, the deformation potential energy, which describes the elastic deformation of an object, can be defined as:

$$E_{deformation}(\mathbf{p}) = \int_0^1 \int_0^1 \int_0^1 \sum_{i,j=1}^{3} \alpha_{ij}(\mathrm{u})(G_{ij}(\mathbf{p}) - G_{ij}^0(\mathbf{p}))^2 du_1 du_2 du_3 \tag{56}$$

where G is the metric tensor of the deformed state, G^0 is the metric tensor of the reference (undeformed) state, and $\alpha_{ij}(\mathrm{u})$ is a weighting coefficient determining the influence of each tensor component: the resistance to stretching along u_1, u_2, and u_3, as well as shearing across planes perpendicular to these axes.

Now, by using the definition of the elastic deformation of an object, the system of a dynamically deformable model, which unifies the description of shape and motion of a three-dimensional object, can be constructed. Because dynamically deformable model is described completely by the positions $\mathbf{p}(\mathrm{u}, t)$, velocities $\partial \mathbf{p} / \partial t$, and accelerations $\partial^2 \mathbf{p} / \partial t^2$ of its mass elements as functions of u and t, Lagrange's equations of motion for $\mathbf{p}$ is expressed as:

$$\mu \frac{\partial^2 \mathbf{p}}{\partial t^2} + \gamma \frac{\partial \mathbf{p}}{\partial t} + \delta_{\mathbf{p}} E_{deformation}(\mathbf{p}) = \mathbf{f} \tag{57}$$

where $\mathbf{f}(\mathrm{u}, t)$ is the net externally applied force, $\mu(\mathrm{u})$ is a mass density, $\gamma(\mathrm{u})$ is a damping density, and $\delta_{\mathbf{p}} E_{deformation}(\mathbf{p})$ is the internal elastic force that resists deformation. By

numerically solving the above partial differential equation with appropriate initial conditions, the system can evolve to equilibrium and exhibit intuitively meaningful physical behaviors. An example of the elastic behavior of the above elastically deformable model is shown in Figure 21.

5.3 Motion-Tracking by Elastic Deformation Estimation

In this section, a cardiac motion-tracking method by elastic deformation estimation is introduced to recover the three-dimensional motion of the myocardium from phase contrast MRI data set. By first formulating the simplified potential energy of elastic deformation of the myocardium and then constructing a system of a dynamically deformable model, the cardiac motion-tracking problem is transformed into the energy minimization problem of an elastically deformable model. The elastic property incorporated into the system is used to refine the motion-trajectories calculated by the polynomial-based spatial modeling technique. Finally, a numerical solution procedure of the system is described.

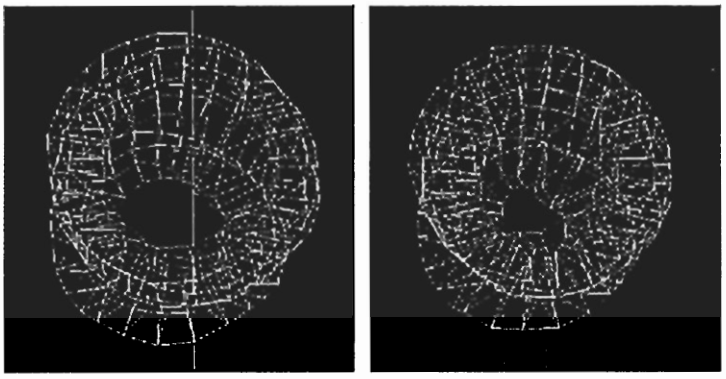

a) b)

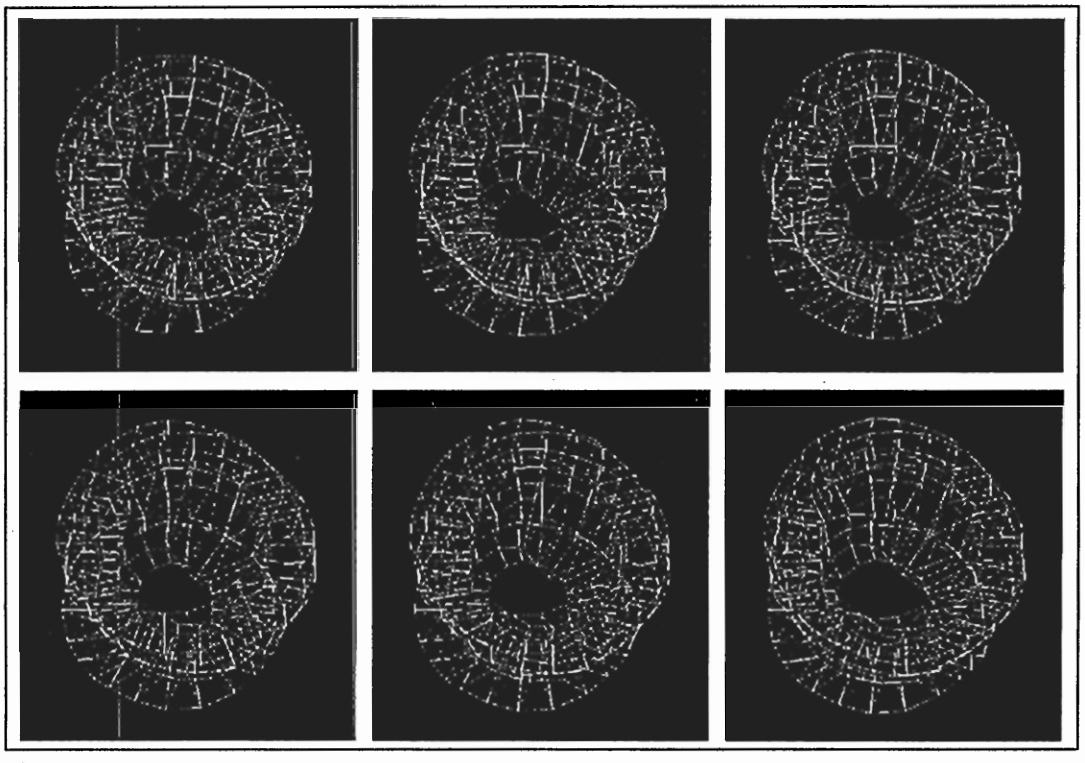

c)

Figure 21. An example of the simulated elastic behavior of the elastically deformable model. a) a reference configuration. b) a deformed configuration. c) a sequence of recovery process back to the reference configuration (left to right and top to bottom) when all externally applied forces are removed.

5.3.1 Potential Energy Formulation

Our cardiac motion-tracking problem is transformed into the energy minimization problem to estimate a set of position vectors **p** of tissue points on the myocardium. The energy minimization of an elastically deformable model of the myocardium balances an internal potential energy derived from an elastic deformation measure of the myocardium and an external potential energy derived from externally applied forces. Its mathematical formulation draws from the optimal approximation theory. The estimated positions of tracked tissue points on the myocardium are expressed as the positions that minimize the total potential energy defined as:

$$E_{total}(\mathbf{p}) = E_{internal}(\mathbf{p}) + E_{external}(\mathbf{p}) \tag{58}$$

where $E_{internal}(\mathbf{p})$ is an internal deformation potential energy and $E_{external}(\mathbf{p})$ is an external potential energy.

To simplify the problem, an assumption has been made: the myocardium is linearly elastic (Hookean's elastic) and isotropic material. Even though the myocardium has much more complex material properties (e.g. non-linear, anisotropic, and active properties) and needs a sophisticated continuum mechanics-based formulation to reflect those properties, this assumption can be used to retain the intuitive physical property of

the myocardium yet greatly simplify our cardiac motion-tracking problem. Using this assumption, the internal deformation potential energy $E_{internal}(\mathbf{p})$ is defined by using Equation (56):

$$E_{internal}(\mathbf{p}) = E_{deformation}(\mathbf{p}) = \int_0^1\int_0^1\int_0^1 \sum_{i,j=1}^{3} \alpha_{ij}(\mathrm{u})(G_{ij}(\mathbf{p}) - G_{ij}^0(\mathbf{p}))^2 du_1 du_2 du_3 \qquad (59)$$

where $\alpha_{ij}(\mathrm{u})$ is a weighting function determining the influence of each metric tensor component, and $\mathrm{u} = (u_1, u_2, u_3)$. This internal potential energy formulation stores the energy as the elastically deformable model of the myocardium deviates from its reference configuration, while it releases the energy as the configuration of the model recovers its reference configuration as described in section 5.2. Because it is also assumed that the myocardium is an isotropic material, the internal deformation potential energy can have only two weighting functions corresponding to on- and off-diagonal elements of the metric tensor, which quantify distance deviations and angle deviations from the reference configuration, respectively.

The external potential energy $E_{external}(\mathbf{p})$ associates the elastic deformation of the myocardium with externally applied forces and consists of two components: the motion potential energy $E_{motion}(\mathbf{p})$ and the image potential energy $E_{image}(\mathbf{p})$. The motion potential energy $E_{motion}(\mathbf{p})$ is derived from the force that attracts the model to the tracked position

of the myocardium by velocity integration and is defined by:

$$E_{motion}(\mathbf{p}) = \int_0^1 \int_0^1 \int_0^1 \beta(\mathrm{u}) \sum_{i=1}^{3} (\mathbf{p}_i - \mathbf{p}_i^0)^2 du_1 du_2 du_3 \tag{60}$$

where $\beta(\mathrm{u})$ is a weighting function determining the influence of the tracked position of a tissue point on the myocardium by velocity integration and $\mathbf{p}^0$ is the tracked position of a tissue point on the myocardium by velocity integration in the subsequent time frame (deformed state). Because the two in-plane (u_1 and u_2 in Cartesian coordinate system) spatial resolutions of the velocity images from phase contrast MRI are usually identical and higher than the out-of-plane (u_3) resolution, $\beta(\mathrm{u})$ is solely a function of the out-of-plane directional distance between the current position of $\mathbf{p}$ and the position of the imaging plane and is inversely proportional to the distance (i.e., smaller the distance, higher the weighting value). $\beta(\mathrm{u})$ can be seen as a confidence measure of the velocity value at the current location of a tissue point on the myocardium. Then, highly weighted model points close to the imaging plane tend to move to the tracked positions of corresponding tissue points by velocity integration, while lowly weighted model points away from the imaging plane tend to move in terms of the elastic property of the deformable model of the myocardium. This implies that the tracked positions of tissue points on the myocardium by velocity integration with less reliable velocity values can be

refined by the elastic property of the myocardium.

$\mathbf{p}^0$ is obtained by integrating velocity values of tissue points in the current time frame (reference state) as a function of time:

$$\mathbf{p}^0 = \mathbf{p}^r + v(\mathbf{p}^r)\Delta t \tag{61}$$

where Δt is the time interval (phase delay) between the current and the subsequent frame of a phase contrast MR image sequence, $\mathbf{p}^r$ is the spatial position of a tissue point in the current frame, and $v(\mathbf{p}^r)$ denotes the velocity value at position $\mathbf{p}^r$. Because the in-plane spatial variation of the velocity value in a single voxel is small, the simple nearest neighbor interpolation technique is used for the in-plane directional spatial modeling of $v(\mathbf{p}^r)$. However, because the out-of-plane resolution of multi-slice phase contrast MRI is usually poorer than the in-plane resolution, the linear spatial modeling technique [79] is used for the out-of-plane directional spatial modeling of $v(\mathbf{p}^r)$. Let (u_1, u_2, u_3) be the spatial position in Cartesian coordinate system, then the intra-voxel velocity variation can be expressed as:

$$v(u_1,u_2,u_3) = v(u_1^0,u_2^0,u_3^0) + (\nabla v)\cdot \begin{bmatrix} u_1-u_1^0 \\ u_2-u_2^0 \\ u_3-u_3^0 \end{bmatrix} + \cdots \tag{62}$$

where (u_1^0, u_2^0, u_3^0) is the center of voxel (u_3^0 is the slice position) and ∇v is velocity gradient. If the higher-(second or higher) order terms are truncated, then it becomes the linear spatial interpolation. In the case of the nearest-neighbor interpolation, constant velocity within each voxel is assumed, and the velocity value for all locations inside the voxel is $v(u_1^0, u_2^0, u_3^0)$.

The image potential energy $E_{image}(\mathbf{p})$ is derived from the force that attracts the boundaries of the model to the closest endocardial and epicardial boundary in the phase contrast MRI magnitude image and is defined by:

$$E_{image}(\mathbf{p}) = \int_0^1 \int_0^1 \int_0^1 \tau(\mathrm{u}) \sum_{i=1}^{3} (\mathbf{p}_i - \mathbf{p}_i^b)^2 du_1 du_2 du_3 \qquad (63)$$

where $\tau(\mathrm{u})$ a weighting function and $\mathbf{p}^b$ is the closest position of zero-crossing of the Laplacian of a Gaussian smoothed phase contrast MR magnitude image in the subsequent frame. Because the velocity values around endocardial and epicardial boundaries are often noisy, this image potential energy derived from image boundary information makes it possible to reduce the tracking errors of the boundaries of the myocardium. Finally, the motion potential energy and the image potential energy are combined into the external potential energy:

$$E_{external}(\mathbf{p}) = \begin{cases} \omega \cdot E_{motion}(\mathbf{p}) + (1-\omega) \cdot E_{image}(\mathbf{p}), & \text{if } \mathbf{p} \text{ belongs to the boundaries} \\ E_{motion}(\mathbf{p}), & \text{otherwise} \end{cases} \quad (64)$$

where ω is a weighting coefficient ($0 \leq \omega \leq 1$), which is determined experimentally to produce the optimal results.

By balancing the internal and external potential energies (minimizing the total potential energy), the estimated configuration of the model of the myocardium will have a minimal deviation from its reference configuration while having the most similar deformation with a tracked configuration of the myocardium by velocity integration. In practice, a solution set of position vectors $\mathbf{p}$, which minimizes the total energy $E_{total}(\mathbf{p})$ can be found by the variational approach (the calculus of variations). Instead of directly solving the above static problem, a dynamically deformable model system, which unifies the description of shape and motion of the myocardium as briefly described in section 5.2, will be constructed and solved numerically in the next section.

5.3.2 Dynamically Deformable Model and Numerical Solution Procedure

Solving the static problem described in the previous section can only produce the final deformed (tracked) configuration of the model of the myocardium at a particular time instance (frame) of the phase contrast MRI data set. By applying the principle of Lagrangian mechanics, the dynamic behavior of the elastically deformable model of the myocardium between the given two time frames can be estimated, so intermediate configurations of the model can also be estimated.

The dynamic behavior of the elastically deformable model of the myocardium can be described by Lagrange's equations of motion as described in section 5.2 and given here again:

$$\mu\frac{\partial^2\mathbf{p}}{\partial t^2}+\gamma\frac{\partial\mathbf{p}}{\partial t}+\delta_{\mathbf{p}}E_{deformation}(\mathbf{p})=\mathbf{f} \tag{65}$$

where $\delta_{\mathbf{p}}E_{deformation}(\mathbf{p})$ is the simplified internal elastic force derived from the deformation potential energy and represents the first variational derivative of the energy $\frac{\delta E_{deformation}(\mathbf{p})}{\delta\mathbf{p}}$. The simplified internal elastic force can be approximated by:

$$\delta_{\mathbf{p}}E_{deformation}(\mathbf{p})=\sum_{i,j=1}^{3}-\frac{\partial}{\partial u_i}\left(\alpha_{ij}(\mathrm{u})\left(G_{ij}(\mathbf{p})-G_{ij}^{0}(\mathbf{p})\right)\frac{\partial\mathbf{p}}{\partial u_j}\right) \tag{66}$$

The complete derivation of this simplified internal elastic force of the elastically deformable model is presented in Appendix B.

Because Equations (65) and (66) are continuous expressions of the partial differential equation of motion and the internal elastic force, discretization of these equations is needed to solve the problem numerically. For this purpose, the standard finite-difference approximation method is applied to transform the partial differential equation of motion into a system of ordinary differential equations [87, 90] as follows. Let us first consider the continuous expression of the internal elastic force. With time-independent notations, the domain $\Omega = 0 \le u_1, u_2, u_3 \le 1$ is discretized into a regular $M \times N \times L$ discrete grid Ω^h of nodal variables such that $\mathbf{p}[m, n, l] = \mathbf{p}(h_1 m, h_2 n, h_3 l)$, where $h_1 = 1/(M-1)$, $h_2 = 1/(N-1)$, $h_3 = 1/(L-1)$, $0 \le m \le M$, $0 \le n \le N$, and $0 \le l \le L$. Then, the first forward (D^+) and backward (D^-) difference operators of $\mathbf{p}[m, n, l]$ can be defined as:

$$
\begin{aligned}
D_1^+ \mathbf{p}[m, n, l] &= \frac{(\mathbf{p}[m+1, n, l] - \mathbf{p}[m, n, l])}{h_1} \\
D_2^+ \mathbf{p}[m, n, l] &= \frac{(\mathbf{p}[m, n+1, l] - \mathbf{p}[m, n, l])}{h_2} \\
D_3^+ \mathbf{p}[m, n, l] &= \frac{(\mathbf{p}[m, n, l+1] - \mathbf{p}[m, n, l])}{h_3}
\end{aligned}
\tag{67}
$$

$$D_1^- \mathbf{p}[m, n, l] = \frac{(\mathbf{p}[m, n, l] - \mathbf{p}[m-1, n, l])}{h_1}$$
$$D_2^- \mathbf{p}[m, n, l] = \frac{(\mathbf{p}[m, n, l] - \mathbf{p}[m, n-1, l])}{h_2} \quad (68)$$
$$D_3^- \mathbf{p}[m, n, l] = \frac{(\mathbf{p}[m, n, l] - \mathbf{p}[m, n, l-1])}{h_3}$$

Using the above difference operators, the discretized internal elastic force can be approximated by:

$$\boldsymbol{\varepsilon}[m, n, l] = \sum_{i,j}^{3} -D_i^- \left(w_{ij}[m, n, l] \, D_j^+ \mathbf{p}[m, n, l] \right) \quad (69)$$

where $w_{ij}[m, n, l] = \alpha_{ij}[m, n, l]\left(D_i^+ \mathbf{p}[m, n, l] \cdot D_j^+ \mathbf{p}[m, n, l] - G_{ij}^0[m, n, l]\right)$ and $\alpha_{ij}[m, n, l]$ is the discrete counterpart of $\alpha_{ij}(\mathrm{u})$. By rearranging the right side of the above equation and denoting $\mathbf{p}[m, n, l]$ and $\boldsymbol{\varepsilon}[m, n, l]$ as $\mathbf{p}'$ and ε' respectively, the discretized internal elastic force can be written as:

$$\boldsymbol{\varepsilon}' = \mathbf{K}(\mathbf{p}')\, \mathbf{p}' \quad (70)$$

where $\mathbf{K}(\mathbf{p}')$ is called a stiffness matrix. The next step is to discretize the mass density $\mu(u_1, u_2, u_3)$ and the damping density $\gamma(u_1, u_2, u_3)$ as $\mu[m, n, l]$ and $\gamma[m, n, l]$, and construct mass and damping matrices. In finite element analysis [91], the mass matrix can be assembled from element mass matrices by expressing the mass density in terms of the interpolating functions and integrating over the element. The damping matrix can similarly be obtained by assembling contributions from element damping parameters.

However, because it is usually difficult to determine these damping parameters, the damping matrix is often approximated as a linear combination of mass and stiffness matrix, or mass alone [92]. For simplicity and computational efficiency of our system, the mass matrix (**M**) is defined by a diagonal lumped (i.e., the mass is assumed to be concentrated at a nodal point) matrix with $\mu[m, n, l]$ as diagonal components, and the damping matrix (**C**) is defined by the simplified linear relationship $\mathbf{C} = \alpha\mathbf{M}$. For further simplicity, an identity matrix is used for the mass matrix, and α is chosen experimentally to minimize the vibrating behavior of the model during evolving to equilibrium. Then, the external force is discretized into $\mathbf{f}_{external}(\mathbf{p}')$:

$$\mathbf{f}_{external}(\mathbf{p}') = \begin{cases} \omega \cdot \left(\sum_{m,n,l}^{M,N,L} \beta(\mathbf{u}) \left\| \mathbf{p}' - \mathbf{p}'^{0} \right\|^2 \right) \\ + (1-\omega) \cdot \left(\sum_{m,n,l}^{M,N,L} \tau(\mathbf{u}) \left\| \mathbf{p}' - \mathbf{p}'^{b} \right\|^2 \right), & \text{if } \mathbf{p}' \text{ belongs to the boundaries} \\ \sum_{m,n,l}^{M,N,L} \beta(\mathbf{u}) \left\| \mathbf{p}' - \mathbf{p}'^{0} \right\|^2, & \text{otherwise} \end{cases} \quad (71)$$

Finally, a system of the second-order ordinary differential equations, which describes the dynamical behavior of the elastically deformable model of the myocardium, can be expressed as:

$$\mathbf{M}\frac{d^2\mathbf{p}'}{dt^2} + \mathbf{C}\frac{d\mathbf{p}'}{dt} + \mathbf{K}(\mathbf{p}')\mathbf{p}' = \mathbf{f}_{external}(\mathbf{p}') \quad (72)$$

where t is a time variable.

To solve the system numerically, the semi-implicit time-integration technique [87] is applied. First, $\boldsymbol{\varepsilon}'$ and $\mathbf{f}_{external}$ are computed at $t+\Delta t$ and t, respectively, and the discrete-time operators are approximated by:

$$\frac{d^2\mathbf{p}'}{dt^2} \approx \frac{\mathbf{p}'_{t+\Delta t} - 2\mathbf{p}'_t + \mathbf{p}'_{t-\Delta t}}{\Delta t^2} \tag{73}$$

$$\frac{d\mathbf{p}'}{dt} \approx \frac{\mathbf{p}'_{t+\Delta t} - \mathbf{p}'_{t-\Delta t}}{2\Delta t}, \tag{74}$$

Then, a linear system for $\mathbf{p}'_{t+\Delta t}$ is obtained by substituting Equations (73) and (74) into Equation (72):

$$\mathbf{A}_t\ \mathbf{p}'_{t+\Delta t} = \mathbf{g}'_t \tag{75}$$

$$\mathbf{A}_t(\mathbf{p}'_t) = \mathbf{K}(\mathbf{p}'_t) + \left(\frac{1}{\Delta t^2}\mathbf{M} + \frac{1}{2\Delta t}\mathbf{C}\right) \tag{76}$$

$$\mathbf{g}'_t = \mathbf{f}_{external,t} + \left(\frac{1}{\Delta t^2}\mathbf{M} + \frac{1}{2\Delta t}\mathbf{C}\right)\mathbf{p}'_t + \left(\frac{1}{\Delta t}\mathbf{M} - \frac{1}{2\Delta t}\mathbf{C}\right)\dot{\mathbf{p}}'_t \tag{77}$$

$$\dot{\mathbf{p}}'_t = \frac{\mathbf{p}'_t - \mathbf{p}'_{t-\Delta t}}{\Delta t} \tag{78}$$

By recursively solving this system with initial conditions of $\mathbf{p}'_t$ and $\dot{\mathbf{p}}'_t$ at $t = 0$, the model can evolve to equilibrium and exhibit physically meaningful dynamic behaviors.

5.4 Model Geometry

In this section, techniques for constructing the initial geometrical representation of the LV from phase contrast MRI data set are described. The techniques in this section can be directly extended to the RV with minor changes.

5.4.1 Boundary Segmentation

To construct a volumetric representation of the LV from the multiple two-dimensional slices of phase contrast MRI, segmentation of both the endocardial and epicardial boundaries are first needed. Velocity-aided cardiac segmentation method developed in Part I of this thesis is used to obtain both the endocardial and epicardial boundaries in the two-dimensional image slices at the first time frame, as shown in Figure 22. Initial contours are placed manually around either the endocardial or epicardial boundary, and the segmentation algorithm is applied to each boundary. This process is repeated until all the boundaries in the entire slices are segmented, and then the segmented boundaries are stacked together, as shown in Figure 23. Some manual corrections are performed where the segmented locations are considered significant errors.

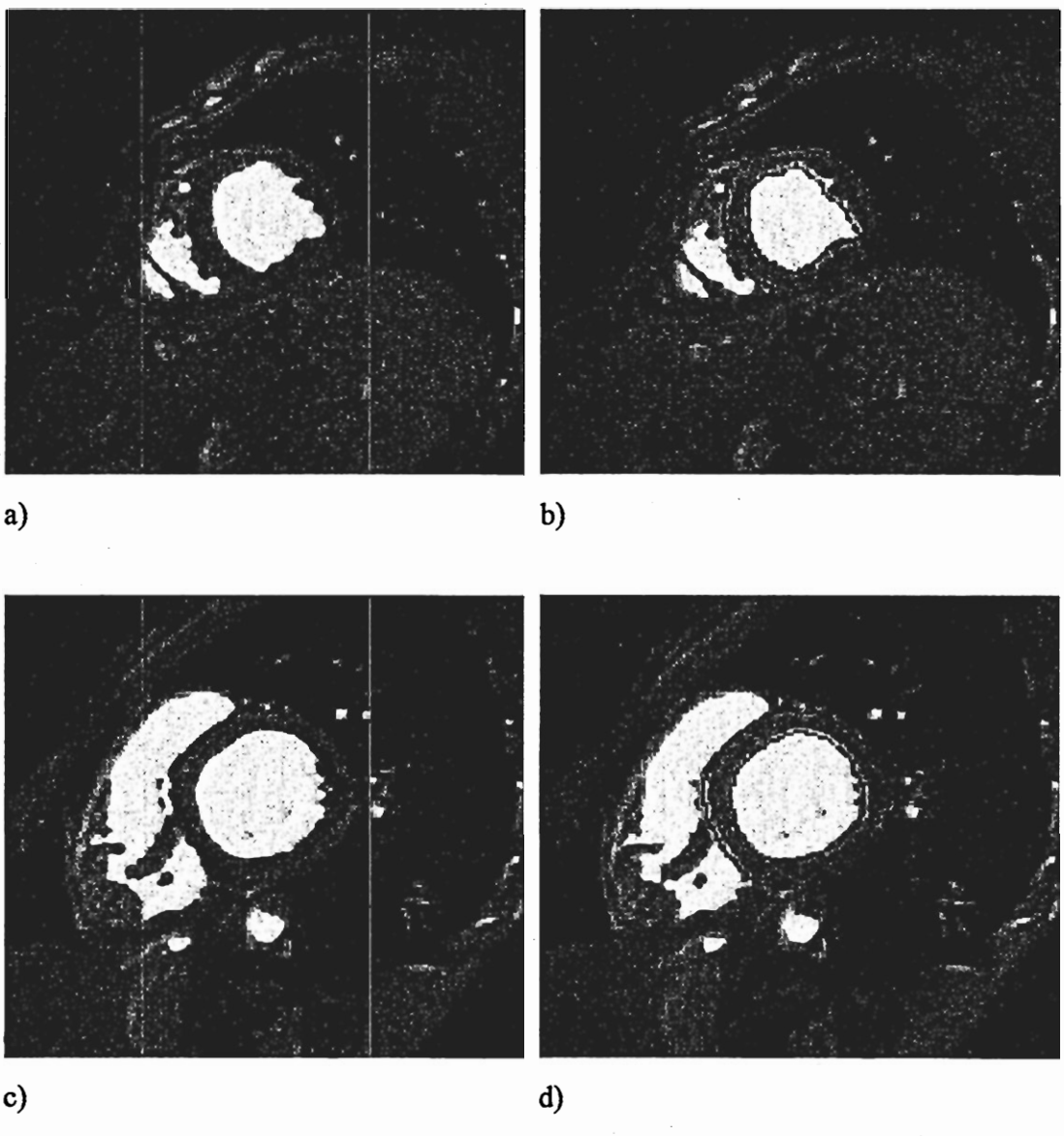

Figure 22. Boundary segmentation of human LV at the first time frame. a) original magnitude image of phase contrast MRI around the apex. b) the segmented endocardial (red) and epicardial (blue) boundaries are superimposed on the same magnitude image. c) original magnitude image around the base. d) the segmented endocardial and epicardial boundaries are superimposed on the same magnitude image.

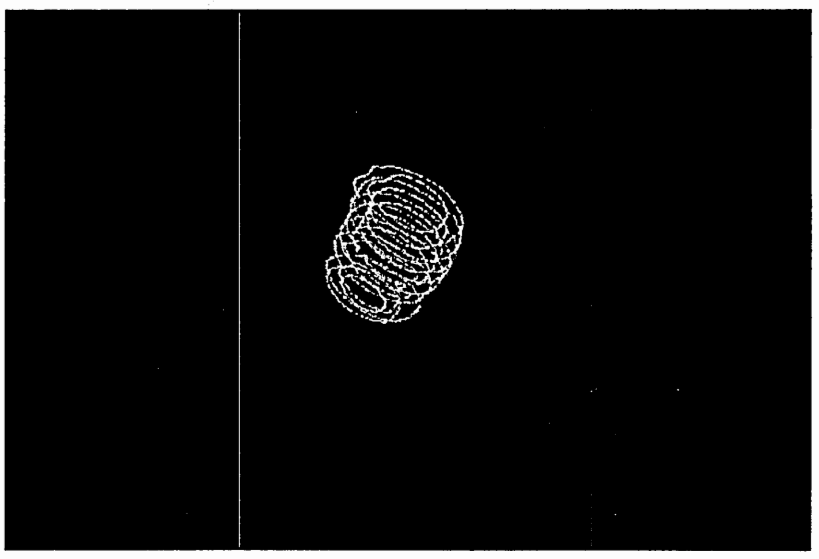

a)

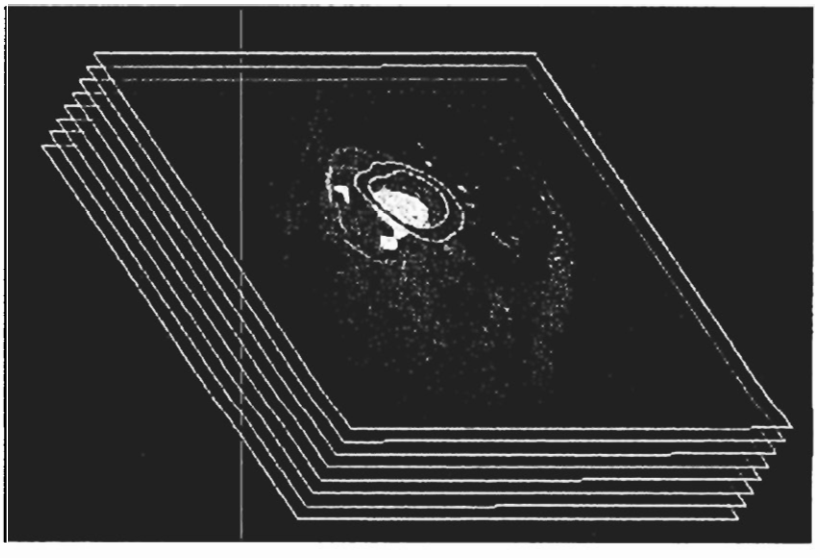

b)

Figure 23. Segmented myocardial boundaries. a) A stack of the segmented endocardial (yellow) and epicardial (white) boundaries of human LV. b) the segmented endocardial and epicardial boundaries are superimposed on a stack of the two-dimensional magnitude images of phase contrast MRI.

5.4.2 Slice Interpolation

As most three-dimensional imaging modalities, such as MRI and computerized tomography (CT), phase contrast MRI also produces a series of two-dimensional image slices that usually have higher in-plane resolution than out-of-plane (through-plane) resolution. Therefore, quantitative analysis of images from such modalities often suffers from the lack of out-of-plane resolution, and the three-dimensional cardiac motion analysis even more suffers from it because of the out-of-plane motion of the myocardium. One of the classical solutions for this problem is to interpolate the given slices to estimate the missing slices between them, and then use this extended data set for further processing. Because our initial model geometry is based only on the endocardial and epicardial boundary information of the LV, a shape-based contour interpolation method is used to provide an extended data set for the shape description of the LV.

The shape-based contour interpolation method [93] consists of two main processes: distance map transformation, and linear interpolation of the distance maps. The distance map transformation is performed by two consecutive chamfering processes, where the first chamfering updates the pixels row by row from top to bottom with a left-to-right ordering within the rows using the template in Figure 24 a), and the second

chamfering updates the pixels row by row from bottom to top with a right-to-left ordering within the rows using the template in Figure 24 b). These chamfering processes convert the segmented contour image (slice), which is initialized with positive numbers inside the contour and negative numbers outside the contour, into a grayscale image. The resulting grayscale image represents the chamfer distance map of the segmented contour. Then, the linear interpolation of the chamfer distance maps at the two consecutive slice positions is performed to obtain missing contour images between two slice positions. Finally, thresholding of the obtained contour images at zero produces interpolated contours. These chamfering and linear interpolation processes are repeated until all the interpolated endocardial and epicardial contours are found. Figure 25 shows the results of this shape-based contour interpolation of the endocardial and epicardial boundary contours.

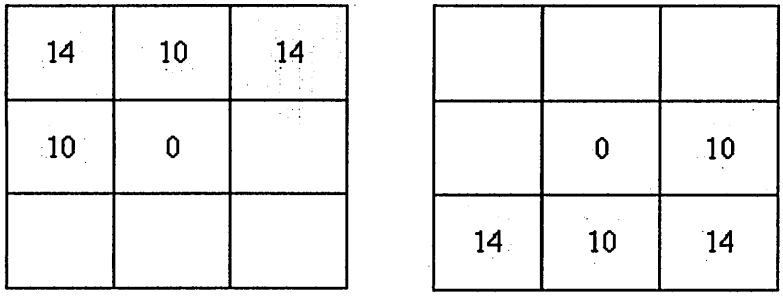

Figure 24. 3 x 3 templates for chamfering processes. a) template for the first chamfering. b) template for the second chamfering.

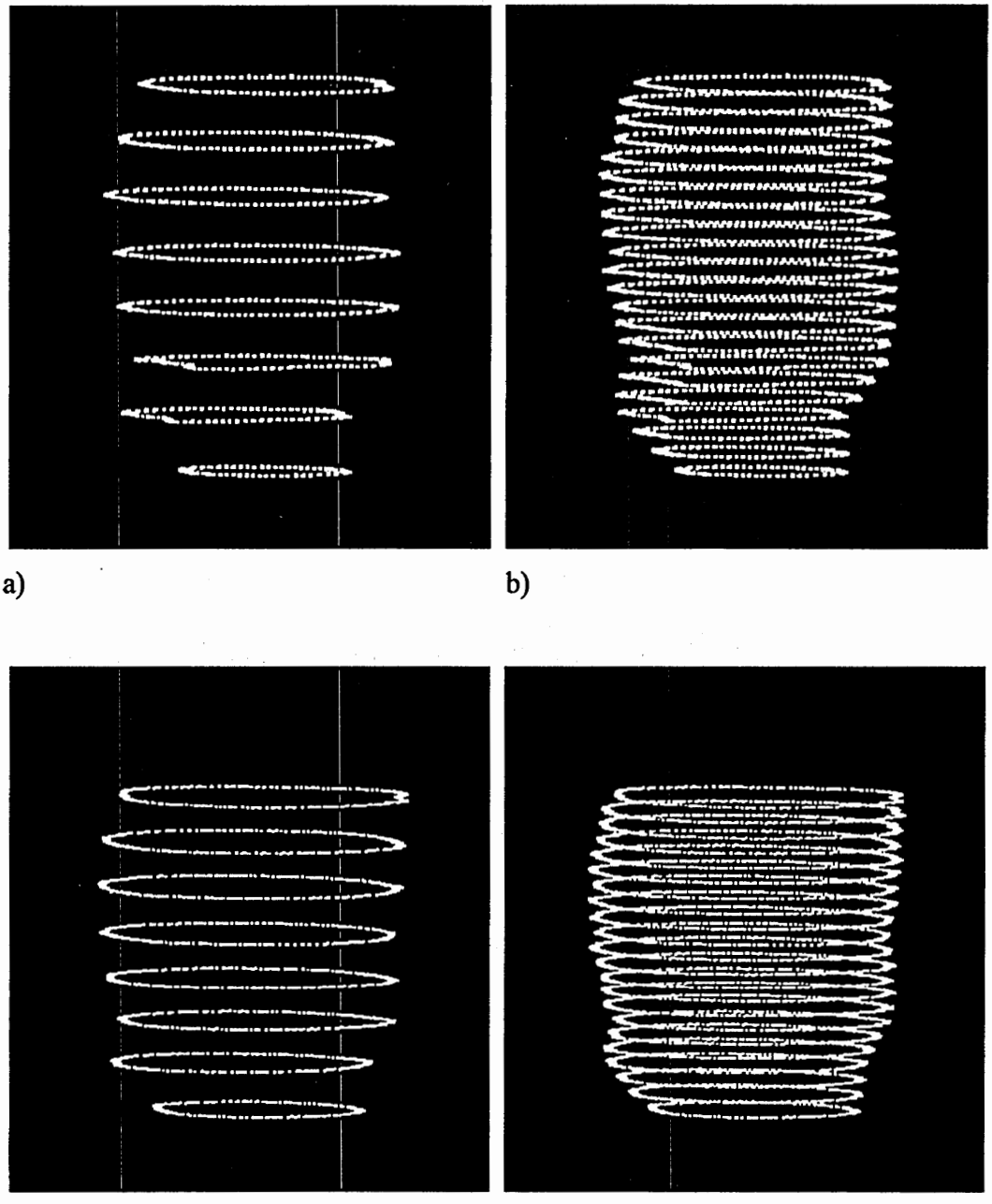

Figure 25. Results of the shape-based contour interpolation. a) given endocardial boundary contours. b) interpolated boundary contours. c) given epicardial boundary contours. d) interpolated boundary contours.

5.4.3 Data Point Sampling

To construct an elastically deformable volumetric model of the LV, a set of three-dimensional data points need to be sampled not only from the segmented and/or interpolated boundary contours, but also from the mid-wall region that is bounded by the endocardial and epicardial boundaries. Data point sampling is performed such that an initial model with the hexahedral lattice structure can be constructed. The hexahedral lattice structure is chosen because of its simplicity in setting up the neighboring information of the model points between neighboring slices. An example of the hexahedral lattice structure is shown in Figure 26.

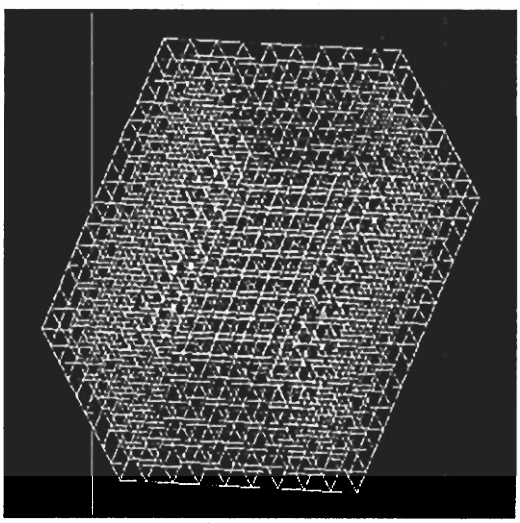

Figure 26. An example of the hexahedral lattice structure.

The endocardial and epicardial boundaries are sampled at the intersections of boundaries and radial lines, which are originated from the center of mass of the LV and evenly distributed in central angle. The numbers of sample data points are determined by the hexahedral lattice structure used. Figure 27 shows examples of the endocardial and epicardial boundary sample data points. Data points of mid-wall region are sampled uniformly between the neighboring endocardial and epicardial sample data points depending on the number of mid-wall data points needed. Examples of the two-dimensional sample data points including mid-wall points and a set of the entire three-dimensional sample data points are shown in Figure 28.

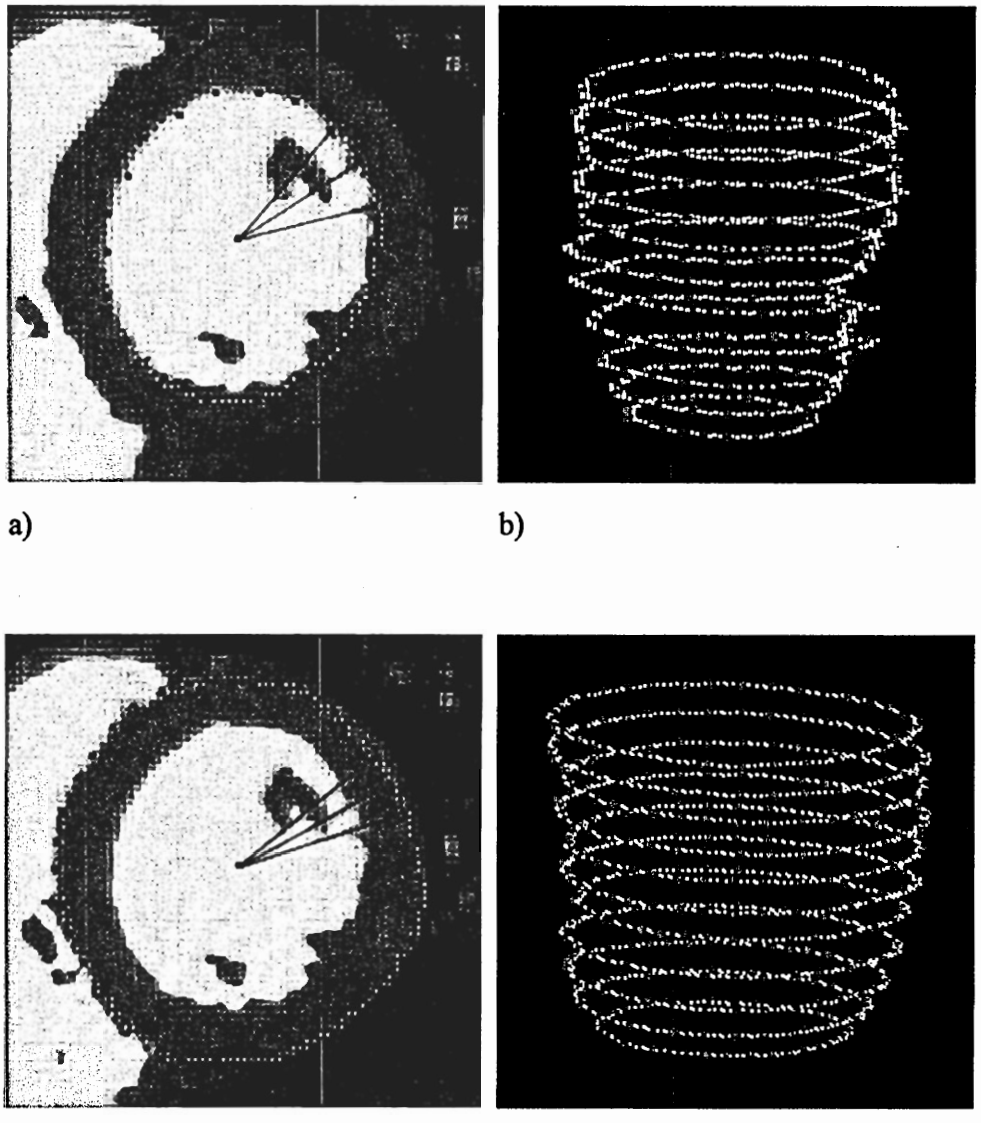

Figure 27. Examples of the endocardial and epicardial sample data points. a) the radial lines and endocardial sample data points are superimposed on the segmented two-dimensional magnitude image. b) a stack of the endocardial sample data points. c) the radial lines and epicardial sample data points are superimposed on the segmented two-dimensional magnitude image. d) a stack of the epicardial sample data points.

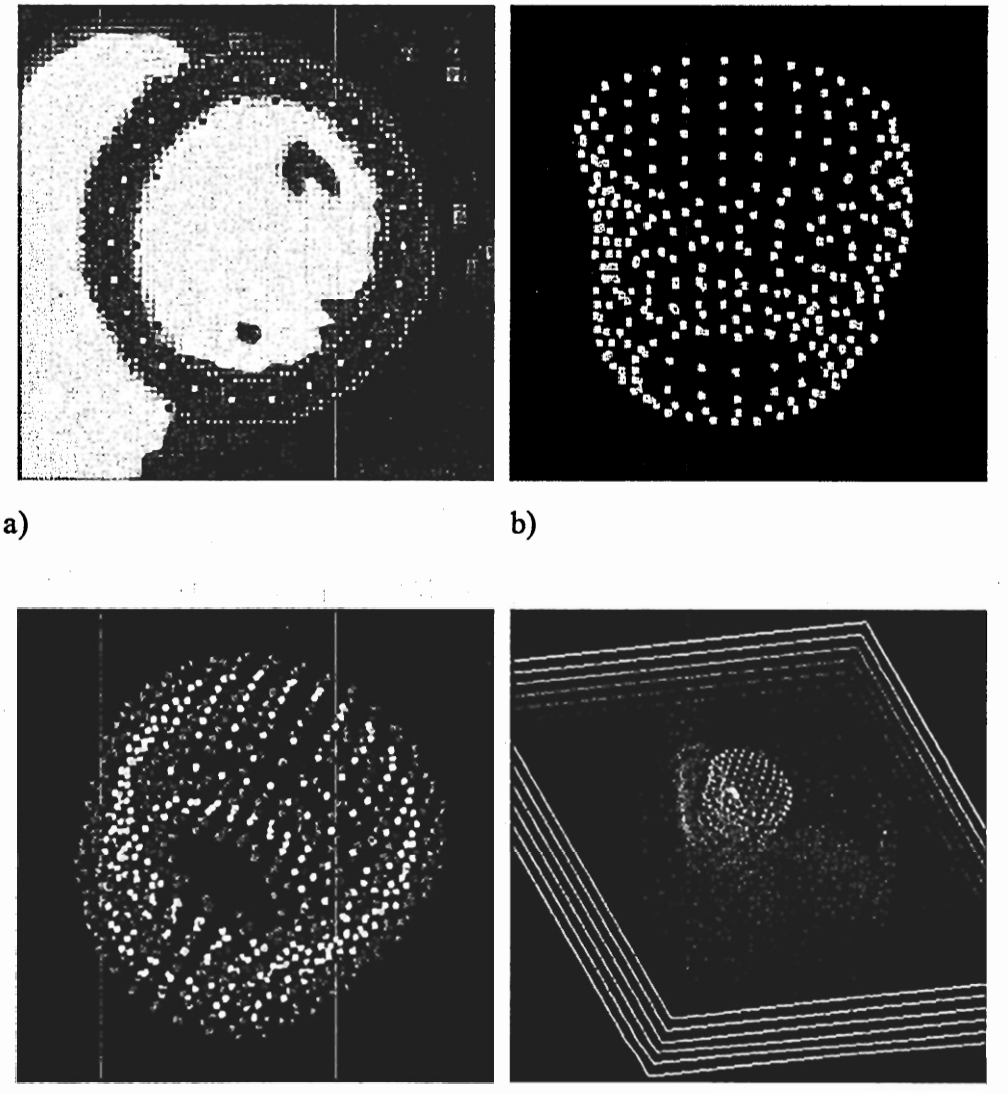

Figure 28. Examples of the mid-wall sample data points and a set of the entire three-dimensional sample data points. a) the mid-wall sample data points are superimposed on the segmented two-dimensional magnitude image. b) a stack of the mid-wall sample data points. c) a set of the entire three-dimensional sample data points. d) a set of the sample data points are superimposed on a stack of the two-dimensional magnitude images of phase contrast MRI.

5.5 Overall Motion-Tracking Procedure

With the system of the cardiac motion-tracking model described in section 5.3 and the initial model geometry of the LV described in the previous section, motion-tracking of the LV throughout the entire cardiac cycle is performed as follows. The initial equilibrium configuration of the model at the first cardiac frame (end diastole) is first set up based on the locations of the sample data points. The distances between the sample data points and the corresponding initial model points with the hexahedral lattice structure are used to generate an equilibrium force, which maintains the equilibrium configuration of the model. This force is constant over time and implicitly incorporated into the governing equations of motion Equation (72) by setting the equilibrium configuration as the reference configuration (the metric tensor of the undeformed state, G^0). An example of the initial equilibrium (reference) configuration of the model at the first frame is shown in Figure 29. Then, $\mathbf{p}^0$ for $E_{motion}(\mathbf{p})$ is calculated by velocity integration with the linear spatial modeling, and the zero-crossing of the Laplacian of a Gaussian smoothed magnitude image in the next frame is calculated for $E_{image}(\mathbf{p})$. Then, $\mathbf{p}'_t$ at $t = 0$ is initialized by using the reference configuration, and $\dot{\mathbf{p}}'_t$ at $t = 0$ is set to zero. Finally, with these reference configuration and initial conditions, the dynamically

deformable model system is solved (i.e., the system evolves to equilibrium), and the motion trajectories and final tracked locations of myocardial tissue points between the first (end diastole) and the next cardiac frames are obtained.

The above motion-tracking process between two consecutive cardiac frames is first repeated in forward direction (e.g., frame $0 \rightarrow 1 \rightarrow \cdots \rightarrow 19$) until the last frame of the cardiac cycle is processed. Because periodic motion of the myocardium ensures that a tissue point in the first frame returns to its starting position in the end of the cardiac cycle and combining the forward and backward directional motion trajectories can reduce the errors of the velocity offset as described in section 4.2, the whole process is repeated again in backward direction (e.g., frame $0 \rightarrow 19 \rightarrow 18 \rightarrow \cdots \rightarrow 1$). Then, the forward and backward directional results are linearly combined into the final results with the weighting coefficients $w_f = 1 - t/T$ and $w_b = t/T$, where t is the current frame number and T is the total number of frames in a cardiac cycle.

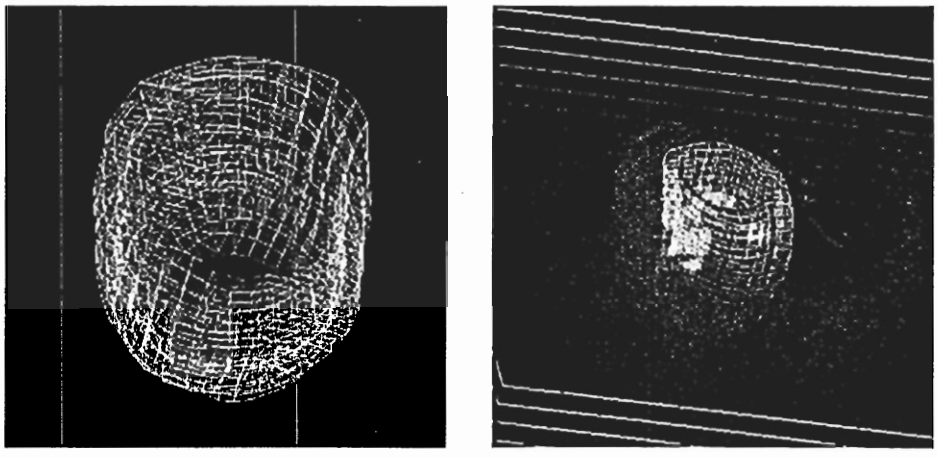

Figure 29. An example of the initial reference configuration at the first frame (end diastole).

5.6 Experimental Results

In this section, experimental results of the proposed cardiac motion-tracking method are presented. First, the tracking results of a normal human LV are compared with a color-coded tissue Doppler echocardiography data set. Then, strain analysis is performed for quantitatively analyzing the motion and deformation of the LV.

5.6.1 Comparisons

Although tracking of the myocardial motion using implanted markers or sonomicrometers is considered the "*gold standard*," it is invasive. In this thesis, a color-

coded tissue Doppler echocardiography data set was used to noninvasively compare the results of the proposed cardiac motion-tracking method. The same phase contrast MRI data set of the LV of a normal human volunteer (i.e., male, 22 year-old) described in section 3.7.1 was used to produce the outputs of the proposed cardiac motion-tracking method. To construct the initial model of the LV at end diastole, the shape-based slice interpolation method was first applied, and then total 924 points were sampled from the phase contrast MRI data set. Both the weighting function $\alpha(u)$ for the internal deformation potential energy and $\tau(u)$ for the image potential energy were set to the constant value 1.0, and $\beta(u)$ for the motion-potential energy was dynamically set to a value between 0 and 1.0 depending on the distance between the current position of a model point and the position of the nearest imaging plane. Then, the motion of the LV throughout the entire cardiac cycle (20 frames) was tracked using the procedure described in section 5.5. Figure 30 shows the tracked motion of the LV throughout the entire cardiac cycle by volumetric meshes.

The color-coded tissue Doppler echocardiography data set of the same volunteer as the phase contrast MRI data set was acquired using a Philips 7500 ultrasound system with a 2.5 MHz transducer at Sibley Heart Center Cardiology at Children's Healthcare of

Atlanta. Scan parameters were as follows: the spatial resolution was 512× 512, the temporal resolution was 40-frames per cardiac cycle (i.e., approximately 20-msec), and each frame was the two-dimensional color-coded tissue Doppler image scanned in apical four chamber view with the maximum and minimum encoding velocity ±4.5 cm/sec. A typical anatomical location of the apical four chamber view image slice and the anatomical location of the acquired color-coded tissue Doppler image slice are shown in Figure 31 a) and b), respectively. Selected frames of the color-coded tissue Doppler echocardiography data set are also shown in Figure 31 c).

The out-of-plane directional velocity values from the tissue Doppler image and the three-dimensional motion-tracking model at the septum of the LV were compared throughout the entire cardiac cycle using the correlation coefficient (r) as follows. First, the nearest model points at the intersection of the tissue Doppler image slice and the LV model were determined, and the model points of the endocardium, mid-ventricle, and epicardium at three different longitudinal levels (around the apex, mid-ventricle, and base) were selected, as shown in Figure 32. The distances between the selected model points and the tissue Doppler image slice were usually less than 3 mm (i.e., less than two pixels in in-plane resolution of phase contrast MRI) for the case of 924 sample points.

Then, the positions of the selected model points were projected onto the tissue Doppler image slice, and the velocity values at the projected positions were retrieved. Although the velocity values in the tissue Doppler image of the apical four chamber view at the septum were measured approximately in the apex-to-base direction, these velocity values are projected onto the exact out-of-plane direction of phase contrast MRI data set, as shown in Figure 33. Finally, the above process was repeated frame-by-frame throughout the entire cardiac cycle, and correlation coefficients of the out-of-plane directional velocity values derived from our LV motion-tracking model and the tissue Doppler image were calculated.

Comparison results using the correlation coefficients of the out-of-plane directional velocity values are shown in Figure 34. Correlation coefficients were higher at the mid-ventricle level than other levels and lower at the mid-wall region than other regions within the same level. In general, the out-of-plane velocity values from the LV model were moderately well correlated with those from the color-coded tissue Doppler images. The discrepancy between the model-driven velocity values and the tissue Doppler velocity values might come from the flow-artifacts and velocity-offset errors of the phase contrast MRI data set. It might also come from the errors in aligning the tissue

Doppler slices into the phase contrast MRI data set and the errors in the tissue Doppler velocity values themselves. The simplified deformation potential energy formulation of the LV model, which can not fully reflect all the physical properties of the myocardium, might also cause the discrepancy. Because the acquired tissue Doppler velocity data were valid only in the septal region, comparisons were limited to the selected regions in the septum. Thus, the results of the measured correlation coefficients may not be generalized for the entire LV.

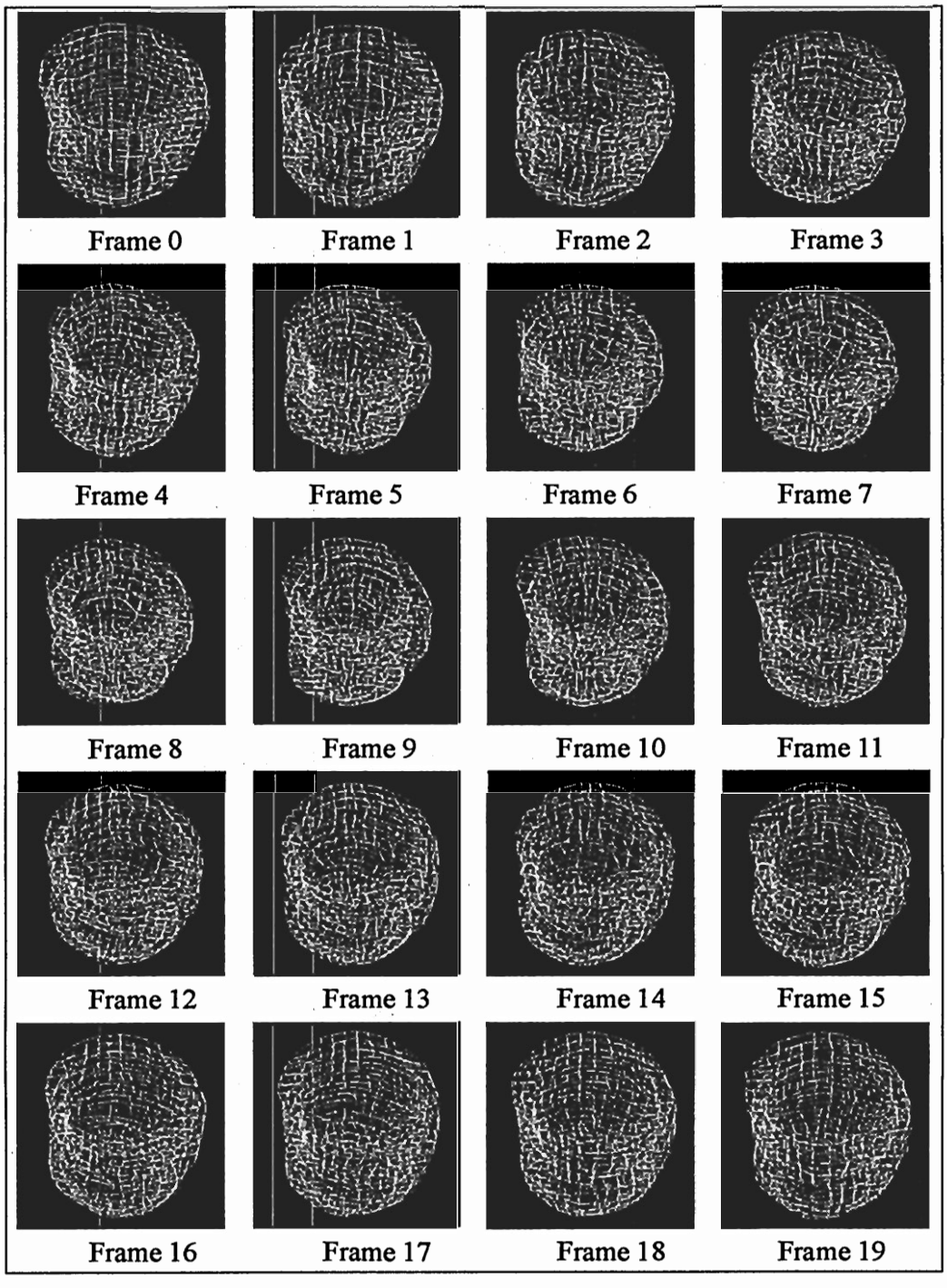

Figure 30. Volumetric meshes of a normal human LV tracked throughout the entire cardiac cycle (20 frames). Frame 0 is end diastole, and red wire-frame indicates the endocardium.

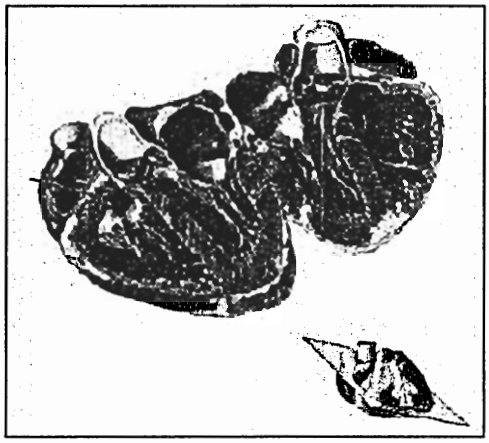

a)

b)

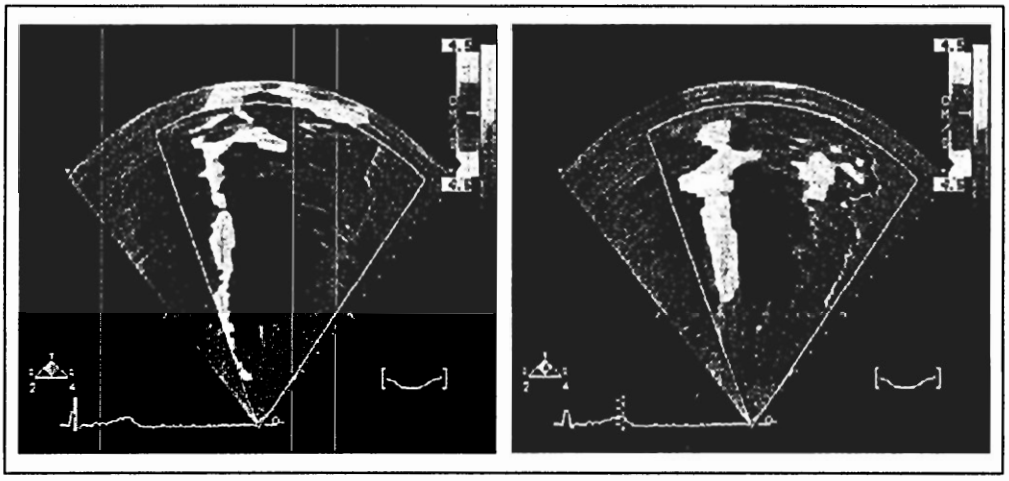

c)

Figure 31. a) A typical anatomical location of four chamber view image slice. b) the acquired color-coded tissue Doppler image slice is aligned with a long-axis magnitude image of phase contrast MRI data set. c) selected frames of the acquired color-coded tissue Doppler echocardiography data set. Image on the left is end diastole, and image on the right is end systole. Red indicates the velocity in the direction of toward-transducer (bottom-direction in the images), and blue indicates the velocity in the direction of away-transducer (top-direction in the images).

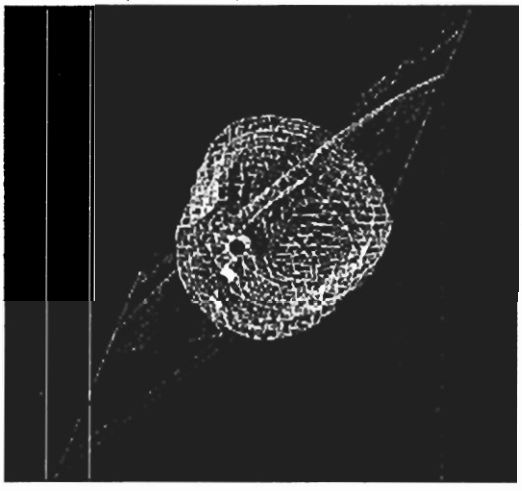

Figure 32. Positions of the selected model points at end diastole for comparison with the velocity values from the tissue Doppler image are indicated as spheres (red = endocardium, green = mid-wall, and blue = epicardium)

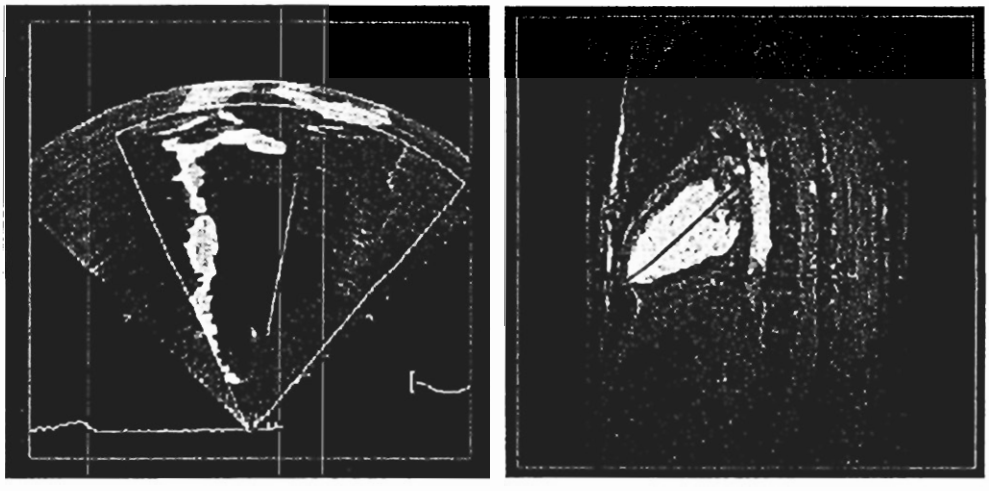

a) b)

Figure 33. The out-of-plane direction in a) the tissue Doppler echocardiograhy data set and b) phase contrast MRI data set. Red lines in both images indicate the out-of-plane direction.

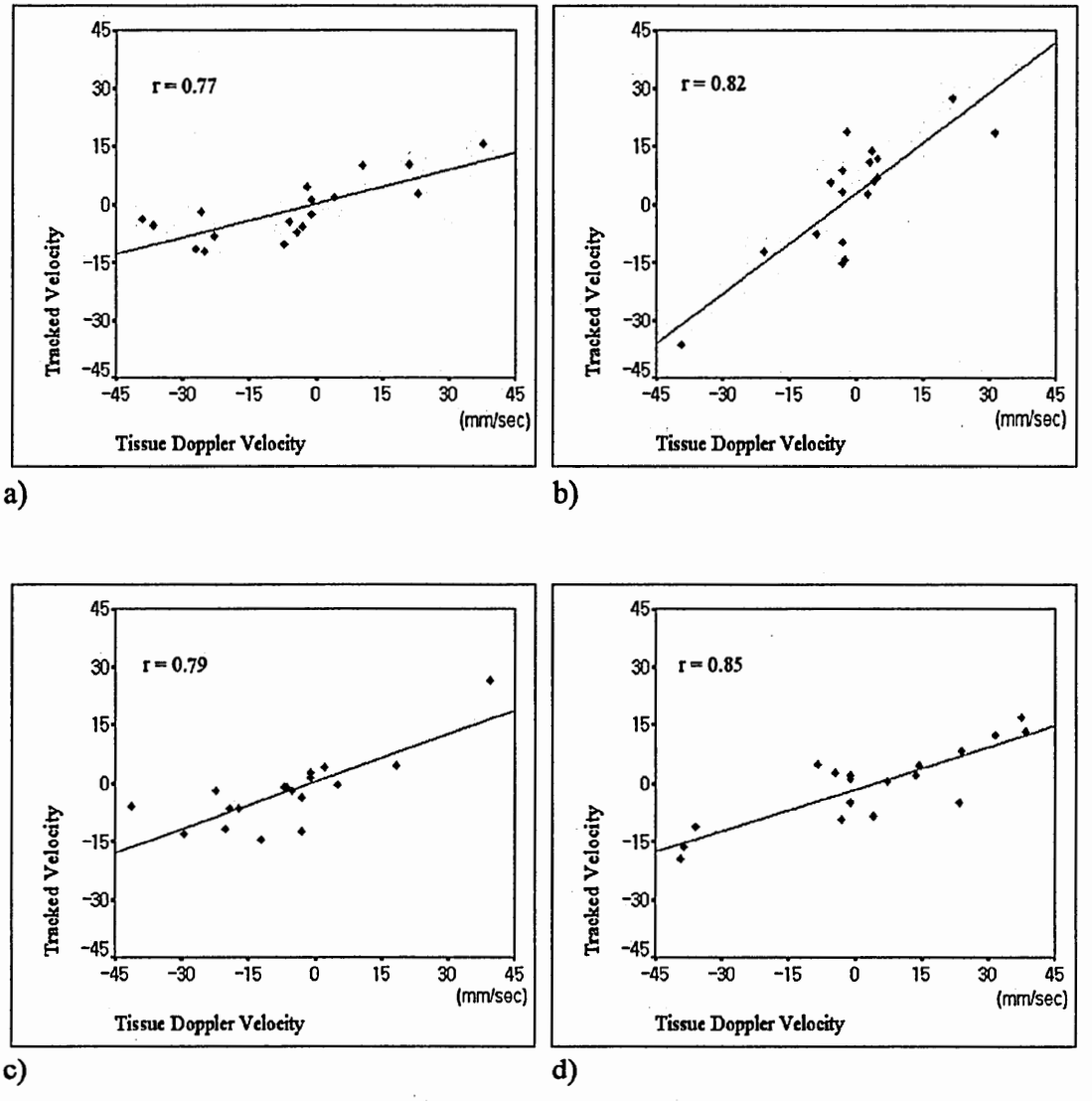

Figure 34. Correlation coefficients of the out-of-plane directional velocity values derived from the LV model and the tissue Doppler image. a) endocardial sample position at the basal level of the septum. b) mid-wall sample position at the basal level of the septum. c) epicardial sample position at the basal level of the septum. d) endocardial sample position at the mid-ventricular level of the septum.

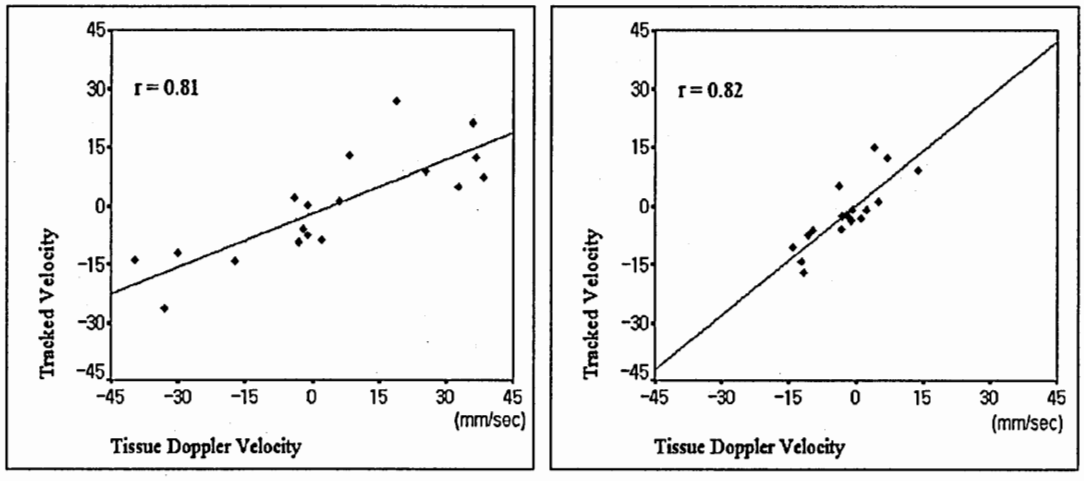

e)

f)

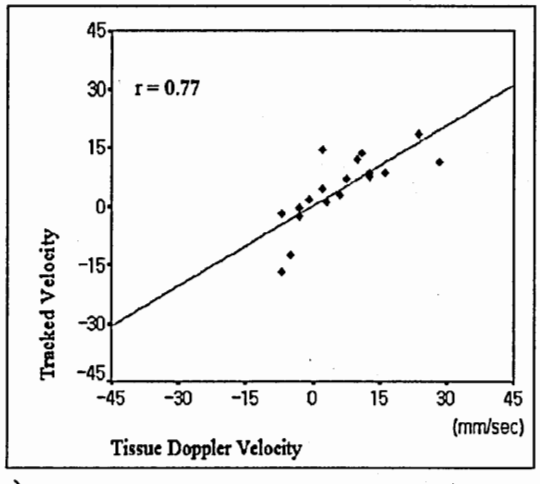

g)

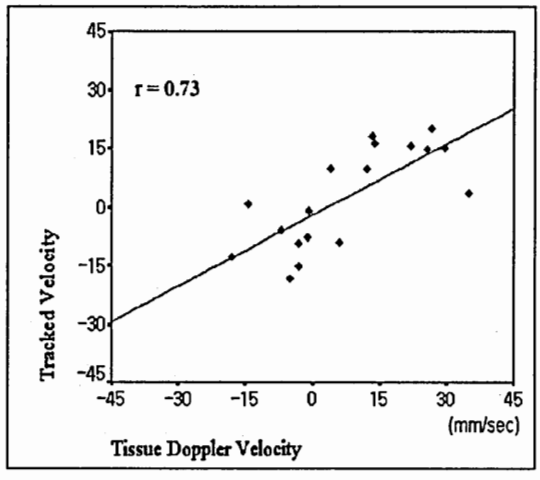

h)

Figure 34 (cont'd). e) mid-wall sample position at the mid-ventricular level of the septum. f) epicardial sample position at the mid-ventricular level of the septum. g) endocardial sample position at the apical level of the septum. h) mid-wall sample position at the apical level of the septum.

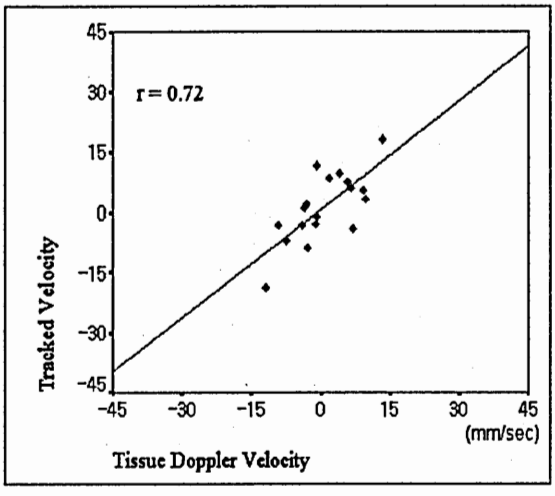

i)

Figure 34 (cont'd). i) epicardial sample position at the apical level of the septum.

5.6.2 Strain Analysis

For the purpose of quantitatively analyzing the results from the proposed cardiac motion-tracking method, strain analysis of a normal human LV was performed using the same experimental setting as the previous section. For strain analysis, the LV was divided into three longitudinal levels (apical, mid-ventricular, and basal level), and each level was further subdivided into four sub-regions (septal, anterior, lateral, and posterior sub-region), as shown in Figure 35. Then, the average strain values in these sub-regions of the LV were calculated.

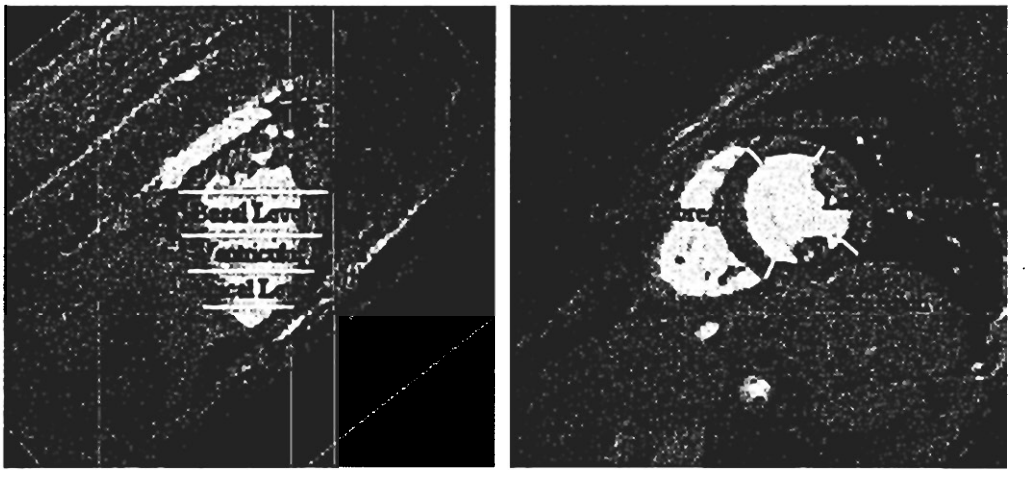

a) b)

Figure 35. Division of a human LV for strain analysis. a) three longitudinal levels are indicated on the long axis magnitude image. b) four sub-regions in the mid-ventricular level are indicated on the short axis magnitude image.

In order to define the strain of the LV, a three-dimensional coordinate system is first needed, and then each strain component (i.e., normal or shear component) can be measured depending on the coordinate system used. Because using the most appropriate coordinate system for the LV can not only facilitate the physical interpretation of strain measurements but also reduce the mathematical complexity required to describe the deformation, a specific coordinate system, called "*the local heart coordinate system* [94]", was used for strain analysis of the LV rather than using a simple global Cartesian coordinate system. For each tissue point in the myocardium, three mutually perpendicular axes are defined as follows:

1) The radial (R) axis: perpendicular to the epicardium pointing outwards.

2) The longitudinal (L) axis: perpendicular to the radial axis, and pointing towards the base of the LV.

3) The circumferential (C) axis: perpendicular to both the radial and longitudinal axis, defined in such a way that the R-L-C coordinate system is right-handed.

This local heart coordinate system is illustrated in Figure 36. Although this coordinate system cannot be defined around the most distal point of the apex of the LV, it can be generally used for strain measurements of the LV.

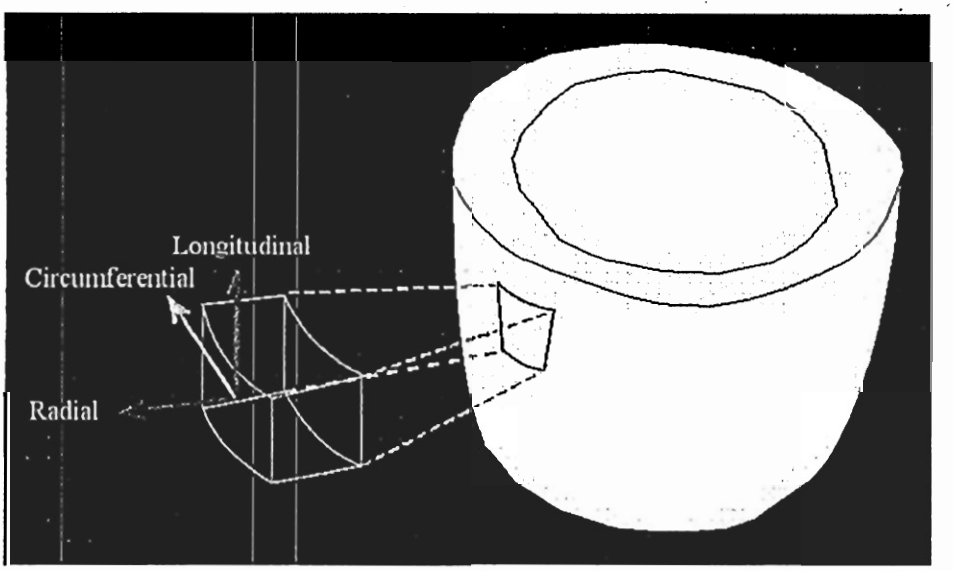

Figure 36. The local heart coordinate system defined for strain measurements of the LV. Red, blue, and green arrows indicate the radial, the longitudinal, and the circumferential axis, respectively.

Because the axial (normal) components of the myocardial strain defined in the local heart coordinate system are commonly used to measure deformation of the myocardium in the cardiology community, only the radial, circumferential, and longitudinal components of the myocardial strain were measured in this experiment. Figure 37 shows the temporal evolutions of the three axial strain components at different regions of the LV from end diastole to end systole. Even though the motion of the LV throughout the entire cardiac cycle was tracked, only the strain evolutions during the contraction phases are plotted because of their physiological importance. At all longitudinal levels and all sub-regions, the average radial, circumferential, and longitudinal strain values generally increased their magnitude as the cardiac cycle reached the end systole. At end systole, the average radial and circumferential strain values reached around 0.3 and -0.2, respectively. The average longitudinal strain values were relatively small compared with other two strain values. These indicate that thickening of the myocardium is primarily in the radial direction and shortening is in the circumferential direction. To less extent, shortening of the myocardium is undergone in the longitudinal direction. Extent of the myocardial deformation can be easily visualized using the color-coded strain maps, as shown in Figure 38.

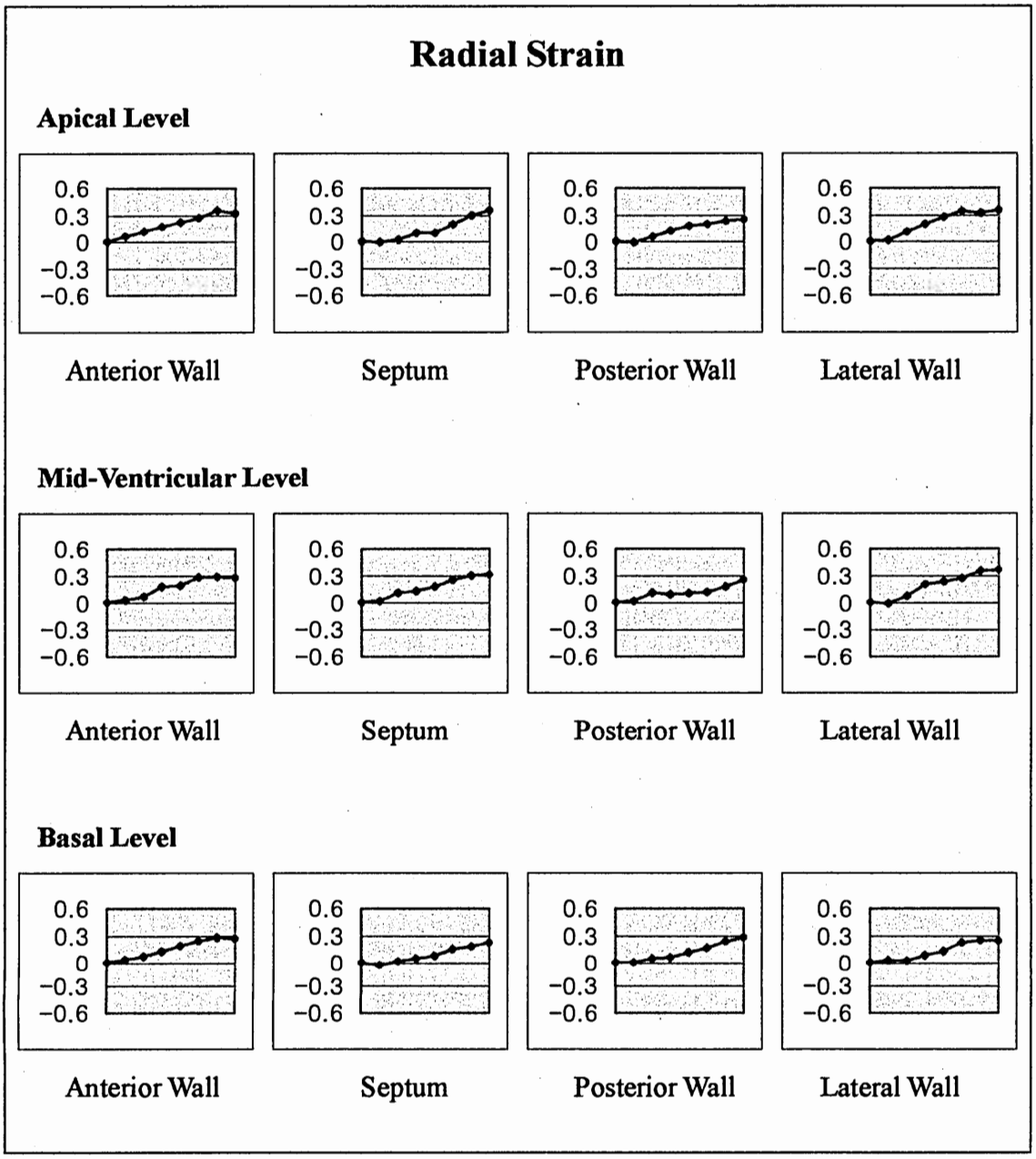

a)

Figure 37. a) Temporal evolutions of the radial strain component of a normal human LV at three longitudinal levels of four sub-regions. Each plot shows the strain evolution from end diastole to end systole.

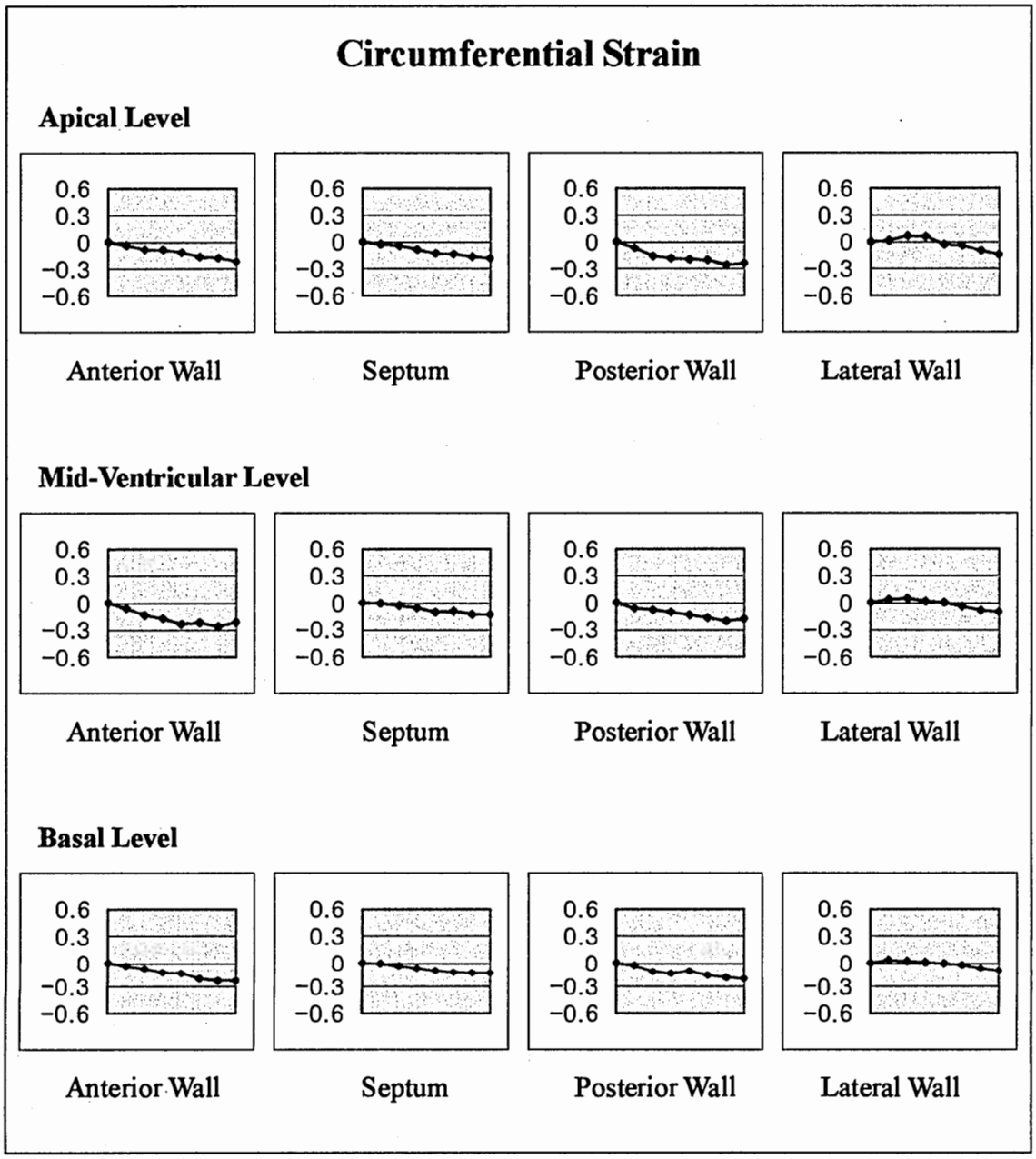

b)

Figure 37 (cont'd). b) Temporal evolutions of the circumferential strain component of a normal human LV at three longitudinal levels of four sub-regions. Each plot shows the strain evolution from end diastole to end systole.

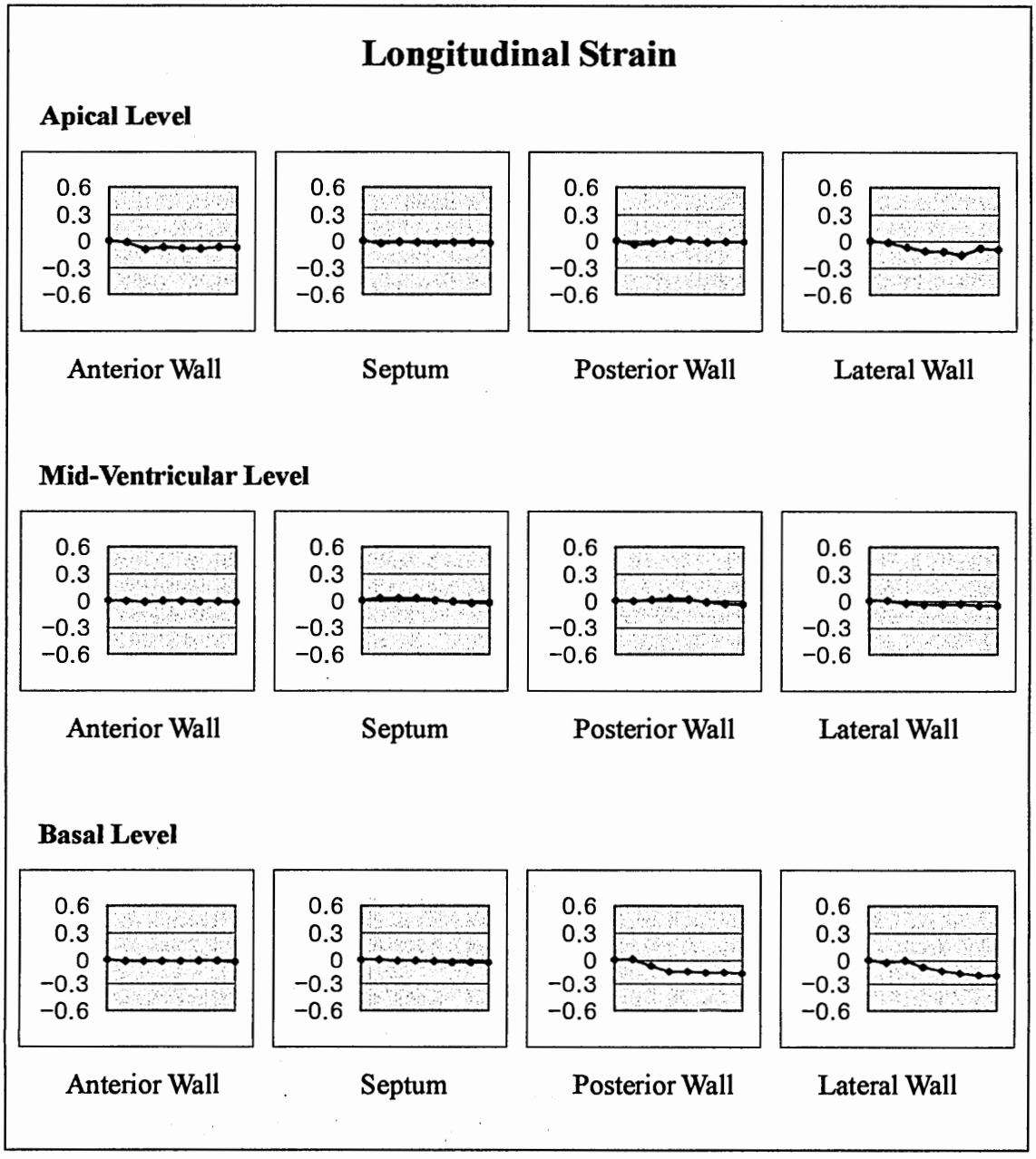

c)

Figure 37 (cont'd). c) Temporal evolutions of the longitudinal strain component of a normal human LV at three longitudinal levels of four sub-regions. Each plot shows the strain evolution from end diastole to end systole.

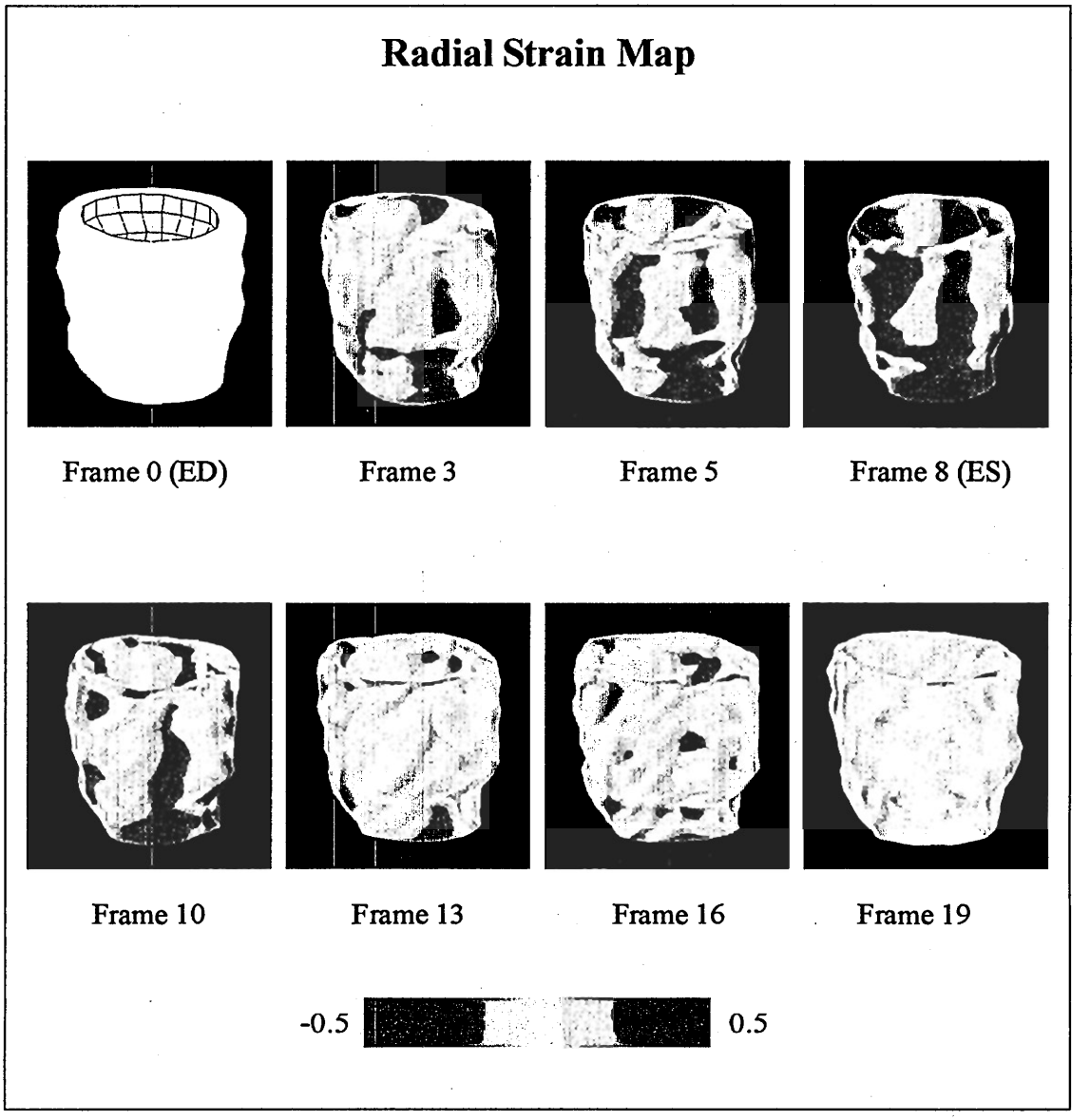

a)

Figure 38. Temporal sequences of the three different strain components of a normal human LV. Extent of the myocardial deformation is visualized using the color-coded strain maps. ED and ES represent end diastole and end systole, respectively. Red and blue indicate extension (lengthening) and contraction (shortening), respectively. a) selected frames of a sequence of the radial strain maps.

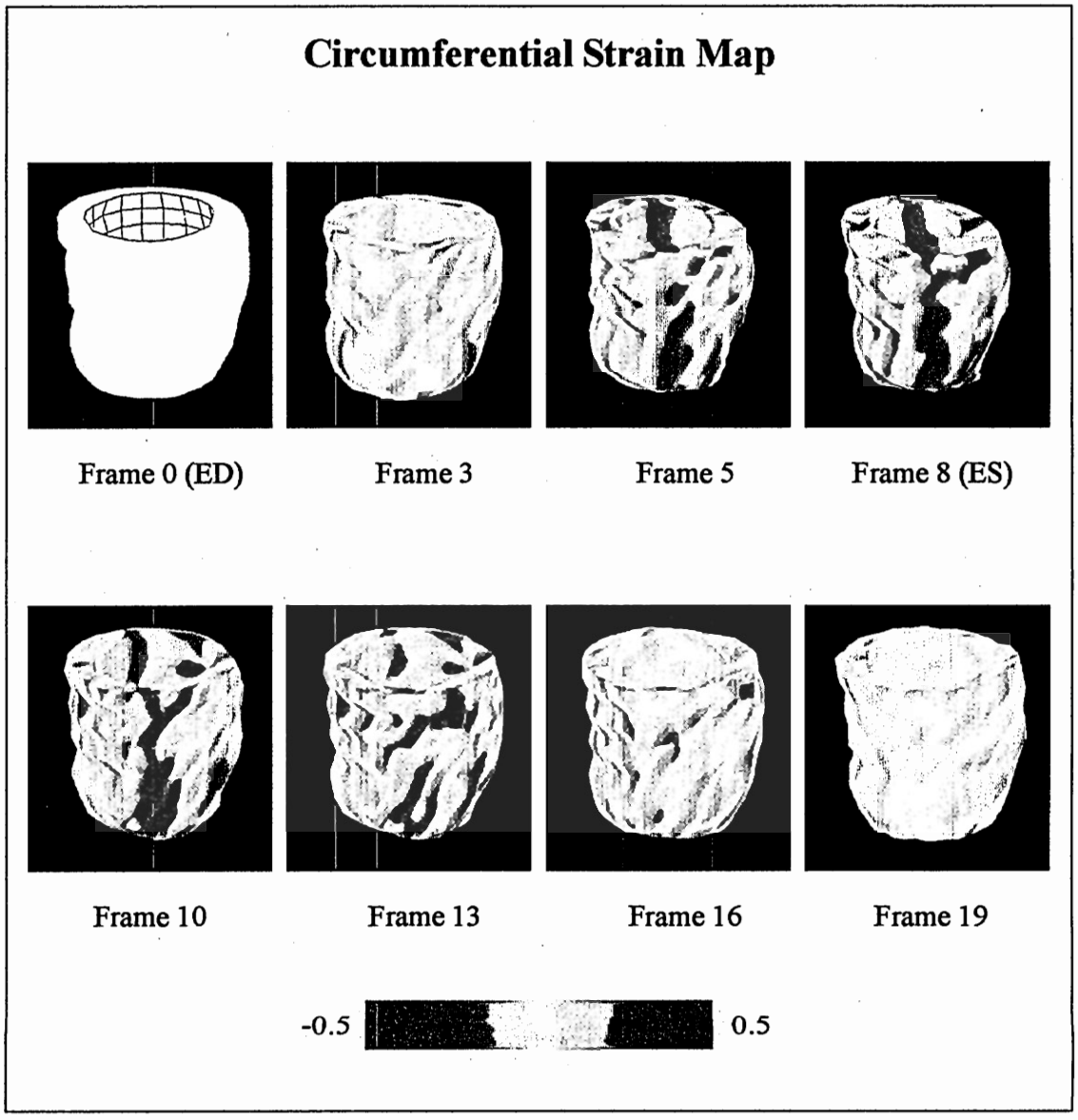

b)

Figure 38 (cont'd). b) selected frames of a sequence of the circumferential strain maps.

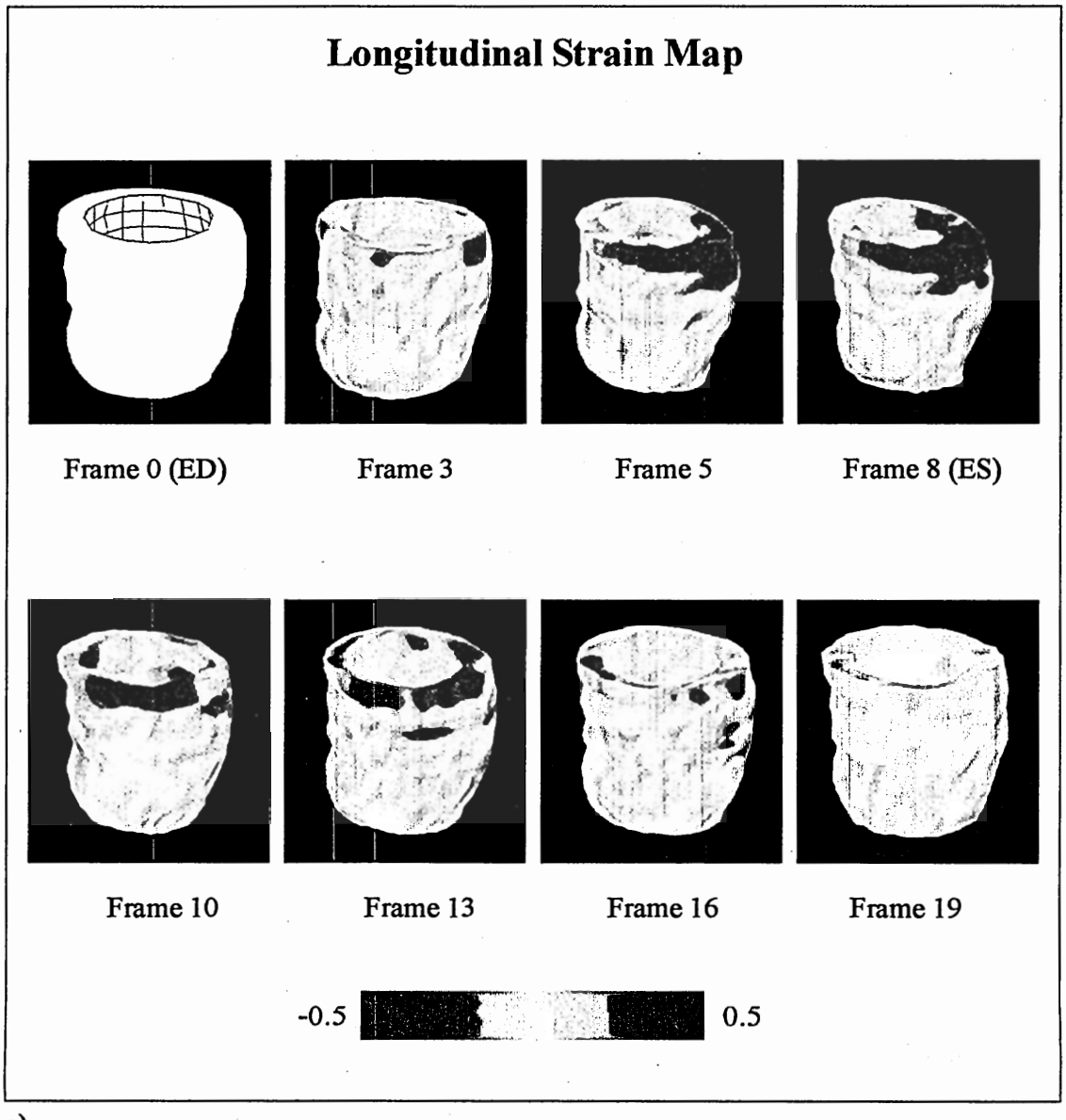

c)

Figure 38 (cont'd). c) selected frames of a sequence of the longitudinal strain maps.

The average strains in four sub-regions at three longitudinal levels of the LV at end systole are shown in Figure 39. At the apex, the septum and the lateral wall showed the greater radial strains than the anterior and posterior wall and their maximums are both around 0.33 (i.e., 33% extension). The circumferential strains were quite consistent over four sub-regions (around −0.2: i.e., −20% contraction). The magnitudes of the longitudinal strains in all sub-regions were relatively small with the greatest value 0.09 in the lateral wall. At the mid-ventricle, the radial strain was the greatest in the lateral wall (0.36) and the least in the posterior wall (0.25). The circumferential strains in the anterior (−0.2) and posterior wall (−0.18) were greater than the septum (−0.12) and the lateral wall (−0.1), and the consistency of the strains over four sub-regions decreased. Again, the magnitudes of the longitudinal strains in all sub-regions were relatively small compared with other strain components, and the septum and posterior wall had even positive strains (extensions). The positive longitudinal strains might be caused by the bending behavior of the LV along the longitudinal axis. At the base, the septum and the lateral wall showed the less radial strains (around 0.24) than other two sub-regions (around 0.27 in the anterior and posterior wall). The circumferential strains (around −0.1) in the septum and the lateral wall also showed the less strains than other two sub-regions (around −0.2 in

the anterior and posterior wall). In the average, the magnitudes of the circumferential strains at the base were similar to those at other longitudinal levels, but the consistency of the strains over four sub-regions further decreased. The longitudinal strains in the posterior and lateral wall (around −0.17) were greater than other two sub-regions (around −0.03) reflecting the greater longitudinal shortening.

The above strain measurements were compared with previously published values [13, 15, 45, 83, 95]. The average regional radial strains that ranged from a minimum of 0.24 and a maximum of 0.36 were higher than the previous studies. Errors in boundary segmentation and papillary muscles especially in the apical level of the LV might cause this higher estimation. However, variation of the radial strains across four sub-regions agreed with the previous studies. The average regional circumferential strains and their variation across four sub-regions agreed with the previous studies at all longitudinal levels (the differences in their magnitudes were less than 5%). The average longitudinal strains were generally lower than the previous studies. This might result from a potential over-smoothing of motion trajectories by the deformation potential energy, lacking of neighboring slice information at the most apical and basal levels, and the problem of defining the local heart coordinate system around the apex (i.e., a tilted longitudinal axis).

In general, our strain measurements were found to be consistent with previously published values.

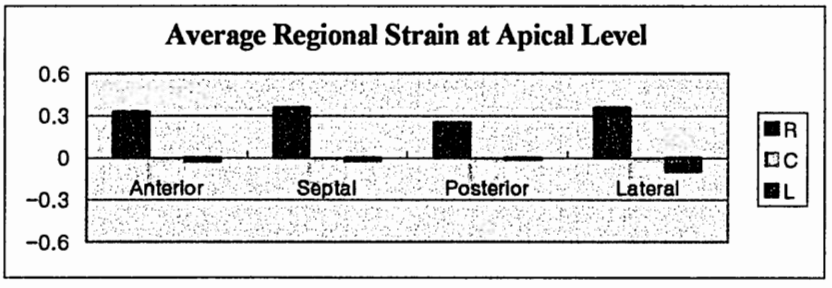

a)

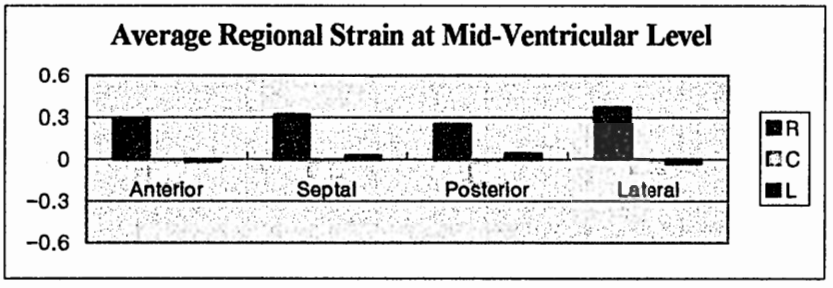

b)

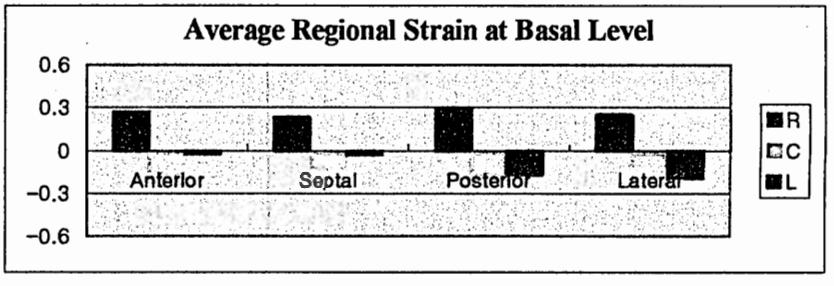

c)

Figure 39. The average radial (R), circumferential (C), and longitudinal (L) strains in the four different sub-regions of a normal human LV at end systole. a) at the apical level. b) at the mid-ventricular level. c) at the basal level.

5.7 Discussions and Conclusions

Estimation of dynamic characteristics of the myocardium is essential for the accurate diagnosis and treatment of heart disease because they are sensitive indicators of many types of heart disease. Although several MR imaging techniques, such as tagged MRI and phase contrast MRI, provide noninvasive tools for estimating the dynamic characteristics of the myocardium, difficulty still arises from the limitations of those imaging modalities, such as relatively low out-of-plane resolution.

A new cardiac motion tracking method based on elastic deformation estimation of a deformable model has been developed to track the three-dimensional motion of the myocardium. Elastic deformation estimation was performed to compensate for the effects of relatively low out-of-plane resolution of phase contrast MRI data set by balancing the internal elastic deformation potential energy of a deformable model and the external potential energy derived from both the magnitude and velocity images from phase contrast MRI. The advantage of this method is that it can provide a physically plausible yet computationally efficient and shape-independent framework for cardiac motion tracking.

Experiments have been performed on a phase contrast MRI data set of the LV of a normal human volunteer. The motion of the LV was tracked throughout the entire cardiac cycle, and then the results were compared with a color-coded tissue Doppler echocardiography data set. The comparison results showed that the out-of-plane velocity measurements from the LV model were correlated with those of the echocardiography data set at the selected regions in the septum. However, the motion of other regions (i.e., the anterior, posterior, and lateral wall) in the LV could not be compared because of the lack of velocity information of the tissue Doppler data set in those regions. Because they are adjacent to the regions with noisy velocity information, comparison with velocity information of the entire volume of the LV or invasive markers is desirable.

To quantitatively analyzing the results from the proposed cardiac motion-tracking method, a strain analysis of the motion and deformation of the LV was carried out. The results showed that the strain measurements were generally found to be consistent with previously published values. However, the reproducibility of the proposed method could not be fully investigated because of the limited number of the experimental data set. More study with various human subjects including normal and abnormal subjects is desirable.

Appendix A: Figures of Segmentation Results

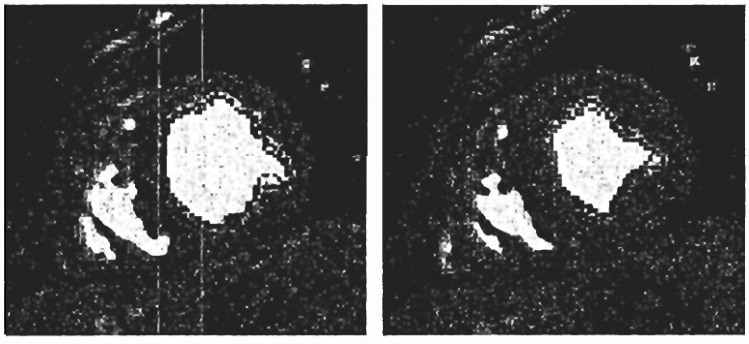

Frame 0 Frame 4

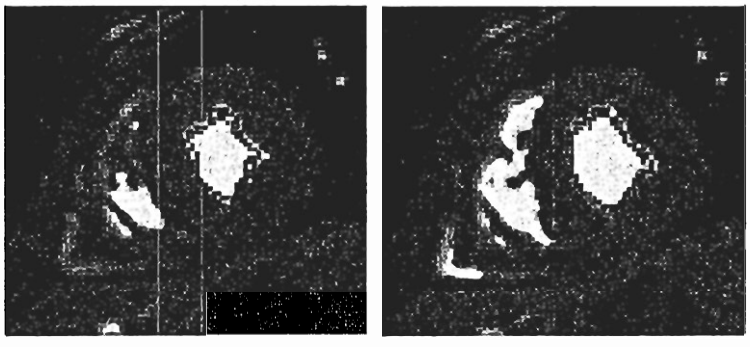

Frame 8 Frame 10

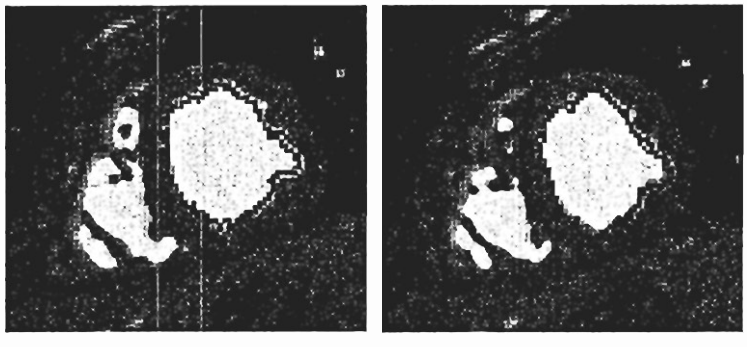

Frame 14 Frame 18

Figure A.1. Individual frame segmentation without the OGF at the apical level of LV. Blue dots indicate the reference boundary by manual segmentation, and red dots indicate the boundary by semiautomatic segmentation.

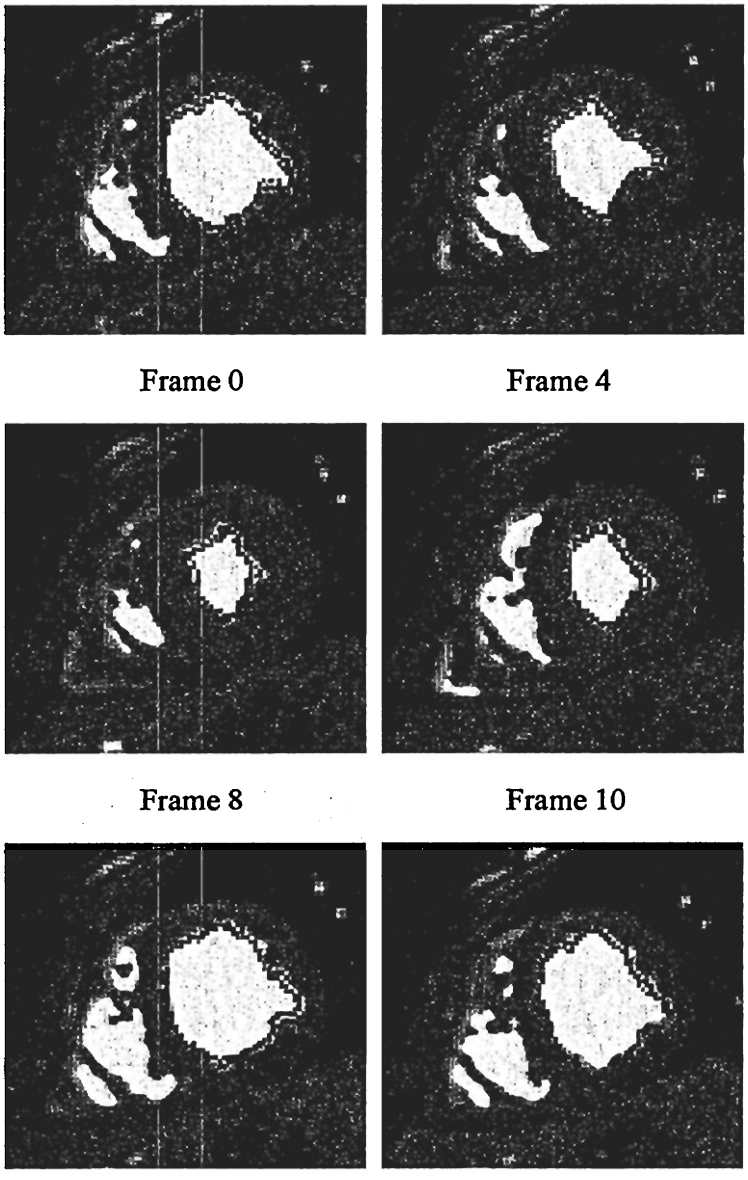

Figure A.2. Individual frame segmentation with the OGF at the apical level of LV. Blue dots indicate the reference boundary by manual segmentation, and red dots indicate the boundary by semiautomatic segmentation.

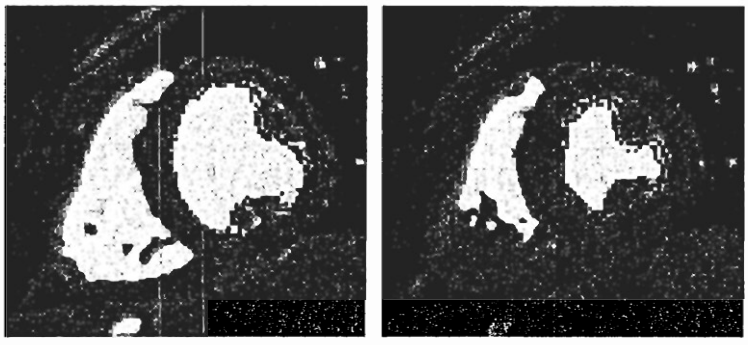

Frame 0 Frame 4

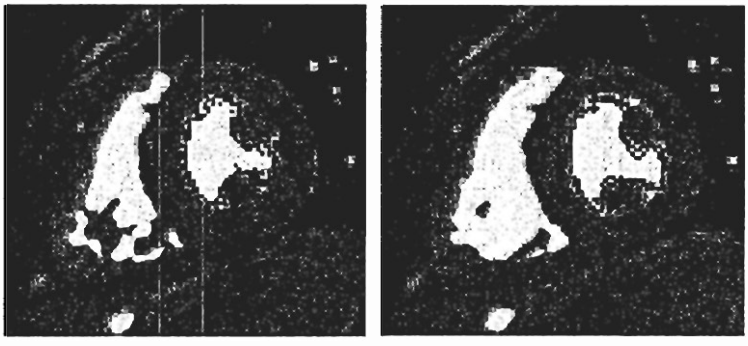

Frame 8 Frame 10

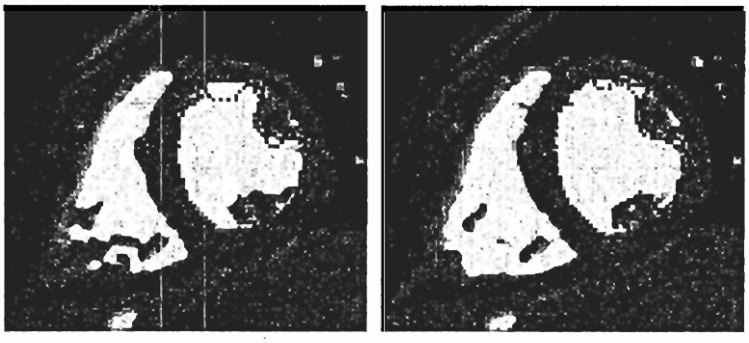

Frame 14 Frame 18

Figure A.3. Individual frame segmentation without the OGF at the mid-ventricle level of LV. Blue dots indicate the reference boundary by manual segmentation, and red dots indicate the boundary by semiautomatic segmentation.

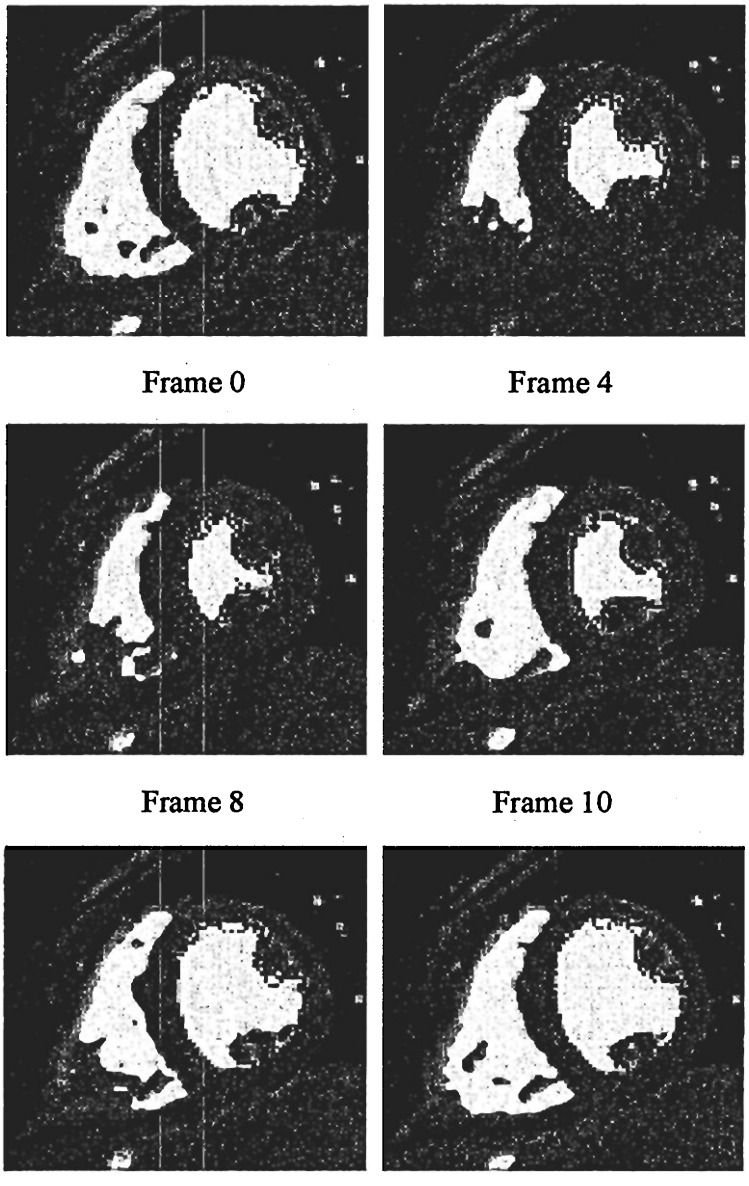

Figure A.4. Individual frame segmentation with the OGF at the mid-ventricle level of LV. Blue dots indicate the reference boundary by manual segmentation, and red dots indicate the boundary by semiautomatic segmentation.

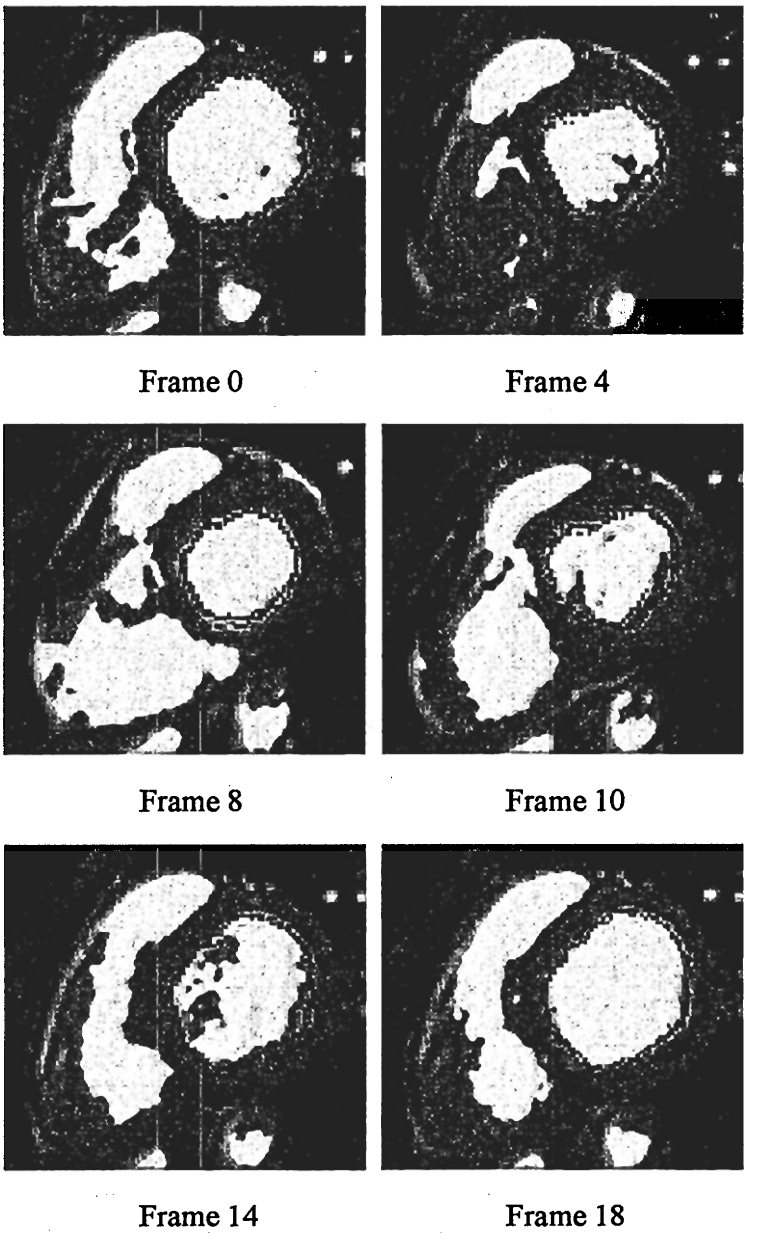

Figure A.5. Individual frame segmentation without the OGF at the basal level of LV. Blue dots indicate the reference boundary by manual segmentation, and red dots indicate the boundary by semiautomatic segmentation.

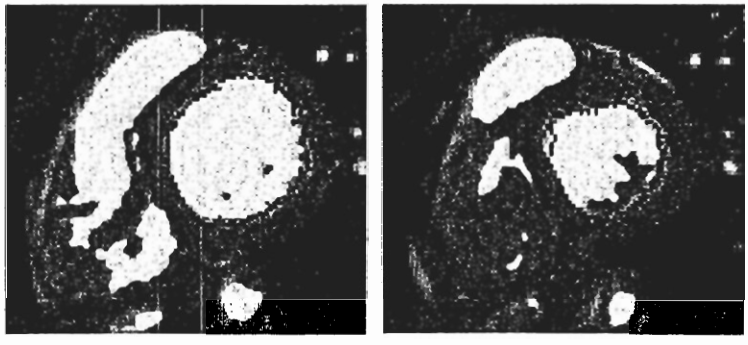

Frame 0 Frame 4

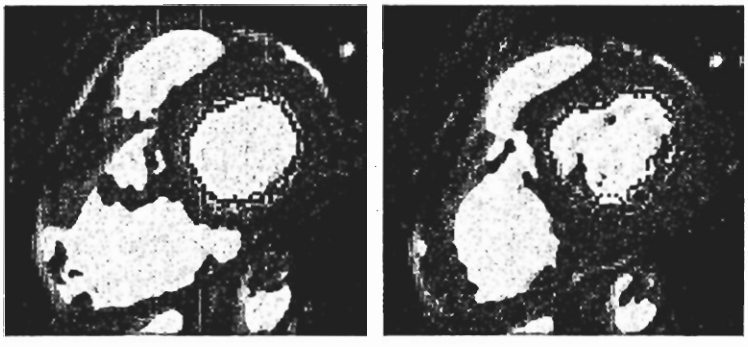

Frame 8 Frame 10

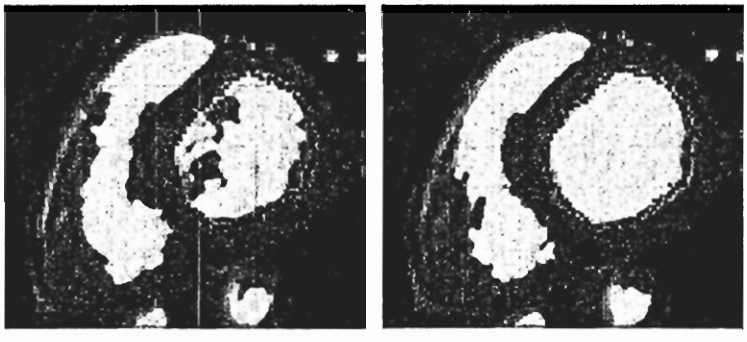

Frame 14 Frame 18

Figure A.6. Individual frame segmentation with the OGF at the basal level of LV. Blue dots indicate the reference boundary by manual segmentation, and red dots indicate the boundary by semiautomatic segmentation.

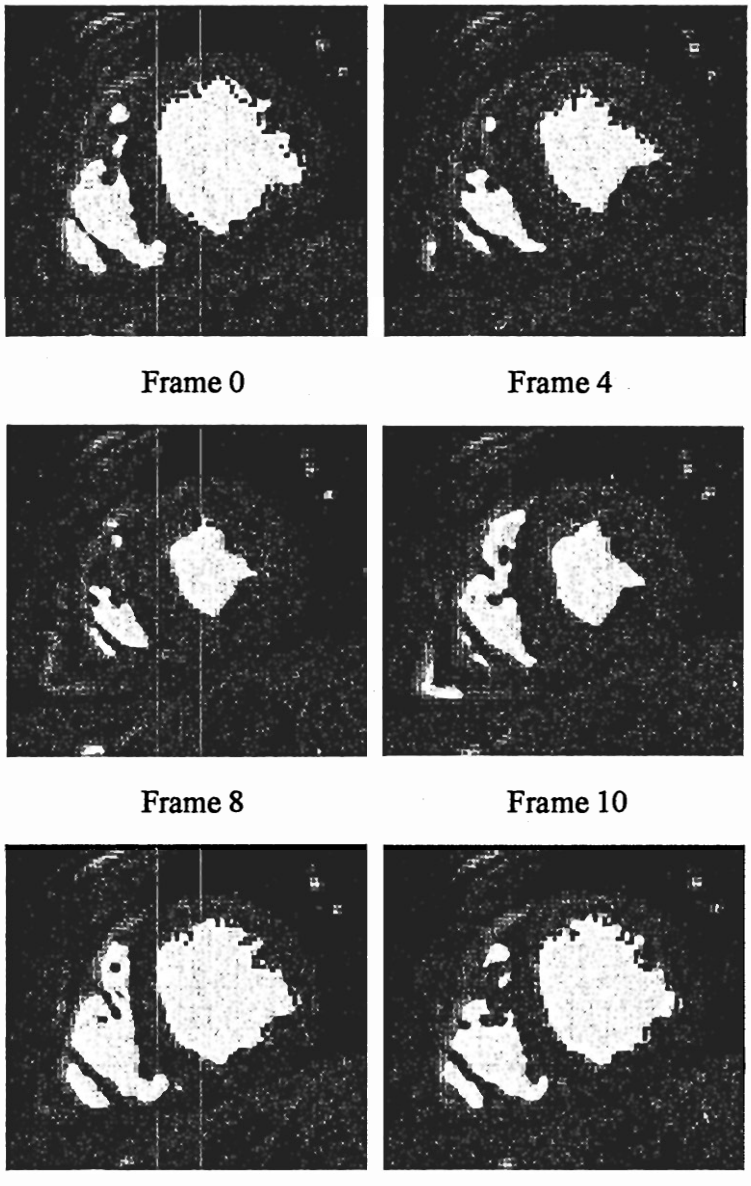

Figure A.7. Sequential frame segmentation without the SCT at the apical level of LV. Red dots indicate the segmented boundary.

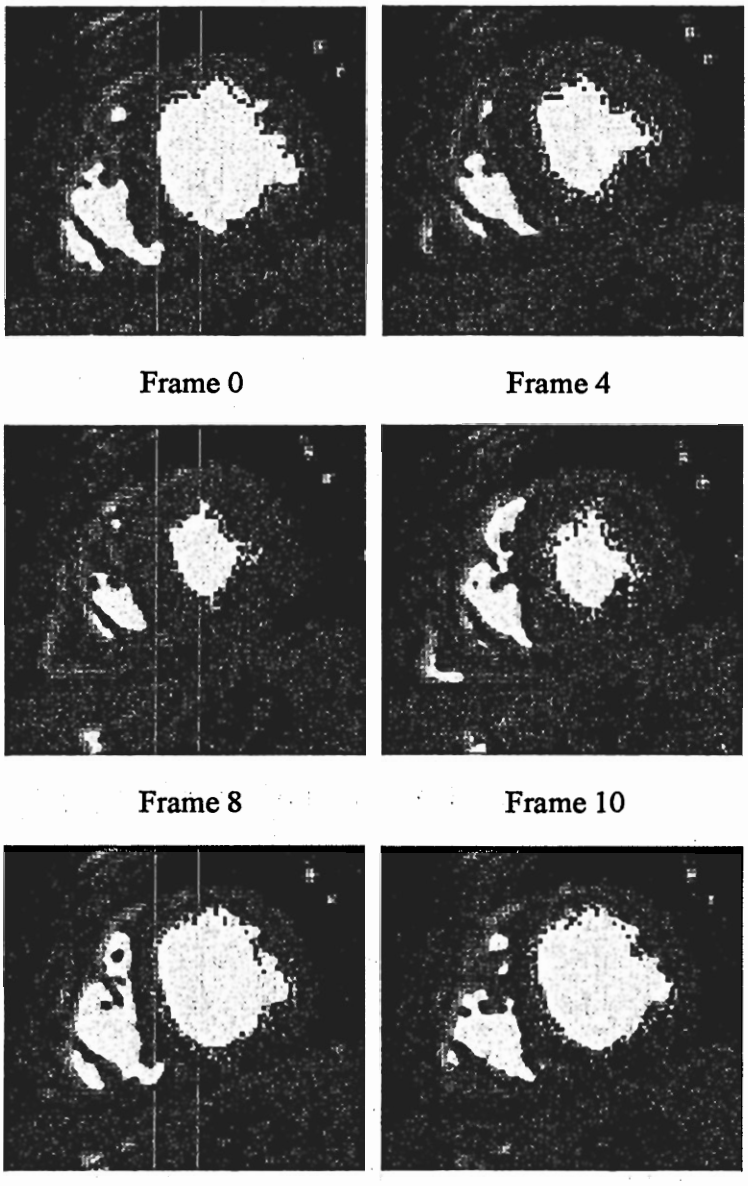

Figure A.8. Sequential frame segmentation with the SCT at the apical level of LV. Red dots indicate the segmented boundary, and green vectors indicate the location of the tracked initial seed contour for the subsequent frame by the SCT.

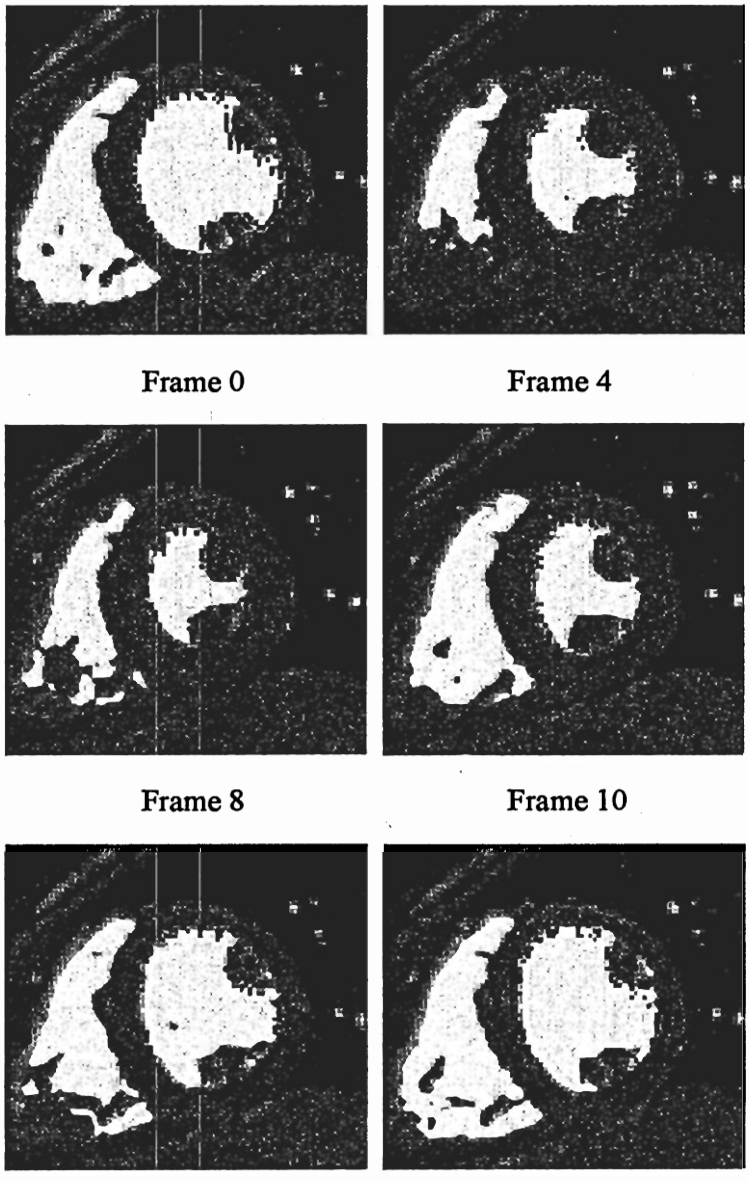

Figure A.9. Sequential frame segmentation without the SCT at the mid-ventricle level of LV. Red dots indicate the segmented boundary.

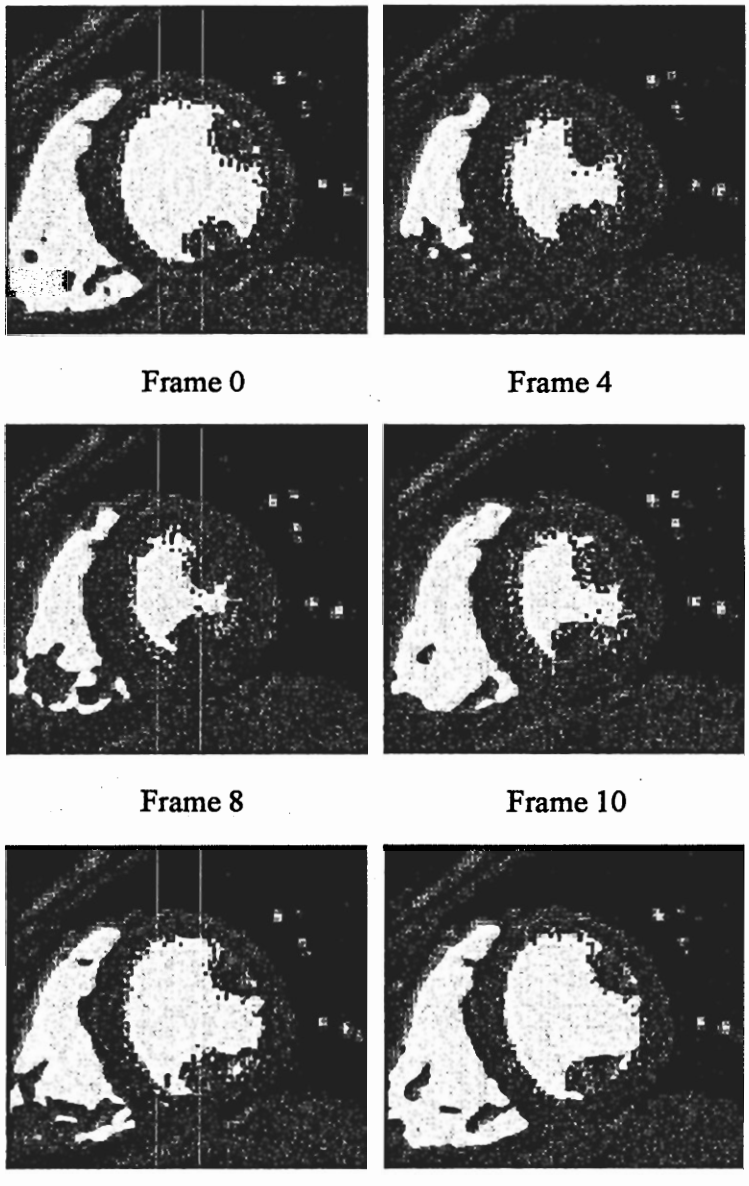

Figure A.10. Sequential frame segmentation with the SCT at the mid-ventricle level of LV. Red dots indicate the segmented boundary, and green vectors indicate the location of the tracked initial seed contour for the subsequent frame by the SCT.

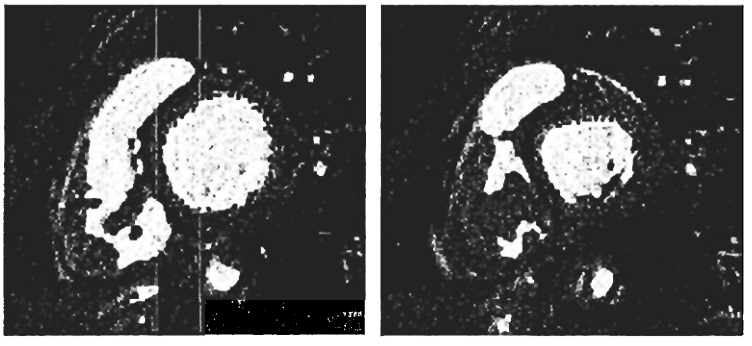

Frame 0 Frame 4

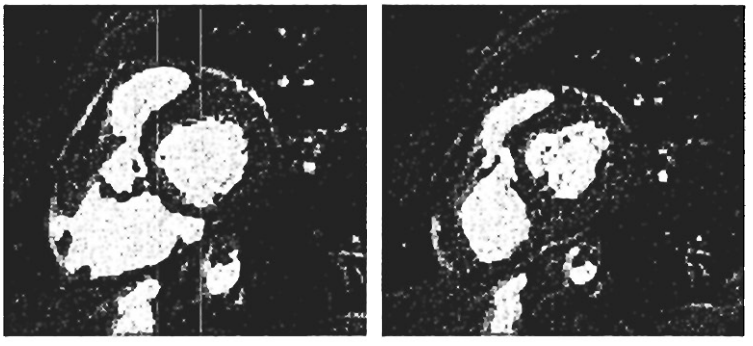

Frame 8 Frame 10

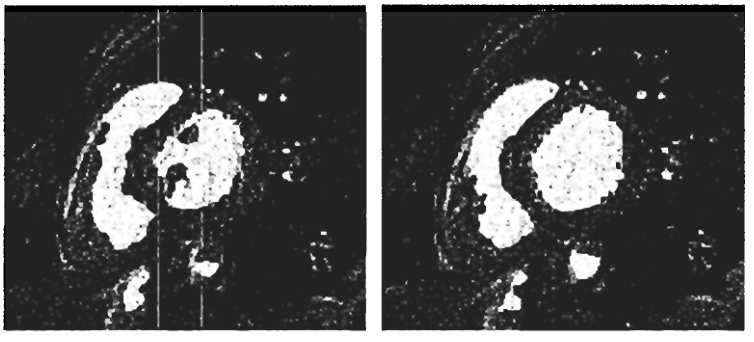

Frame 14 Frame 18

Figure A.11. Sequential frame segmentation without the SCT at the basal level of LV. Red dots indicate the segmented boundary.

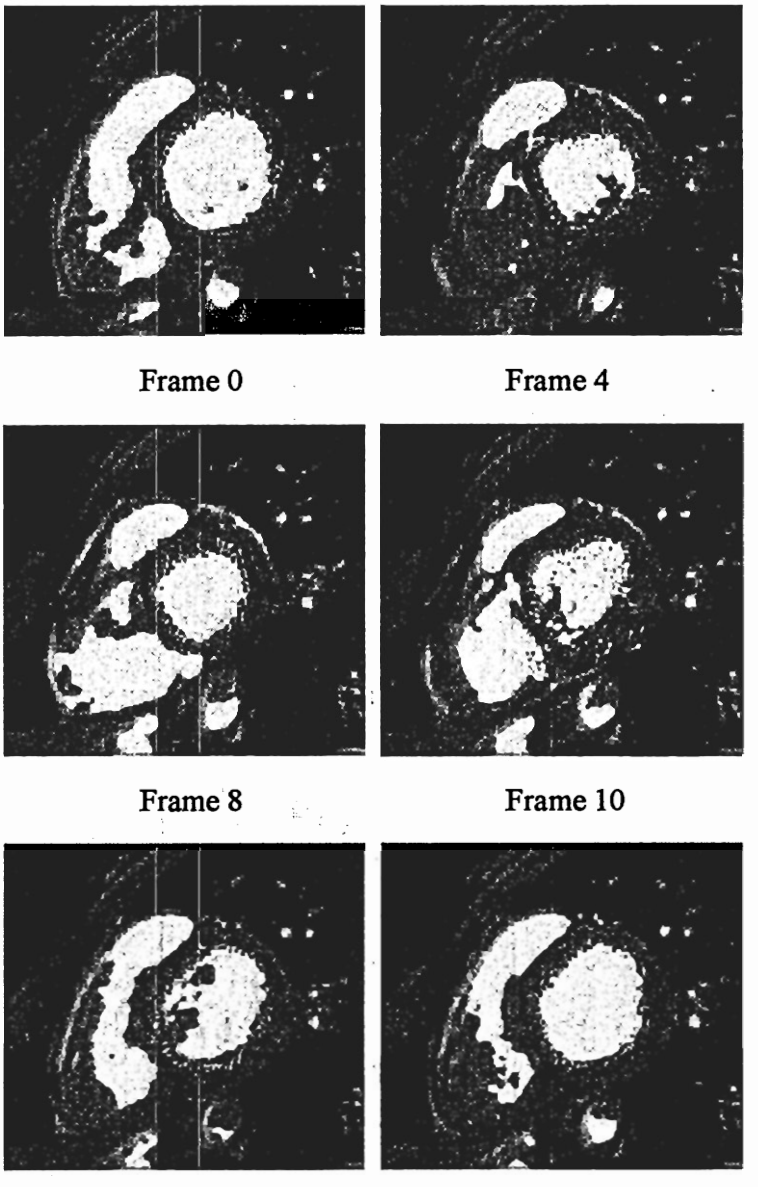

Figure A.12. Sequential frame segmentation with the SCT at the basal level of LV. Red dots indicate the segmented boundary, and green vectors indicate the location of the tracked initial seed contour for the subsequent frame by the SCT.

Appendix B: Derivation of the Simplified Form of the Internal Elastic Force

By letting the integrand $\sum_{i,j=1}^{3} \alpha_{ij}(\mathrm{u})(G_{ij}(\mathbf{p}) - G_{ij}^{0}(\mathbf{p}))^2$ of the deformation potential energy Equation (59) be $\xi(u_1, u_2, u_3, \mathbf{p}, \mathbf{p}_{u1}, \mathbf{p}_{u2}, \mathbf{p}_{u3})$, the deformation potential energy is written as:

$$E_{deformation}(\mathbf{p}) = \int_0^1 \int_0^1 \int_0^1 \xi(u_1, u_2, u_3, \mathbf{p}, \mathbf{p}_{u1}, \mathbf{p}_{u2}, \mathbf{p}_{u3})\, du_1 du_2 du_3 \tag{79}$$

where $\mathbf{p}_{ui} = \frac{\partial \mathbf{p}}{\partial u_i}$. Then, the first variational derivative of the deformation potential energy can be obtained by the Euler-Lagrange differential equation generated upon the integrand ξ, where its solution gives the function that minimizes $E_{deformation}(\mathbf{p})$. By using the Euler-Lagrange differential equation for three independent variables [96]

$$\frac{\partial \xi}{\partial \mathbf{p}} - \frac{\partial}{\partial u_1}\left(\frac{\partial \xi}{\partial \mathbf{p}_{u1}}\right) - \frac{\partial}{\partial u_2}\left(\frac{\partial \xi}{\partial \mathbf{p}_{u2}}\right) - \frac{\partial}{\partial u_3}\left(\frac{\partial \xi}{\partial \mathbf{p}_{u3}}\right) = 0 \tag{80}$$

and the definition of the metric tensor G, a simple vector form of $\delta_{\mathbf{p}} E_{deformation}(\mathbf{p})$ can be approximated. First, by denting the first summation components of the integrand of Equation (79) denoted as ξ_{11},

$$\int_0^1\int_0^1\int_0^1 \xi_{11}(u_1,u_2,u_3,\mathbf{p},\mathbf{p}_{u1},\mathbf{p}_{u2},\mathbf{p}_{u3})du_1du_2du_3 = \int_0^1\int_0^1\int_0^1 \alpha_{11}(\mathrm{u})(G_{11}(\mathbf{p})-G_{11}^0(\mathbf{p}))^2 du_1du_2du_3$$
$$= \int_0^1\int_0^1\int_0^1 \alpha_{11}(\mathrm{u})(\mathbf{p}_{u1}\cdot\mathbf{p}_{u1}-\mathbf{p}_{u1}^0\cdot\mathbf{p}_{u1}^0)^2 du_1du_2du_3 \tag{81}$$

where $\mathbf{p}_{u1}=\dfrac{\partial\mathbf{p}}{\partial u_1}$ and $\mathbf{p}_{u1}^0=\dfrac{\partial\mathbf{p}^0}{\partial u_1}$. Then, components of the Euler-Lagrange differential equation upon the integrand ξ_{11} are calculated as follows:

$$\frac{\partial\xi_{11}}{\partial\mathbf{p}}=0,$$

$$-\frac{\partial}{\partial u_2}\left(\frac{\partial\xi_{11}}{\partial\mathbf{p}_{u2}}\right)=0,$$

$$-\frac{\partial}{\partial u_3}\left(\frac{\partial\xi_{11}}{\partial\mathbf{p}_{u3}}\right)=0, \tag{82}$$

$$-\frac{\partial}{\partial u_1}\left(\frac{\partial\xi_{11}}{\partial\mathbf{p}_{u1}}\right)=-\frac{\partial}{\partial u_1}\left(\frac{\partial\left(\alpha_{11}(\mathrm{u})\left(\mathbf{p}_{u1}\cdot\mathbf{p}_{u1}-\mathbf{p}_{u1}^0\cdot\mathbf{p}_{u1}^0\right)^2\right)}{\partial\mathbf{p}_{u1}}\right)$$
$$=-\frac{\partial}{\partial u_1}\left(4\alpha_{11}(\mathrm{u})\left(G_{11}(\mathbf{p})\cdot\mathbf{p}_{u1}-G_{11}^0(\mathbf{p})\cdot\mathbf{p}_{u1}\right)\right)$$
$$=-\frac{\partial}{\partial u_1}\left(4\alpha_{11}(\mathrm{u})\left(G_{11}(\mathbf{p})-G_{11}^0(\mathbf{p})\right)\frac{\partial\mathbf{p}}{\partial u_1}\right)$$

Then, the first variational derivative of Equation (3) denoted by $\delta_{\mathbf{p}}E_{11}(\mathbf{p})$ becomes

$$\delta_{\mathbf{p}}E_{11}(\mathbf{p})=\frac{\partial\xi_{11}}{\partial\mathbf{p}}-\frac{\partial}{\partial u_1}\left(\frac{\partial\xi_{11}}{\partial\mathbf{p}_{u1}}\right)-\frac{\partial}{\partial u_2}\left(\frac{\partial\xi_{11}}{\partial\mathbf{p}_{u2}}\right)-\frac{\partial}{\partial u_3}\left(\frac{\partial\xi_{11}}{\partial\mathbf{p}_{u3}}\right)$$
$$=-\frac{\partial}{\partial u_1}\left(4\alpha_{11}(\mathrm{u})\left(G_{11}(\mathbf{p})-G_{11}^0(\mathbf{p})\right)\frac{\partial\mathbf{p}}{\partial u_1}\right) \tag{83}$$

By similar fashion, all other derivatives are calculated as follows:

$$\delta_{\mathrm{p}} E_{22}(\mathbf{p}) = -\frac{\partial}{\partial u_2}\left(4\alpha_{22}(\mathrm{u})\left(G_{22}(\mathbf{p}) - G_{22}^{0}(\mathbf{p})\right)\frac{\partial \mathbf{p}}{\partial u_2}\right) \tag{84}$$

$$\delta_{\mathrm{p}} E_{33}(\mathbf{p}) = -\frac{\partial}{\partial u_3}\left(4\alpha_{33}(\mathrm{u})\left(G_{33}(\mathbf{p}) - G_{33}^{0}(\mathbf{p})\right)\frac{\partial \mathbf{p}}{\partial u_3}\right) \tag{85}$$

$$\begin{aligned}\delta_{\mathrm{p}} E_{12}(\mathbf{p}) = &-\frac{\partial}{\partial u_1}\left(2\alpha_{12}(\mathrm{u})\left(G_{12}(\mathbf{p}) - G_{12}^{0}(\mathbf{p})\right)\frac{\partial \mathbf{p}}{\partial u_2}\right) \\ &-\frac{\partial}{\partial u_2}\left(2\alpha_{12}(\mathrm{u})\left(G_{12}(\mathbf{p}) - G_{12}^{0}(\mathbf{p})\right)\frac{\partial \mathbf{p}}{\partial u_1}\right)\end{aligned} \tag{86}$$

$$\begin{aligned}\delta_{\mathrm{p}} E_{21}(\mathbf{p}) = &-\frac{\partial}{\partial u_1}\left(2\alpha_{21}(\mathrm{u})\left(G_{21}(\mathbf{p}) - G_{21}^{0}(\mathbf{p})\right)\frac{\partial \mathbf{p}}{\partial u_2}\right) \\ &-\frac{\partial}{\partial u_2}\left(2\alpha_{21}(\mathrm{u})\left(G_{21}(\mathbf{p}) - G_{21}^{0}(\mathbf{p})\right)\frac{\partial \mathbf{p}}{\partial u_1}\right)\end{aligned} \tag{87}$$

$$\begin{aligned}\delta_{\mathrm{p}} E_{13}(\mathbf{p}) = &-\frac{\partial}{\partial u_1}\left(2\alpha_{13}(\mathrm{u})\left(G_{13}(\mathbf{p}) - G_{13}^{0}(\mathbf{p})\right)\frac{\partial \mathbf{p}}{\partial u_3}\right) \\ &-\frac{\partial}{\partial u_3}\left(2\alpha_{13}(\mathrm{u})\left(G_{13}(\mathbf{p}) - G_{13}^{0}(\mathbf{p})\right)\frac{\partial \mathbf{p}}{\partial u_1}\right)\end{aligned} \tag{88}$$

$$\begin{aligned}\delta_{\mathrm{p}} E_{31}(\mathbf{p}) = &-\frac{\partial}{\partial u_1}\left(2\alpha_{31}(\mathrm{u})\left(G_{31}(\mathbf{p}) - G_{31}^{0}(\mathbf{p})\right)\frac{\partial \mathbf{p}}{\partial u_3}\right) \\ &-\frac{\partial}{\partial u_3}\left(2\alpha_{31}(\mathrm{u})\left(G_{31}(\mathbf{p}) - G_{31}^{0}(\mathbf{p})\right)\frac{\partial \mathbf{p}}{\partial u_1}\right)\end{aligned} \tag{89}$$

$$\begin{aligned}\delta_{\mathrm{p}} E_{23}(\mathbf{p}) = &-\frac{\partial}{\partial u_2}\left(2\alpha_{23}(\mathrm{u})\left(G_{23}(\mathbf{p}) - G_{23}^{0}(\mathbf{p})\right)\frac{\partial \mathbf{p}}{\partial u_3}\right) \\ &-\frac{\partial}{\partial u_3}\left(2\alpha_{23}(\mathrm{u})\left(G_{23}(\mathbf{p}) - G_{23}^{0}(\mathbf{p})\right)\frac{\partial \mathbf{p}}{\partial u_2}\right)\end{aligned} \tag{90}$$

$$\delta_{\mathbf{p}} E_{32}(\mathbf{p}) = -\frac{\partial}{\partial u_2}\left(2\alpha_{32}(\mathrm{u})\left(G_{32}(\mathbf{p}) - G_{32}^{0}(\mathbf{p})\right)\frac{\partial \mathbf{p}}{\partial u_3}\right) - \frac{\partial}{\partial u_3}\left(2\alpha_{32}(\mathrm{u})\left(G_{32}(\mathbf{p}) - G_{32}^{0}(\mathbf{p})\right)\frac{\partial \mathbf{p}}{\partial u_2}\right) \tag{91}$$

Then, with the assumption of the isotropic material ($\alpha_{ij}(\mathrm{u}) = \alpha_{ji}(\mathrm{u})$, if $i \neq j$), the approximated first variational derivative of Equation (79) is obtained by adding Equation (83), (84), (85), (86), (87), (88), (89), (90), and (91) and dropping out all the constant coefficients:

$$\delta_{\mathbf{p}} E_{deformation}(\mathbf{p}) = \sum_{i,j=1}^{3} -\frac{\partial}{\partial u_i}\left(\alpha_{ij}(\mathrm{u})\left(G_{ij}(\mathbf{p}) - G_{ij}^{0}(\mathbf{p})\right)\frac{\partial \mathbf{p}}{\partial u_j}\right) \tag{92}$$

This completes the derivation of the simplified internal elastic deformation force.

REFERENCES

[1] A. Bazille, M.A. Guttman, E.R. Mcveigh, and E.A. Zerhouni, "Impact of semiautomated versus manual image segmentation errors on myocardial strain calculation by magnetic resonance tagging," *Investigative Radiology*, vol. 29, no. 4, pp. 427-433, 1994.

[2] N.B. Ingels, G.T. Daughters, E.B. Stinson, and E.L. Alderman, "Evaluation of methods for quantitating left ventricular segmental wall motion in man using myocardial markers as a standard," *Circulation*, vol. 61, pp. 966-973, 1980.

[3] G.D. Meier, M.C. Ziskin, W.P. Santamore, and A.A. Bove, "Kinematics of the beating heart," *IEEE Trans. Biomed. Engr.*, vol. BME-27, no. 6, 1980.

[4] E.A. Zerhouni, D.M. Parish, W.J. Rogers, A. Yang, and E.P. Shapiro, "Human heart: tagging with MR imaging – a method for noninvasive assessment of myocardial motion," *Radiology*, vol. 169, pp. 59-64, 1988.

[5] L. Axel and L. Dougherty, "MR imaging of motion with spatial modulation of magnetization," *Radiology*, vol. 171, pp.841-845, 1989.

[6] L. Axel and L. Dougherty, "Heart wall motion: improved method of spatial modulation of magnetization for MR imaging," *Radiology*, vol. 172, pp. 349-350, 1989.

[7] B.D. Bolster, E.R. McVeigh, and E.A. Zerhouni, "Myocardial tagging in polar coordinates with use of striped tags," *Radiology*, vol. 177, pp. 769-772, 1990.

[8] N.J. Pelc, R.J. Herfkens, A. Shimakawa, and D.R. Enzmann, "Phase contrast cine magnetic resonance imaging," *Magnetic Resonance Quarterly*, vol. 7, no. 4, pp. 229-254, 1991.

[9] M. Kass, A. Witkin, and D. Terzopoulos, "Snakes: active contour models," *Int J. Computer Vision*, pp. 321-331, 1987.

[10] C. Vuille and A.E. Weyman, "Left ventricle 1: General considerations, assessment of chamber size and function," in *Principles and Practice of Echocardigraphy*, 2nd ed. A.E. Weyman, Ed. Philadelphia PA: Lea and Febiger, 1994.

[11] C.H. Lorenz, E.S. Walker, V.L. Morgan, S.S. Klein, and T.P. Graham, Jr., "Normal human right and left ventricular mass, systolic function and gender differences by cine magnetic resonance imaging," *J. Cardiovasc. Magn. Res.*, vol. 1, no. 1, pp. 7-21, 1999.

[12] H. Azhari, S. Sideman, J.L. Weiss, E.P. Shapiro, M.L. Weisfeldt, W.L. Graves, W.J. Rogers, and R. Beyar, "Three-dimensional mapping of acute ischemic regions using MRI: wall thickening versus motion analysis," *The American Journal of Physiology*, Pt. 2, vol. 259, no. 5, pp. H1492-1503, Nov. 1990.

[13] A.A. Young and L. Axel, "Three-dimensional motion and deformation of the heart wall: estimation with spatial modulation of magnetization – a model-based approach," *Radiology*, vol. 185, pp. 241-247, 1992.

[14] A.A. Young, C.M. Kramer, V.A. Ferrai, L. Axel, and N. Reichek, "Three-dimensional left ventricular deformation in hypertropic cardiomyopathy," *Circulation*, vol. 90, pp. 854-867, 1994.

[15] J. Park and S. Park, "Strain analysis and visualization: left ventricle of a heart," *Computers & Graphics*, vol. 24, pp. 701-714, 2000.

[16] M.D. Robson and R.T. Constable, "Three-dimensional strain-rate imaging," *Magn Reson Med*, vol. 36, no. 4, pp. 537-546, Oct. 1996.

[17] A. Heimdal, A. Stoylen, H.T. DrTechn, and T. Skjaerpe, "Real-time strain rate imaging of the left ventricle by ultrasound," *J Am Soc Echo*, vol. 11, no. 11, pp. 1013-1019, Nov. 1998.

[18] J.U. Voigt, M. Arnold, T. Kukulski, M. Karlsson, and G.R. Sutherland, "Is strain rate imaging applicable to the clinical setting? Preliminary in vivo data," *J Am Coll Cardiol*, vol. 33 (Suppl A), pp. 429A, 1999.

[19] B.H. Smaill and P.J. Hunter, "Structure and function of the diastolic heart: material properties of the passive myocardium," In *Theory of the heart*, Berlin, Springer-Verlag, 1991.

[20] L.D. Cohen, "On active contour models and balloons," *CVGIP: Image Understanding*, vol. 53, no. 2, pp. 211-218, Mar. 1991.

[21] L.D. Cohen and I. Cohen, "Finite element methods for active contour models and balloons for {2-D} and {3-D} images," *IEEE Transactions on Pattern Analysis and Machine Intelligence*, vol. 15, no. 11, pp. 1131-1147, 1993.

[22] J.L. Prince and C. Xu, "A new external force model for snakes," In *1996 Image and Multimedimensional Signal Processing Workshop*, pp. 30-31, 1996.

[23] C. Xu and J.L. Prince, "Gradient vector flow: a new external force for snakes," *IEEE Proc. Conf. on Comp. Vis. Patt. Recog. (CVPR'97)*, Los Alamitos: Comp. Soc. Press, pp. 66-71, 1997.

[24] S. Kozerke, R. Botnar, S. Oyre, M.B. Scheidegger, E.M. Pedersen, and P. Boesiger, "Automatic vessel segmentation using active contours in cine phase contrast flow measurements," *Journal of Magnetic Resonance Imaging*, vol. 10, pp. 41-51, 1999.

[25] F. Leymarie and M.D. Levine, "Tracking Deformable Objects in the Plane Using an Active Contour Model," *IEEE-PAMI*, vol. 15(6), pp. 617-634, June 1993.

[26] A. Gupta, L.V. Kurowski, A. Singh, D Geiger, C-C Liang, M-Y Chiu, L.P. Adler, M. Haacke, and D.L. Wilson, "Cardiac MR image segmentation using deformable models," *Proc. IEEE Conf. Computers in Cardiology*, pp. 747-750, 1993.

[27] V. Chalana, D.T. Linker, D.R. Haynor, and Y. Kim, "A multiple active contour model for cardiac boundary detection on echocardiographic sequences," *IEEE Trans. Med. Imag.*, vol. 15, no. 3, pp. 290-298, June 1996.

[28] M. Li and C. Kambhamettu, "Motion-based post processing of deformable contours," *ICVGIP*, Dec. 2002.

[29] Y.S. Akgul, C. Kambhamettu, and M. Stone, "Extraction and tracking of the tongue surface from ultrasound image sequences," In *Proc. IEEE Computer Vision Pattern Recognition*, Santa Barbara, CA, pp. 298-303, June 1998.

[30] Y.S. Akgul, C. Kambhamettu, and M. Stone, "Automatic motion analysis of the tongue surface from ultrasound image sequences," In *Proc. IEEE Workshop Biomedical Image Analysis*, Santa Barbara, CA, pp. 126-132, June 1998.

[31] Y.S. Akgul, C. Kambhamettu, and M. Stone, "Automatic extraction and tracking fo the tongue contours," *IEEE Trans. On Med. Imag.*, vol. 18, no 10, October 1999.

[32] N. Peterfreund, "The velocity snake: Deformable contour for tracking in spatio-velocity space," *Computer Vision and Image Understanding*, vol. 73, no. 3, pp. 346-356, Mar. 1999.

[33] G.H. Glover, N.J. Pelc, "A rapid-gated cine MRI technique", In *Kressel HY, ed. Magnetic resonance annual*, New York: Raven, pp. 299-333, 1988.

[34] K.F. Lai, "Deformable contours: modeling, extraction, detection, and classification," *Ph.D. Dissertation*, Department of Electrical Engineering, University of Wisconsin at Madison, WI, 1994.

[35] GH. Granlund and H. Knutsson, "Signal processing for computer vision," *Kluwer Academic Publishers*, 1995.

[36] H. knutsson, "Filtering and reconstruction in image processing," *Ph.D. Dissertation*, Linköping University, 1982.

[37] A.A. Amini, T.E. Weymouth, and R.C. Jain, "Using dynamic programming for solving variational problems in vision," *IEEE Trans. Pat. Anal. Mach. Intell.*, vol. PAMI-12, no. 9, pp. 855-867, 1990.

[38] R.T. Constable, K.M. Rath, A.J. Sinusas, and J.C. Gore, "Development and evaluation of tracking algorithms for cardiac wall motion analysis using phase velocity MR imaging," *Magnetic Resonance in Medicine*, vol. 32, pp. 33-42, 1994.

[39] E.L. Dove, K.P. Philip, D.D. McPherson, and K.B. Chandran, "Quantitative shape descriptors of left-ventricular cine-CT images," *IEEE Trans. Biomed. Eng.*, vol. 38, no. 12, pp. 1256-1261, Dec. 1991.

[40] K.P. Philip, E.L. Dove, D.D. McPherson, N.L. Gotteiner, M.J. Vonesh, W. Stanford, J.E. Reed, J.A. Rumberger, and K.B. Chandran, "Automatic detection of myocardial contours in cine-Computed Tomographic images," *IEEE Trans. Med. Imag.*, vol. 13, no. 2, pp. 241-253, June 1994.

[41] R. C. Gonzalez and E. Wintz, "Digital Image Processing," *Addison-Wesley*, 1987.

[42] J.R. Singer and L.E. Crooks, "Nuclear magnetic resonance blood flow measurements in the human brain," *Science*, vol. 221, pp. 654-656, 1983.

[43] L. Axel, R. Goncalves, and D. Bloomgarden, "Regional heart wall motion: two-dimensional analysis and functional imaging of regional heart wall motion with magnetic resonance imaging," *Radiology*, vol. 183, pp. 745-750, 1992.

[44] A.A. Young, L. Axel, L. Dougherty, D.K. Bogen, and C.S. Parenteau, "Validation of tagging with MR imaging to estimate material deformation," *Radiology*, vol. 188, pp. 101-108, 1993.

[45] A.A. Young, H. Imai, C.N. Chang, and L. Axel, "Two-dimensional left ventricular deformation during systole using magnetic resonance imaging with spatial modulation of magnetization," *Circulation*, vol. 89, pp. 740-752, 1994.

[46] S.E. Maier and S.E. Fischer, "Evaluation of left ventricular segmental wall motion in hypertrophic cardiomyopathy with myocardial tagging," *Circulation*, vol. 86, no. 6, pp. 1919-1928, 1992.

[47] S.E. Maier and S.E. Fischer, "Acquisition and evaluation of tagged magnetic resonance images of the human left ventricle," *Computerized Medical Imaging and Graphics*, vol. 16, no. 2, pp. 73-80, 1992.

[48] J.A.C. Lima, V.A. Ferrari, N. Reichek, C.M. Kramer, L. Palmon, M.R. Llaneras, B. Tallant, A.A. Young, and L. Axel, "Segmental motion and deformation of transmurally infarcted myocardium in acute postinfarct period," *The American Journal of Physiology*, vol. 268, pp. H1304-H1312, 1995.

[49] M.A. Fogel, K.B. Gupta, P.M. Weinberg, and E.A. Hoffman, "Regional wall motion and strain analysis across stages of fontan reconstruction by magnetic resonance tagging," *The American Journal of Physiology*, vol. 269, pp. H1132-H1152, 1995.

[50] A.A. Young, D.L. Kraitchman, and L. Axel, "Deformable models for tagged MR images: reconstruction of two- and three-dimensional heart wall motion," *Proc. IEEE Workshop on Biomedical Image Analysis*, pp. 317-323, 1994.

[51] A.A. Young, D.L. Kraitchman, L. Dougherty, and L. Axel, "Tracking and finite element analysis of stripe deformation in magnetic resonance tagging," *IEEE Transactions on Medical Imaging*, vol. 14, no. 3, pp. 413-421, 1995.

[52] A.A. Young and L. Axel, "Non-rigid heart wall motion using MR tagging," *Proc. Computer Vision and Pattern Recognition*, pp.399-404, 1992.

[53] A.A. Young, R. Orr, B.H. Smaill, and L.J. Dell'Italia, "Three-dimensional changes in left and right ventricular geometry in chronic mitral regurgitation," *The American Journal of Physiology*, vol. 271, pp. H2689-H2700, 1996.

[54] P.M.F. Nielsen, I.J. LE Grice, B.H. Smaill, and P.J. Hunter, "Mathematical model of geometry and fibrous structure of the heart," *The American Journal of Physiology*, vol. 260, pp. H1365-H1378, 1991.

[55] A.A. Young, Z.A. Fayad, and L. Axel, "Right ventricular midwall surface motion and deformation using magnetic resonance tagging," *The American Journal of Physiology*, vol. 271, pp. H2677-H2688, 1996.

[56] A.A. Young, "Model tags: direct 3D tracking of heart wall motion from tagged MR images," *Medical Image Analysis*, pp. 92-101, 1999.

[57] J. Park, D. Metaxas, and A.A. Young, "Deformable models with parameter functions: Application to heart wall modeling," *Proc. Computer Vision and Pattern Recognition*, pp. 437-422, 1994.

[58] J. Park, D. Metaxas, A.A. Young, and L. Axel, "Deformable models with parameter functions for cardiac motion analysis from tagged MRI data," *IEEE Transactions on Medical Imaging*, vol. 15, pp.278-289, 1996.

[59] J. Park, D. Metaxas, and L. Axel, "Analysis of left ventricular wall motion based on volumetric deformable models and MRI-SPAMM," *Medical Image Analysis*, vol. 1, no. 1, pp. 53-71, 1996.

[60] J. Park, "Model based shape and motion analysis: left ventricle of a heart", *Ph.D. Dissertation*, Department of Computer and Information Science, University of Pennsylvania, 1996.

[61] W.G. O'Dell, C.C. Moore, W.C. Hunter, E.A. Zerhouni, and E.R. McVeigh, "Three-dimensional myocardial deformations: calculation with displacement field fitting to tagged MRI images," *Radiology*, vol. 195, no. 3, pp. 829-835, 1995.

[62] W.G O'Dell, C.C. Moore, and E.R. McVeigh,"Displacement field fitting approach to calculate 3D deformations from parallel tagged grids," *J. Mag. Res. Imag.*, vol. 3, pp. 208, 1993.

[63] W.S. Kerwin and J.L. Prince, "Cardiac material markers from tagged MR images," *Medical Image Analysis*, vol. 2, no. 4, pp. 339-353, 1998.

[64] C. Ozturk and E.R. McVeigh, "Four dimensional B-spline based motion analysis of tagged cardiac MR images," *Proc. SPIE Medical Imaging 99*, San Diego, Feb. 1999.

[65] T.S. Denney and J.L. Prince, "Reconstruction of 3-D left ventricular motion from planar tagged cardiac MR images: an estimation theoretic approach," *IEEE Transactions on Medical Imaging*, vol. 14, no. 4, pp. 625-635, 1995.

[66] D.L. Kraitchman, A.A. Young, C.N. Chang, and L. Axel, "Semi-automatic tracking of myocardial motion in MR tagged images," *IEEE Transactions on Medical Imaging*, vol. 14, no. 3, pp. 422-433, 1995.

[67] S. Kumar and D. Goldgof, "Automatic tracking of SPAMM grid and the estimation of deformation parameters from cardiac MR images," *IEEE Transactions on Medical Imaging*, vol. 13, no. 1, pp. 122-132, 1994.

[68] M. A. Guttman, J.L. Prince, and E.R. McVeigh, "Tag and contour detection in tagged MR images of the left ventricle," *IEEE Transactions on Medical Imaging*, vol. 13, no. 1, pp. 74-88, 1994.

[69] P.V. Dijk, "Direct cardiac NMR imaging of heart wall and blood flow velocity," *Journal of Computer Assisted Tomography*, vol. 8, pp. 429-436, 1984.

[70] G.L. Nayler, D.N. Firmin, and D.B. Longmore, "Blood flow imaging by cine magnetic resonance," *Journal of Computer Assisted Tomography*, vol. 10, pp. 715-722, 1986.

[71] N.J. Pelc, "Myocardial motion analysis with phase contrast cine MRI," *Proc. SMRM*, 10th Annual Meeting, p. 17, 1991.

[72] N.J. Pelc, R.J. Herfkens, and L.R. Pelc, "3D analysis of myocardial motion and deformation with phase contrast cine MRI," *Proc. SMRM*, 11th Annual Meeting, p. 18, 1992.

[73] R.T. Constable, K.M. Rath, A.J. Sinusas, and J.C. Gore, "Development and evaluation of tracking algorithms for cardiac wall motion analysis using phase velocity MR imaging," *Magnetic Resonance in Medicine*, vol. 32, pp. 33-42, 1994.

[74] N.J. Pelc, M. Drangova, L.R. Pelc, Y. Zhu, D.C. Noll, B.S. Bowman, and R.J. Herkens "Tracking of cyclic motion with phase contrast cine MR velocity data," *Journal of Magnetic Resonance*, vol. 5, no. 3, pp. 339-345, 1995.

[75] L.R. Pelc, J. Sayre, K. Yun, L.J. Castro, R.J. Herfkens, D.C. Miller, and N.J. Pelc, "Evaluation of myocardial motion tracking with cine-phase contrast magnetic resonance imaging," *Investigative Radiology*, vol. 29, pp. 1038-1042, 1994.

[76] A. Lingamneni, P.A. Hardy, K.A. Powell, N.J. Pelc, and R.D. White, "Validation of cine phase-contrast MR imaging for motion analysis," *Journal of Magnetic Resonance*, vol. 5, No. 3, pp. 331-338, 1995.

[77] Y. Zhu, M. Drangova, and N.J. Pelc, "Fourier tracking of myocardial motion using cine-pc data," *Magnetic Resonance in Medicine*, vol. 35, pp. 471-480, 1996.

[78] M. Drangova, Y. Zhu, B. Bowman, and N.J. Pelc, "In vitro verification of myocardial motion tracking from phase-contrast velocity data," *Magnetic Resonance Imaging*, vol. 16, no. 8, pp. 863-870, 1998.

[79] Y. Zhu and N.J. Pelc, "Three-dimensional motion tracking with volumetric phase contrast MR velocity imaging," *Journal of Magnetic Resonance Imaging*, vol. 9, pp. 111-118, 1999.

[80] Y. Zhu and N.J. Pelc, "A spatiotemporal model of cyclic kinematics and its application to analyzing nonrigid motion with MR velocity images," *IEEE Transactions on Medical Imaging*, vol. 18, no. 7, pp. 557-569, 1999.

[81] S.M. Song and R.M. Leahy, "Computation of 3-D velocity fields from 3-D cine CT images of a human heart," *IEEE Transactions on Medical Imaging*, vol. 10, no. 3, pp. 295-306, 1991.

[82] A.A. Amini and J.S. Duncan, "Bending and stretching models for LV wall motion analysis from curves and surfaces," *Image and Vision Computing*, vol. 10, no. 6, pp. 418-430, 1992.

[83] P. Shi, "Image analysis of 3D Cardiac Motion using physical and geometrical models," *Ph.D. Dissertation*, Yale University, CT, 1996.

[84] P. Shi, A.J. Sinusas, R.T. Constable, E. Ritman, and J.S. Duncan, "Point-tracked quantitative analysis of left ventricular motion from 3D image sequences," *IEEE Transactions on Medical Imaging*, vol. 19, no. 1, pp. 36-50, 2000.

[85] P. Shi, A.J. Sinusas, R.T. Constable, and J.S. Duncan, "Volumetric deformation analysis using mechanics-based data fusion: Applications in cardiac motion recovery," *International Journal of computer Vision*, vol. 35, no. 1, pp. 65-85, 1999.

[86] S. Papademetris, A.J. Sunusas, D.P. Dione, and J.S. Duncan, "3D cardiac deformation from ultrasound images," *Medical Image Computing and Computer Aided Intervention*, vol. 1679, pp. 420-429, 1999.

[87] D. Terzopoulos and K. Fleischer, "Deformable Models," *The Visual Computer*, vol. 4, pp. 306-331, 1988.

[88] J.D. Faux, M.J. Pratt, "Computational geometry for design and manufacture," *Halstead Press*, Horwood, NY, 1981.

[89] P.G Ciarlet, "Mathematical elasticity, vol. I: Three-dimensional elasticity," *North-Holland*, 1988.

[90] L. Lapidus, G F. Pinder, "Numerical solution of partial differential equations in science and engineering," *Wiley Inter-Science*, 1999.

[91] K. Huebner, "The finite element method for engineers," *John Wiley and Sons*, New York, 1975.

[92] S. Gibson and B. Mirtich, "A survey of deformable modeling in computer graphics," *Mitsubishi Electroincs Research Laboratory Technical Report* TR-97-19, November 1997.

[93] G T. Herman, J. Zheng, C. A. Bucholtz, "Shape-based interpolation," *IEEE Computer Graphics and Applications*, pp. 69-79, 1992.

[94] J. D'hooge, A. Heimdal, F. Jamal, T. Kukulski, B. Bijnens, F. Rademakers, L. Hatle, P. Suetens, and G R. Sutherland, "Regional strain and strain measurements by cardiac ultrasound: principles, implementation and limitations," *European Journal Echocardiography*, vol. 1, no. 3, pp. 154-170, 2000.

[95] J. Marcus, M. Gotte, A. Rossum, J. Jujier, R. Heethaar, L. Axel, C. Visser, "Myocardial function in infarcted and remote regions early after infarction in man: assessment by magnetic resonance tagging and strain analysis," *Magnetic Resonance in Medicine*, vol. 38, p. 803-810, 1997.

[96] R. Weinstock, "Calculus of variations, with applications to physics and engineering," *Dover Publications*, New York, 1974.